

2010

Configurational effect on dust cloud formation and brownout

Sayan Ghosh
Iowa State University

Follow this and additional works at: <https://lib.dr.iastate.edu/etd>

 Part of the [Aerospace Engineering Commons](#)

Recommended Citation

Ghosh, Sayan, "Configurational effect on dust cloud formation and brownout" (2010). *Graduate Theses and Dissertations*. 11489.
<https://lib.dr.iastate.edu/etd/11489>

This Thesis is brought to you for free and open access by the Iowa State University Capstones, Theses and Dissertations at Iowa State University Digital Repository. It has been accepted for inclusion in Graduate Theses and Dissertations by an authorized administrator of Iowa State University Digital Repository. For more information, please contact digirep@iastate.edu.

Configurational effect on dust cloud formation and brownout

by

Sayan Ghosh

A thesis submitted to the graduate faculty
in partial fulfillment of the requirements for the degree of
MASTER OF SCIENCE

Major: Aerospace Engineering

Program of Study Committee:
R. Ganesh Rajagopalan, Major Professor
Thomas J. Rudolphi
Bong Wie

Iowa State University

Ames, Iowa

2010

Copyright © Sayan Ghosh, 2010. All rights reserved.

TABLE OF CONTENTS

LIST OF TABLES	iii
LIST OF FIGURES	iv
NOMENCLATURE	v
ACKNOWLEDGEMENTS	vii
CHAPTER 1. OVERVIEW	1
1.1 Current Research	3
1.1.1 Turbulence models	4
1.1.2 Rotor model	5
1.1.3 Dust transport model	6
CHAPTER 2. TURBULENT ROTOR FLOW MODELING	7
2.1 Reynolds Average Navier-Stokes (RANS) Equation	7
2.2 Eddy Viscosity-based Turbulence Model	9
2.2.1 Baldwin-Lomax Model	10
2.2.2 Spalart-Allmaras Model	12
2.2.3 $k - \epsilon$ Models	13
2.2.3.1 Standard $k - \epsilon$ model	14
2.2.3.2 Realizable $k - \epsilon$ model	16
2.3 Rotor Source Modeling	18
2.3.1 Rotor source calculation	18
CHAPTER 3. DUST TRANSPORT MODELING	22
3.1 Particle Characteristics	23

3.1.1	Equivalent particle diameter	23
3.1.2	Forces on particle	25
3.1.3	Particle terminal velocity	29
3.1.4	Particle threshold friction velocity	31
3.2	Modes of Particle Transport	33
3.2.1	Dust emission mechanism and modeling	34
3.2.2	Vertical particle flux	35
3.3	Dust Transport Modeling	37
3.3.1	Particle Stokes number	38
3.3.2	Particle volume fraction	39
3.3.3	Particle bulk density (Dust cloud density)	39
3.3.4	Particle loading	39
3.3.5	Dilute versus dense flows and phase coupling	39
3.3.6	Rotorcraft Brownout Model	41
3.3.6.1	Dust Transport Equation	43
3.3.6.2	Dust Particle Velocity	45
CHAPTER 4. NUMERICAL METHOD AND ALGORITHM		46
4.1	General Convection-Diffusion Equation	46
4.1.1	Scalar variables	50
4.2	Momentum Equations	53
4.2.1	Pressure correction equation	55
4.2.2	The pressure equation	57
4.2.3	The SIMPLER algorithm	59
4.3	Boundary conditions	59
4.3.1	Inlet boundary conditions	60
4.3.2	Outlet boundary conditions	60
4.3.3	Wall boundary condition	61
4.3.4	Computational process	61

CHAPTER 5. RESULTS	63
5.1 Validation	63
5.1.1 3D incompressible solver	63
5.1.2 Turbulence models	64
5.1.3 Rotor model validation	70
5.1.4 Brownout model validation	71
5.2 Turbulence Model Comparison for Rotor in Ground Effect	73
5.3 Fuselage Effect on Wake and Ground Signature	75
5.4 Fuselage Effect on Brownout	89
5.5 Fuselage Shape Effect on Wake and Ground Signature	95
5.6 Multi-Rotor Configuration Effect on Brownout	102
CHAPTER 6. CONCLUSION, REMARKS, AND FUTURE WORK . . .	131
BIBLIOGRAPHY	133
APPENDIX A. WALL FUNCTIONS	139
A.1 Standard Wall Function	139
A.2 Launder Spalding Wall Function	140
A.3 Turbulence	140
A.4 Wall Function for Rough Wall	141

LIST OF TABLES

Table 2.1	Closure coefficient for Baldwin-Lomax Model	11
Table 2.2	Closure coefficient for Spalart-Allmaras Model	14
Table 2.3	Closure coefficient for Standard $k - \epsilon$ Model	16
Table 2.4	Closure coefficient for Realizable $k - \epsilon$ Model	18
Table 4.1	Coefficient and source term for scalar transport equations	51
Table 5.1	Rotor properties for helicopter in hover	75
Table 5.2	Rotor properties for helicopter with different fuselage shape	95
Table 5.3	Properties of rotor for multi-rotor configurations	103

LIST OF FIGURES

Figure 2.1	Aerodynamic forces on blade section	19
Figure 3.1	Particle size characterization	24
Figure 3.2	Particle size distribution in different regions	25
Figure 3.3	Aerodynamic drag and lift on spherical particle	26
Figure 3.4	Aerodynamic drag coefficient, C_D , as a function of Reynolds number Re_p	27
Figure 3.5	Particle terminal velocity, w_t , Shao (2000) [24]	30
Figure 3.6	Particle threshold friction velocity u_{*t} Iversen et al. (1976) [26]	31
Figure 3.7	Modes of particle transport	33
Figure 3.8	Dust emission mechanism from Shao (2000) [24]	35
Figure 3.9	Dilute vs dense flows Crowe et al. (1998) [25]	40
Figure 3.10	Mass concentration of various particle size ranges at rotor tip location during Sandblaster-2 field test on rotorcraft brownout (from Midwest Research Institute (MRI) technical report (Chatten (2007) [2]))	42
Figure 4.1	The control volume for scalar variable ϕ	47
Figure 4.2	Control volumes of u and v momentum	53
Figure 4.3	Flowchart of Rotorcraft Brownout Model	62
Figure 5.1	u and v velocity at center plane in driven cavity at $Re = 100$	64
Figure 5.2	u and v velocity at center plane in driven cavity at $Re = 400$	64
Figure 5.3	Velocity magnitude contour plot at center plane of driven cavity at Re $= 100$ and 400	65
Figure 5.4	Skin friction coefficient with Reynolds number on flat plate	66

Figure 5.5	Impinging jet simulation set up	67
Figure 5.6	Impinging jet velocity profile	67
Figure 5.7	Velocity magnitude contour plot (impinging jet)	68
Figure 5.8	Reynolds Shear Stress $\overline{u'w'}$ in impinging jet	69
Figure 5.9	Aerodynamic blade load comparisons with Rabbott's experiment at various Θ	70
Figure 5.10	Particle transport by rotor downwash in wind tunnel experiment (Nathan et al. (2008) [44])	72
Figure 5.11	Dust particle distribution predicted by brownout model	72
Figure 5.12	Ground velocity profile for hovering CH-53E rotor	74
Figure 5.13	Ground friction velocity at rotor height $H = 0.5R$	76
Figure 5.14	Ground friction velocity at rotor height $H = 0.75R$	77
Figure 5.15	Ground friction velocity at rotor height $H = 1.0R$	77
Figure 5.16	Ground friction velocity at rotor height $H = 1.5R$	78
Figure 5.17	Ground friction velocity at rotor height $H = 2.0R$	78
Figure 5.18	Ground friction velocity at rotor height $H = 2.5R$	79
Figure 5.19	Ground friction velocity at rotor height $H = 3.0R$	79
Figure 5.20	Ground friction velocity at rotor height $H = 4.0R$	80
Figure 5.21	Ground friction velocity at rotor height $H = 8.0R$	80
Figure 5.22	Velocity magnitude contours at $H = 0.5R$	82
Figure 5.23	Velocity magnitude contours at $H = 1.0R$	83
Figure 5.24	Velocity magnitude contours at $H = 1.5R$	84
Figure 5.25	Velocity magnitude contours at $H = 2.0R$	85
Figure 5.26	Ground velocity profile at different radial location for different rotor heights	86
Figure 5.27	Wall jet velocity at different radial locations	88
Figure 5.28	Dust cloud formation after 5s for rotor-only and rotor-fuselage configuration	90

Figure 5.29	Visualizing dust cloud characteristics	92
Figure 5.30	Dust cloud characteristics seen through rotor center cut plane for rotor-only and rotor-fuselage configurations	93
Figure 5.31	Particle path lines at rotor mid plane for rotor-only and rotor-fuselage configurations	94
Figure 5.32	Four fuselage shapes used	95
Figure 5.33	Ground friction velocity comparison at $H = 0.6R$	96
Figure 5.34	Ground friction velocity comparison at $H = 1.0R$	97
Figure 5.35	Ground friction velocity of different fuselage cross-section at $H = 1.5R$	97
Figure 5.36	Ground friction velocity comparison at $H = 2.0R$	98
Figure 5.37	Ground friction velocity comparison at $H = 3.0R$	98
Figure 5.38	Velocity magnitude and streamlines for different fuselage shapes at $H = 0.6R$	99
Figure 5.39	Velocity magnitude and streamlines for different fuselage shapes at $H = 1.0R$	100
Figure 5.40	Velocity magnitude and streamlines for different fuselage shapes at $H = 1.5R$	101
Figure 5.41	Rotor configurations	102
Figure 5.42	Streamlines in lateral plane for tandem rotor hovering at different heights	104
Figure 5.43	Streamlines in longitudinal plane for tandem rotor hovering at different heights	106
Figure 5.44	Streamlines in lateral plane for tilt rotor hovering at different heights	107
Figure 5.45	Streamlines in longitudinal plane for tilt rotor hovering at different heights	108
Figure 5.46	Streamlines in lateral planes for quad rotor hovering at different heights	109
Figure 5.47	Streamlines on longitudinal plane for quad rotor hovering at different heights	111
Figure 5.48	Ground friction velocity comparison at $H = 1.0R_{ref}$	113
Figure 5.49	Ground friction velocity comparison at $H = 1.5R_{ref}$	113

Figure 5.50	Ground friction velocity comparison at $H = 2.0R_{ref}$	113
Figure 5.51	Ground friction velocity comparison at $H = 2.5R_{ref}$	113
Figure 5.52	Dust cloud comparison for multiple rotor configurations at $H = 1.0R_{ref}$	114
Figure 5.53	Dust cloud comparison for multiple rotor configurations at $H = 1.5R_{ref}$	115
Figure 5.54	Dust cloud comparison for multiple rotor configurations at $H = 2.0R_{ref}$	116
Figure 5.55	Dust cloud comparison for multiple rotor configurations at $H = 2.5R_{ref}$	117
Figure 5.56	Dust cloud characteristics through fuselage lateral mid plane at $H =$ $1.0R_{ref}$	118
Figure 5.57	Dust cloud characteristics through fuselage lateral mid plane at $H =$ $1.5R_{ref}$	118
Figure 5.58	Dust cloud characteristics through fuselage lateral mid plane at $H =$ $2.0R_{ref}$	119
Figure 5.59	Dust cloud characteristics through fuselage lateral mid plane at $H =$ $2.5R_{ref}$	119
Figure 5.60	Dust cloud characteristics through fuselage longitudinal mid plane at $H = 1.0R_{ref}$	120
Figure 5.61	Dust cloud characteristics through fuselage longitudinal mid plane at $H = 1.5R_{ref}$	120
Figure 5.62	Dust cloud characteristics through fuselage longitudinal mid plane at $H = 2.0R_{ref}$	121
Figure 5.63	Dust cloud characteristics through fuselage longitudinal mid plane at $H = 2.5R_{ref}$	121
Figure 5.64	Dust cloud evolution after 2s at $H = 1.0R_{ref}$	123
Figure 5.65	Dust cloud evolution after 3s at $H = 1.0R_{ref}$	124
Figure 5.66	Dust cloud evolution after 5s at $H = 1.0R_{ref}$	125
Figure 5.67	Dust cloud evolution after 7s at $H = 1.0R_{ref}$	126
Figure 5.68	Dust cloud evolution after 10s at $H = 1.0R_{ref}$	127
Figure 5.69	Comparison of tandem rotors with and without fuselage at $H = 1.0R_{ref}$	128

Figure 5.70 Comparison of tilt rotors with and without fuselage at $H = 1.0R_{ref}$. . 129

Figure 5.71 Comparison of quad rotors with and without fuselage at $H = 1.0R_{ref}$. 130

NOMENCLATURE

b	rotor blade span
C_d	drag coefficient
C_l	lift coefficient
c	airfoil chord
d_m, d_p	particle equivalent diameter
g	acceleration due to gravity
k	turbulent kinetic energy
M	local Mach number
p	pressure
p'	pressure correction
Re	Reynolds number
Re_p	particle Reynolds number
S_{rotor}^i	rotor momentum source term
St_v	particle Stokes number
u_i	fluid velocity components
u_{pi}	particle velocity components
U_i	mean fluid velocity components
u'_i	turbulent fluid fluctuating velocity components
u', v'	velocities correction
\hat{u}, \hat{v}	pseudo velocity components
u_r	particle relative velocity
u_*	fluid friction velocity

u_{*t}	particle threshold terminal velocity
V_∞	freestream velocity
\vec{V}	velocity vector
\vec{V}_{flap}	rotor flapping velocity
w_t	particle terminal velocity

Greek Symbols

α	angle of attack
α_p	particle volume fraction
β	rotor flapping angle
ϵ	turbulent dissipation
Γ_d	dust diffusion coefficient
μ	fluid viscosity
μ_t	turbulent eddy viscosity
μ_t^p	turbulent particle eddy viscosity
ν_t	turbulent kinematic eddy viscosity
ϕ	general, scalar transport variable (in rotor modeling used as twist angle)
ρ	fluid density
ρ_p	particle density
ρ_d	dust cloud density
σ_p	particle density ratio
θ_r	rotor blade pitch angle at radius r
τ_{ij}	Reynolds stress tensor $-\overline{\rho u'_i u'_j}$
τ_v	particle velocity response time
τ_F	flow field time characteristics
τ_f	fluid relaxation time
τ_w	ground shear stress

ACKNOWLEDGEMENTS

I would like to acknowledge my advisor, Dr. Ganesh Rajagopalan, for his support and encouragement throughout the entirety of my graduate studies. I would like to thank Air Force Office of Scientific Research (AFOSR) for providing the financial support to carry out my research and graduate studies. In addition, I appreciate all the help and discussion with Dr. William Warmbrodt and Dr. Marvin Moulton and other MURI teams, during the course of research. I express my deepest gratitude to Dr. James D. Iversen for his suggestion and guidance. I would also like to thank my other committee members: Dr. Thomas J. Rudolphi and Dr. Bong Wie. Many thanks are due to the Department of Aerospace Engineering at Iowa State University and its staff for administrative help and computing resources.

I would also like to thank my friends and colleagues, Angela Lestari, Mark Lohry, Janani Murallidharan, and Kanchan Guntupalli for their valuable suggestions and support. Most importantly, I would like to express my deepest appreciation for the support, confidence and love provided to me by my parents. Without them I would not have made it to where I am today.

CHAPTER 1. OVERVIEW

Rotorcraft brownout is in-flight visibility restriction caused by clouds of sand and dust particles during landing, take off, and near ground flight operations in arid desert terrain. This complex phenomenon is caused by entrainment of dust, sand, and ground particles by rotor downwash and is compounded by fuselage geometry and its orientation with respect to the ground. Nonlinear forces and moments on the fuselage, and highly unsteady wind velocities are common in near ground operations and play a significant role in the behavior of the particulate clouds that create the brownout condition.

To date, systematic study of brownout is sparse in literature. Some flight test data on dust distribution for different aircraft are available in Rogers [1] and Chatten [2]. However, in order to computationally simulate this phenomenon, it is first imperative to correctly predict the rotor downwash in different flight conditions. Also important is understanding the physics of particle entrainment and distribution in the brownout dust cloud. Some knowledge can be obtained from the field of riverine and aeoline sedimentology. It has been found that the empirical models used in describing the behavior of suspended particles in water or air can be applied to the helicopter brownout problem also.

Two approaches are popular in studying particle entrainment processes. One is the Lagrangian approach by Keller [3] in which the trajectories of individual particles are tracked and these particles are taken to represent a dust cloud. The dynamics of each individual particle is modeled. Thus, for the overall flow to be reliably represented, a large number of particles must be modeled, thereby making this approach computationally very expensive. In the second approach, the so-called Eulerian approach, overall dynamics of the particle distribution in the air is modeled using suitable transport equations. This approach has been applied to the

brownout problem by Ryerson [4], and Haehnel [5]. All of the above mentioned research use a two-phase model to represent the particle dynamics and assume a one-way coupling between the fluid and the particles, i.e., the fluid affects the particle but not the other way around. Another documented study of the brownout problem was conducted by Phillips and Brown [6]. They used the Vorticity Transport Model (VTM) to solve the rotor flowfield and coupled it with an Eulerian-based dust Transport equation to represent the dust entrainment process. Brown's dust transport model uses empirical correlations borrowed from sedimentology and studies the evolution of particle density distribution and its relation with flowfield velocity and vorticity. This study found the interaction of the tip vortices with the ground is by far the most important contributor to the formation of the initial dust cloud. Therefore, the vorticity and velocity profile in the rotor wake are crucial. Phillips et al [7] determined them to be affected by parameters like solidity and blade twist. From these studies it can be concluded that the geometric properties of the rotor have a great influence on the type and extent of the dust cloud formed. Although VTM is found to be a good model in predicting the rotor downwash, no fuselage effect is considered in this study. Since it is based on empirical correlations, the dust transport model has room for further investigation.

Another approach, ([8], [9]) employs a real-time free wake model, coupled with a dust and debris model, that uses analytical methods in a Lagrangian framework. This model results in a real-time brownout simulator that gives pilots a feel for the brownout cloud formed under different flight conditions, ground cover and type of aircraft. A visual obscuration model, based on a light scattering method, is also used to visualize brownout and train pilots accordingly. However, the Lagrangian approach makes this approach computationally expensive.

One of the important factors in developing a dust transport model that can be used in conjunction with a Computational Fluid Dynamics (CFD) code is the development of a suitable entrainment function to describe the entrainment flux. Haehnel [10] studied the physics of particle entrainment under the influence of an impinging jet and determined the driving force for particle entrainment is the Reynolds stress associated with the turbulent fluctuations of the flow. Since an impinging jet is similar to the wake of the rotor in ground effect, it can

be deduced that solving correctly for the turbulent fluctuations in the rotor's flowfield is an important step in solving the brownout problem. Thus, a complete brownout model that incorporates all the components of brownout as observed in reality is yet to be developed.

1.1 Current Research

The goal of this current research is to develop a computational test bed to study fuselage and rotor configuration effects on brownout. The emphasis of the simulation approach has been on

- global flow field rather than on the flow near the rotor blades.
- body influence on the brownout and on the inception of particle entrainment.

Brownout is a complex phenomenon with multiple scales and physics dictating the physics of the simulation. The complex phenomenon involves aerodynamic processes like ground effect on rotor wake, turbulent burst, surface wall jet, tip vortices, and their interactions. These aerodynamic interactions, coupled with the interaction of the particles, become a complex multi-phase phenomenon. In addition to the rotor-induced vortical wake, there are unsteady effects, due to the bluff body underneath the rotor as well as the dynamics of the particles that complicate the simulation. Hence, to study this behavior accurately as well as economically, judicious compromises and an engineering approach to the complete physics are required.

Accuracy of the simulation, particularly close to the ground where particle entrainment takes place, is highly dependent upon the turbulence characteristics and ground shear predicted by the mathematical models used. Since the phenomenon is inherently three-dimensional, a three-dimensional flow solver has been developed for studying various turbulence models. Many variants of turbulence models are considered and implemented in the solver before settling on the final choice for studying the fuselage configuration effects on rotorwash and brownout. In addition, a solution procedure for dust cloud evolution and dynamics has been developed.

To accurately and economically predict the turbulent flow field, incompressible Reynolds Averaged Navier Stokes (RANS)-based solver has been developed in the Cartesian coordinate

system. In the solver, the governing flow equations are solved using a finite-volume based method known as SIMPLER ([11]). In this algorithm, the flow field is determined by solving for primitive variables, namely the static pressure and the velocity vector, directly from the mass and momentum conservation equations.

To solve for the Reynolds turbulent stresses, additional relations or partial differential equations (PDE) are solved, known as turbulence models. In general, these turbulence model can be broadly classified [12] into Zero Equation models, One Equation models and Two Equation models. These models are also known as linear eddy viscosity models, as they assumes a linear relationship between turbulent eddy viscosity and the mean strain rate. Other complex RANS-based models, such as Reynolds Stress models [13], Non-linear Models [14] etc. can also be found in the literature. Since there has not been much research on the applicability of these models on rotorcraft brownout flows, it has been decided to use linear eddy viscosity models for the current research because of their relatively low complexity and low computational cost. Although these models are most widely used for many industrial flow problems, one of the drawbacks of these models is that it assumes isotropic character of turbulence, which may be erroneous for the anisotropic turbulence condition found in brownout.

1.1.1 Turbulence models

Zero Equation models, as the name denotes, do not solve any partial differential equation. Instead, turbulent viscosity is solved using an algebraic equation. On the other hand, One Equation and Two Equation models solve one and two partial differential equations, respectively. In general, complexity and accuracy of linear eddy viscosity models increases with the number of equations solved. A candidate model from each of these categories has been selected, implemented, and tested.

Zero Equation Model (Baldwin Lomax Model) This model implementation is straightforward for simple single body flows. It gives acceptable results for simple attached flow with mild separation and re-attachment. The eddy viscosity is calculated as a function of turbulent length scale (l_t) and turbulent velocity scale (v_t), both are semi-empirically mod-

eled. Length scale is of the order of the boundary layer thickness calculated using vorticity distribution; thus, eliminating the need to calculate the boundary layer thickness explicitly. However the model does not perform well where turbulence properties are not proportional to the mean flow length scale, such as in flows with strong separation and recirculation. The model is computationally very efficient.

One Equation Model (Spalart Allmaras Model) One equation model overcomes some of the problems of the Zero Equation Model by solving the transport equation for turbulent viscosity-like variables. Since a transport equation is solved, it captures the effects of convection and diffusion of turbulence. Thus, the flow downstream is affected by the upstream turbulence. However, this model still needs to semi-empirically model the length scale to complete the equations. This is achieved by making the source term (destruction term) as a function of distance from the nearest wall. This model gives better results for wall-bounded flows, separated flows, and boundary layer flows with adverse pressure gradients. However, calculation of an additional equation increases the computational requirement and storage of additional variables.

Two Equation Model (Standard and Realizable $k - \epsilon$ Model) Solving two equations avoids the dependence on empirical and semi-empirical algebraic formulations for both turbulent velocity and length scales. The two coupled partial differential equation are solved for turbulent kinetic energy, k , and turbulent dissipation, ϵ . This model is widely used for a variety of turbulent flows involving separation and re-attachment, and flows with complex turbulent characteristics. However, solving two additional equations requires more computational time and memory.

1.1.2 Rotor model

To model the rotor, the method developed by Rajagopalan and Fanucci, Rajagopalan and Lim, and Rajagopalan and Mathur [15, 16, 17] has been used, where the rotor's influence is considered as a momentum source which imparts momentum to the fluid flow around it. The

momentum source is time averaged and its magnitude depends upon the rotor's geometry and flow characteristics around the rotor. The advantage of this model is that there is no need of a body fitted grid around the rotor; thus, reducing the memory and computational time requirements. In the time averaged model of the rotor used in this study the effect of discrete blades are not captured.

1.1.3 Dust transport model

The transport of dust has been modeled by the multiphase species transport equation. Since the number of dust particles during brownout is immense, dust particle transport is assumed to be in a continuum phase and is solved in the Eulerian frame of reference. The advantage of modeling dust in such a manner reduces the computational requirements and memory. Also, the coupling between particle and flow phase has been considered as a one-way coupled system, where the particles are affected by the flow and the particles do not have any effect on the flow. The modeling of dust lift-off criteria, entrainment, and saltation are accomplished through empirical formulation used in geophysical research. The particle velocity field is calculated through an Algebraic slip model, which calculates the relative particle velocity using an algebraic expression.

In summary, all of the aforementioned models have been integrated into a single program, Rotorcraft Brownout Model (RBM). In the present research, RBM has been used to study the following problems:

1. Study of various turbulence models on rotorcraft problems in ground effect.
2. Effects of fuselage on rotor wake, ground signature and brownout.
3. Different rotor configurations and ground height effect on rotor wake, ground signature, and brownout.

CHAPTER 2. TURBULENT ROTOR FLOW MODELING

2.1 Reynolds Average Navier-Stokes (RANS) Equation

The equation for conservation of mass and momentum of incompressible rotor flow field is given by

$$\frac{\partial u_i}{\partial x_i} = 0 \quad (2.1)$$

$$\frac{\partial \rho u_i}{\partial t} + \frac{\partial \rho u_i u_j}{\partial x_j} = -\frac{\partial p}{\partial x_i} + \frac{\partial t_{ij}}{\partial x_j} + S_{rotor}^i \quad (2.2)$$

where ρ is density, x_i is position, u_i is velocity, p is pressure, and t is time. The term t_{ij} is viscous stress tensor given by

$$t_{ij} = 2\mu S_{ij} \quad (2.3)$$

where μ is molecular viscosity and s_{ij} is the strain rate tensor given by

$$S_{ij} = \frac{1}{2} \left(\frac{\partial u_i}{\partial x_j} + \frac{\partial u_j}{\partial x_i} \right) \quad (2.4)$$

S_{rotor}^i is the rotor momentum source term used to model the rotor (discussed in section 2.3).

The above set of equations form the incompressible Navier-Stokes equation and can be used to solve for laminar as well as turbulent flows. However, most of the practical turbulent flows contain cascades of eddies with a wide range of time and length scales. Direct Numerical Simulation (DNS) is a numerical method, which resolves all the length and time scales of turbulent motion using very fine grids. Large Eddy Simulation (LES) is another numerical technique, in which the larger eddies are resolved; whereas, the smaller turbulent structures are modeled. Nevertheless, in case of complex flows, such as rotor flows, both of the above methods need an impractical degree of grid refinement and simulation time for design use.

An alternate approach is to solve for the *time averaged* mean flow as introduced by Reynolds. In this concept, the instantaneous velocity, u_i , in an inhomogeneous turbulence can be expressed in terms of mean velocity, U_i , and fluctuating velocity, u'_i .

$$u_i = U_i + u'_i \quad (2.5)$$

The mean velocity U_i is the time averaged velocity defined as

$$U_i = \lim_{T \rightarrow \infty} \left[\frac{1}{2T} \int_{-T}^T u_i dt \right] \quad (2.6)$$

where T is a time interval large enough compared to the turbulent length scale, but smaller than the time in which the time-averaged mean flow varies. Also, the time average of the fluctuating velocity is zero.

$$\lim_{T \rightarrow \infty} \left[\frac{1}{2T} \int_{-T}^T u'_i dt \right] = 0 \quad (2.7)$$

Replacing the instantaneous velocity, u_i , in the Navier-Stokes equation with the sum of time averaged velocity, U_i , and fluctuating velocity, u'_i , and then taking the time average of the equation yields **Reynolds Average Navier-Stokes (RANS)** equations.

$$\frac{\partial U_i}{\partial x_i} = 0 \quad (2.8)$$

$$\frac{\partial \rho U_i}{\partial t} + \frac{\partial \rho U_i U_j}{\partial x_j} = -\frac{\partial p}{\partial x_i} + \frac{\partial}{\partial x_j} \left(2\mu S_{ij} - \overline{\rho u'_i u'_j} \right) + S_{rotor}^i \quad (2.9)$$

where $-\overline{\rho u'_i u'_j}$ is the time average of product of fluctuating velocities and are called **Reynolds Stresses**, denoted by τ_{ij} .

$$\tau_{ij} = -\overline{\rho u'_i u'_j} \quad (2.10)$$

wherein τ_{ij} is a symmetric tensor, i.e., $\tau_{ij} = \tau_{ji}$.

The RANS equations are not closed form equations. The Reynolds stresses, τ_{ij} , are six additional unknowns, that need to be calculated to complete the RANS equations. Additional relationships or equations are required to relate or calculate τ_{ij} in terms of known or calculated

variables. These additional relations or equations are the main essence of turbulence modeling.

2.2 Eddy Viscosity-based Turbulence Model

According to Boussinesq's hypothesis, the turbulent Reynolds stress is related linearly to the mean strain-rate tensor of the fluid flow. Analogous to viscous stress, the proportionality factor is called turbulent viscosity or eddy viscosity, μ_t . Boussinesq's hypothesis for incompressible flow is

$$\tau_{ij} = 2 \mu_t S_{ij} - \frac{2}{3} \rho k \delta_{ij} \quad (2.11)$$

where the term $\frac{2}{3} \rho k \delta_{ij}$ is a linear constitutive relation used while solving two-equation models or models which solve for turbulent kinetic energy, k . Turbulent kinetic energy is defined as

$$k = \frac{1}{2} \left(\overline{u_1'^2} + \overline{u_2'^2} + \overline{u_3'^2} \right) \quad (2.12)$$

Using Boussinesq's hypothesis, the RANS (Eq. 2.9) equation becomes

$$\frac{\partial \rho U_i}{\partial t} + \frac{\partial \rho U_i U_j}{\partial x_j} = - \frac{\partial p}{\partial x_i} + \frac{\partial}{\partial x_j} \left[(\mu + \mu_t) \left(\frac{\partial U_i}{\partial x_j} + \frac{\partial U_j}{\partial x_i} \right) \right] - \frac{2}{3} \frac{\partial k}{\partial x_i} + S_{rotor}^i \quad (2.13)$$

Thus, using the above assumption, the problem of finding Reynolds stress reduces to determination of eddy viscosity. Unlike molecular viscosity, μ , eddy viscosity, μ_t , depends on local flow characteristics, mainly the local turbulent length scale and velocity scale. The eddy viscosity is calculated using various eddy viscosity-based turbulence models which can be broadly categorized, depending upon the number of transport equations being solved.

- Zero Equation Models (Cebeci-Smith Model, Baldwin-Lomax Model)
- One Equation Models (Baldwin-Barth Model, Spalart-Allmaras Model)
- Two Equation Models ($k - \epsilon$ Model, $k - \omega$ Model)

In the current research, one representative model from each category, i.e., Baldwin-Lomax Model, Spalart-Allmaras Model, and $k - \epsilon$ has been implemented and tested.

2.2.1 Baldwin-Lomax Model

The Baldwin-Lomax model [12, 18] is a two-layer algebraic zero-equation eddy viscosity model, which gives the eddy viscosity, μ_t , as a function of the local boundary layer velocity profile. The earlier zero-equation models require determination of the outer edge of boundary layer to calculate the length scale for boundary layer and wakes. This problem is eliminated in this model as it uses the vorticity distribution to compute the required length scales. One of the major disadvantages of this model is it is unable to capture the time history effect of turbulence, such as convection and diffusion, because no transport equation is being solved. This model is quite robust and useful for simpler flow geometries.

Equations: The turbulent viscosity is given as

$$\mu_t = \begin{cases} \mu_{t_{inner}} & \text{if } y \leq y_m \\ \mu_{t_{outer}} & \text{if } y > y_m \end{cases} \quad (2.14)$$

where y_m is the smallest distance from the surface, where $\mu_{t_{inner}}$ is equal to $\mu_{t_{outer}}$. The inner region is given by the Prandtl - Van Driest formula:

$$\mu_{t_{inner}} = \rho l_{mix}^2 |\omega| \quad (2.15)$$

where mixing length l_{mix} is given by

$$l_{mix} = ky \left(1 - e^{-\frac{y^+}{A^+}} \right) \quad (2.16)$$

where y^+ is non-dimensional height calculated as $y^+ = \sqrt{\tau_w/\rho} y/\nu$. A^+ is a constant.

$|\omega|$ is magnitude of vorticity given by

$$|\omega| = \sqrt{2\omega_{ij}\omega_{ij}} \quad (2.17)$$

where

$$\omega_{ij} = \frac{1}{2} \left(\frac{\partial u_i}{\partial x_j} - \frac{\partial u_j}{\partial x_i} \right) \quad (2.18)$$

The outer region is given by:

$$\mu_{t_{outer}} = \rho K C_{cp} F_{wake} F_{Kleb}(y) \quad (2.19)$$

where K and C_{cp} are constants. F_{wake} is given as

$$F_{wake} = MIN \left(y_{max} F_{max} ; C_{wk} y_{max} \frac{u_{dif}^2}{F_{amax}} \right) \quad (2.20)$$

where C_{wk} is a constant.

$$F_{max} = \frac{1}{\kappa} [max_y(l_{mix} |\omega|)] \quad (2.21)$$

where y_{max} is y at which $l_{mix} |\omega|$ is a maximum.

F_{Kleb} is the intermittency factor given by:

$$F_{Kleb}(y) = \left[1 + 5.5 \left(\frac{y C_{Kleb}}{y_{max}} \right)^6 \right]^{-1} \quad (2.22)$$

where C_{Kleb} is a constant.

u_{dif} is the difference between maximum and minimum speed in the profile. For boundary layers, the minimum is always set to zero.

$$u_{dif} = max(\sqrt{u_i u_i}) - min(\sqrt{u_i u_i}) \quad (2.23)$$

The values of closure coefficient used in this model is given in Table 2.1.

Table 2.1 Closure coefficient for Baldwin-Lomax Model

A^+	26
C_{cp}	1.6
C_{Kleb}	0.3
C_{wk}	0.25
κ	0.4
K	0.0168

2.2.2 Spalart-Allmaras Model

Spalart-Allmaras Model [19] is a one-equation eddy viscosity model which solves a transport equation for a viscosity-like variable, $\tilde{\nu}$, used to calculate kinematic turbulent viscosity, ν_t .

Equations: Kinematic turbulent eddy viscosity, ν_t , is related to $\tilde{\nu}$ as:

$$\nu_t = \tilde{\nu} f_{v1} \quad (2.24)$$

where

$$f_{v1} = \frac{\chi^3}{\chi^3 + C_{v1}^3}, \quad \chi = \frac{\tilde{\nu}}{\nu} \quad (2.25)$$

The intermediate variable $\tilde{\nu}$ is calculated using the transport equation:

$$\frac{\partial \rho \tilde{\nu}}{\partial t} + \frac{\partial \rho u_j \tilde{\nu}}{\partial x_j} = S_{diffusion} + S_{production} - S_{destruction} + S_{trip} \quad (2.26)$$

where $S_{diffusion}$ is a diffusion term, $S_{production}$ is the source term due to turbulence production, $S_{destruction}$ is the sink term due to turbulence destruction, and S_{trip} is a trip term used for turbulence transition.

The diffusion term is defined as

$$S_{diffusion} = \frac{\rho}{\sigma} \left[\frac{\partial}{\partial x_j} \left((\nu + \tilde{\nu}) \frac{\partial \tilde{\nu}}{\partial x_j} \right) + C_{b2} \frac{\partial \tilde{\nu}}{\partial x_i} \frac{\partial \tilde{\nu}}{\partial x_i} \right] \quad (2.27)$$

The production source term depends upon vorticity and allows good modeling near the wall.

$$S_{production} = \rho C_{b1} [1 - f_{t2}] \tilde{S} \tilde{\nu} \quad (2.28)$$

where C_{b1} is a constant. \tilde{S} is given by

$$\tilde{S} = S + \frac{\tilde{\nu}}{\kappa^2 d^2} f_{v2}, \quad f_{v2} = 1 - \frac{\chi}{1 + \chi f_{v1}} \quad (2.29)$$

d is distance from nearest wall and S is magnitude of vorticity given by

$$S = \sqrt{2\Omega_{ij}\Omega_{ij}}, \quad \Omega_{ij} = \frac{1}{2}\left(\frac{\partial u_i}{\partial x_j} - \frac{\partial u_j}{\partial x_i}\right) \quad (2.30)$$

f_{t2} is given by

$$f_{t2} = C_{t3} \exp(-C_{t4}\chi^2) \quad (2.31)$$

where C_{t3} and C_{t4} are constants.

The destruction term depends upon the nearest wall distance, d .

$$S_{destruction} = \rho \left[C_{w1}f_w(r) - \frac{C_{b1}}{\kappa^2}f_{t2} \right] \left(\frac{\tilde{\nu}}{d} \right)^2 \quad (2.32)$$

The term $f_w(r)$ calibrates the outer region of boundary layer and depends upon the characteristic length r , and is given by:

$$f_w = g \left[\frac{1 + C_{w3}^6}{g^6 + C_{w3}^6} \right]^{1/6}, \quad g = r + C_{w2}(r^6 - r), \quad r = \frac{\tilde{\nu}}{\tilde{S}\kappa^2 d^2} \quad (2.33)$$

where C_{w2} and C_{w3} are constants.

The trip term is modeled as

$$S_{trip} = \rho f_{t1} \Delta U^2 \quad (2.34)$$

where ΔU^2 is a norm between the velocity at transition and field point considered. f_{t1} is given by

$$f_{t1} = C_{t1}g_t \exp\left(-C_{t2}\frac{\omega_t^2}{\Delta U^2}[d^2 + g_t^2 d_t^2]\right) \quad (2.35)$$

In the current research, the tripping terms f_{t1} and f_{t2} have been neglected (set to zero).

The values of closure coefficient is given in Table 2.2

2.2.3 $k - \epsilon$ Models

$k - \epsilon$ model is a two-equation turbulence model which solves two transport equations for turbulent kinetic energy, k , and turbulent dissipation, ϵ . Unlike zero-equation and one-equation

Table 2.2 Closure coefficient for Spalart-Allmaras Model

σ	2/3
C_{b1}	0.1355
C_{b2}	0.622
κ	0.41
C_{w1}	$C_{b1}/\kappa + (1 + C_{b2})/\kappa$
C_{w2}	0.3
C_{w3}	2.0
C_{v1}	7.1
C_{t1}	1.0
C_{t2}	2.0
C_{t3}	1.1
C_{t4}	2.0

models, the two-equation model is also called a “complete” turbulence model since it solves for both turbulence length scale and velocity scale, instead of relating it to some flow properties. The turbulence length scale is taken as $k^{3/2}/\epsilon$ and velocity scale is approximated as $k^{1/2}$. Using these, the turbulent viscosity can be calculated as

$$\mu_t = C_\mu \rho \frac{k^2}{\epsilon} \quad (2.36)$$

where C_μ is a model constant in Standard $k - \epsilon$ model with value of 0.09.

Many variant of $k - \epsilon$ model are discussed in the literature. These formulations mainly differ in the method of calculating turbulent velocity, calculation of source term (both generation and destruction term) of ϵ -equation and model constants. In this research two variants of the $k - \epsilon$ model have been used. The first is the original and the most popular model, developed by Launder and Spalding [20] well known as the *Standard $k - \epsilon$* model. The other model is relatively new, proposed by Shih [21], known as *Realizable $k - \epsilon$* model.

2.2.3.1 Standard $k - \epsilon$ model

The Standard $k - \epsilon$ model is a semi-empirical model in which the equation for turbulent kinetic energy, k , is derived from the exact equation; whereas, the transport equation for ϵ is more of a mathematical expression obtained from physical reasoning. This model is only valid

for fully turbulent flows.

Equations: Transport equation for turbulent kinetic energy is given by

$$\frac{\partial}{\partial t}(\rho k) + \frac{\partial}{\partial x_i}(\rho k u_i) = \frac{\partial}{\partial x_j} \left[\left(\mu + \frac{\mu_t}{\sigma_k} \right) \frac{\partial k}{\partial x_j} \right] + P_k - \rho \epsilon \quad (2.37)$$

where P_k is the production term for turbulent kinetic energy and $\rho \epsilon$ is the destruction term due to turbulent dissipation.

The transport equation for turbulent dissipation is given by

$$\frac{\partial}{\partial t}(\rho \epsilon) + \frac{\partial}{\partial x_i}(\rho \epsilon u_i) = \frac{\partial}{\partial x_j} \left[\left(\mu + \frac{\mu_t}{\sigma_\epsilon} \right) \frac{\partial \epsilon}{\partial x_j} \right] + C_{1\epsilon} \frac{\epsilon}{k} P_k - C_{2\epsilon} \rho \frac{\epsilon^2}{k} \quad (2.38)$$

where $C_{1\epsilon} \frac{\epsilon}{k} P_k$ is the production and $C_{2\epsilon} \rho \frac{\epsilon^2}{k}$ is the destruction of turbulent dissipation.

The production term P_k is modeled as

$$P_k = -\overline{\rho u'_i u'_j} \frac{\partial u_j}{\partial x_i} = \tau_{ij} \frac{\partial u_i}{\partial x_j} \quad (2.39)$$

Using Boussinesq's hypothesis, P_k can be related to mean rate of strain tensor $S = \sqrt{2S_{ij}S_{ij}}$ as

$$P_k = \mu_t S^2 \quad (2.40)$$

Calculating turbulent production term using Eq.2.40 may cause overproduction in turbulent kinetic energy in highly accelerated or decelerated regions and the stagnation regions. To overcome this problem, Kato and Launder [22] proposed an ad-hoc modification to the production term of turbulent kinetic energy equation. Kato and Launder proposed to replace one of the strain rate, S , with vorticity, Ω , to modify the production term as

$$P_k = \mu_t S \Omega \quad (2.41)$$

where Vorticity Ω is given as

$$\Omega = \sqrt{\frac{1}{2} \left(\frac{\partial u_i}{\partial x_j} - \frac{\partial u_j}{\partial x_i} \right)^2} \quad (2.42)$$

The values of coefficient used are listed in Table 2.3.

Table 2.3 Closure coefficient for Standard $k - \epsilon$ Model

$C_{1\epsilon}$	1.44
$C_{2\epsilon}$	1.92
C_μ	0.09
σ_k	1.0
σ_ϵ	1.3

2.2.3.2 Realizable $k - \epsilon$ model

The Standard $k - \epsilon$ model may sometimes violate two mathematical constraints on Reynolds Stresses based on the physics of turbulent flows. Using Boussinesq hypothesis, normal Reynolds stress for an incompressible flow can be written as

$$\overline{\rho u'^2} = -2\mu_t \frac{\partial U}{\partial x} + \frac{2}{3}k \quad (2.43)$$

The normal Reynolds Stress $\overline{\rho u'^2}$, a positive quantity, may become negative or non-realizable if the strain is high as

$$\frac{k}{\epsilon} \frac{\partial U}{\partial x} = \frac{1}{3C_\mu} \approx 3.7 \quad (2.44)$$

Another defect of the Standard $k - \epsilon$ model (Shih (1995) [21]) is it may violate the Schwarz inequality for shear stresses $\overline{u'_\alpha u'_\beta} \leq \overline{u'^2_\alpha u'^2_\beta}$ at a high strain rate.

To overcome these deficiencies in the Standard $k - \epsilon$ model, two modifications have been adopted in the Realizable $k - \epsilon$ model as follows:

1. A new transport equation for turbulent dissipation (new production and destruction term) based on the dynamic equation of the mean-square vorticity fluctuation.
2. A new eddy viscosity formulation in which C_μ is a variable.

Equations: The transport equation for turbulent kinetic energy is given by

$$\frac{\partial}{\partial t}(\rho k) + \frac{\partial}{\partial x_i}(\rho k u_i) = \frac{\partial}{\partial x_j} \left[\left(\mu + \frac{\mu_t}{\sigma_k} \right) \frac{\partial k}{\partial x_j} \right] + P_k - \rho \epsilon \quad (2.45)$$

The equation for turbulent dissipation is given by

$$\frac{\partial}{\partial t}(\rho\epsilon) + \frac{\partial}{\partial x_j}(\rho\epsilon u_j) = \frac{\partial}{\partial x_j} \left[\left(\mu + \frac{\mu_t}{\sigma_\epsilon} \right) \frac{\partial \epsilon}{\partial x_j} \right] + \rho C_1 S \epsilon - \rho C_2 \frac{\epsilon^2}{k + \sqrt{\nu \epsilon}} \quad (2.46)$$

where $\rho C_1 S \epsilon$ is the new production term and $\rho C_2 \frac{\epsilon^2}{k + \sqrt{\nu \epsilon}}$ is the new destruction term for turbulent dissipation. The term C_1 is given as

$$C_1 = \max \left[0.43, \frac{\eta}{\eta + 5.0} \right], \quad \eta = S \frac{k}{\epsilon}, \quad S = \sqrt{2 S_{ij} S_{ij}} \quad (2.47)$$

The transport equation for turbulent kinetic energy is the same as the Standard $k - \epsilon$ model. The only difference is in the calculation of the source term of dissipation equation. One of the remarkable features noted in the ϵ equation is it does not contain the P_k in production source term. It is believed this helps to better represent the spectral energy transfer [23]. Also, the singularity problem of destruction term in the ϵ equation of the Standard $k - \epsilon$ model (when $k = 0$) does not exist because of the modified destruction term.

The turbulent viscosity is modeled the same as Eq. 2.36 but with the variable, C_μ . C_μ is given by

$$C_\mu = \frac{1}{A_0 + A_s \frac{k U^*}{\epsilon}} \quad (2.48)$$

$$U^* \equiv \sqrt{S_{ij} S_{ij} + \tilde{\Omega}_{ij} \tilde{\Omega}_{ij}}, \quad \tilde{\Omega}_{ij} = \Omega_{ij} - 2 \epsilon_{ijk} \omega_k, \quad \Omega_{ij} = \bar{\Omega}_{ij} - \epsilon_{ijk} \omega_k \quad (2.49)$$

$\bar{\Omega}_{ij}$ is the mean rate-of-rotation tensor viewed in a rotating reference frame with the angular velocity ω_k .

The constants A_0 and A_s are given by:

$$A_0 = 4.04, \quad A_s = \sqrt{6} \cos \phi \quad (2.50)$$

where

$$\phi = \frac{1}{3} \cos^{-1}(\sqrt{6}W), \quad W = \frac{S_{ij} S_{jk} S_{ki}}{\tilde{S}^3}, \quad \tilde{S} = \sqrt{S_{ij} S_{ij}}, \quad S_{ij} = \frac{1}{2} \left(\frac{\partial u_j}{\partial x_i} + \frac{\partial u_i}{\partial x_j} \right) \quad (2.51)$$

The values of the coefficient used in the Realizable $k - \epsilon$ Model are given in Table 2.4.

Table 2.4 Closure coefficient for Realizable $k - \epsilon$ Model

$C_{1\epsilon}$	1.44
$C_{2\epsilon}$	1.9
σ_k	1.0
σ_ϵ	1.2

2.3 Rotor Source Modeling

In the present research, the method developed by Rajagopalan and Fanucci, Rajagopalan and Lim, and Rajagopalan and Mathur [15, 16, 17], where the rotor has been treated as a momentum source is adopted. The rotor is modeled as the momentum source term, S_{rotor}^i , and is added to the momentum equation at the point where the blades pass. The magnitude of the source term is a function of rotor geometry, blade cross-sectional aerodynamic characteristics, and the local flow field.

$$S_{rotor}^i = S_{rotor}^i(C_l, C_d, \alpha, \dot{\alpha}, \vec{V}, \Omega, x, y, z, \rho, \mu, Re, M, b, c) \quad (2.52)$$

The source term is time averaged and individual blades are not recognized. Explicit details of the chordwise flow over rotor blade are not resolved.

To calculate rotor source term, the rotor is discretized into a spanwise element. The blade properties, like chord length, airfoil thickness, plane deflection, and cross-sectional area are assumed to be constant over the element. The source term is added to the grid cells, where the blade pass while the rotor spins. A brief description of rotor source calculation is shown here. More details can be found in Rajagopalan and Lim [16] and Rajagopalan and Mathur,[17].

2.3.1 Rotor source calculation

The rotor source term is calculated by computing the rotor force using the local angle of attack and Mach number at each spanwise element. This is achieved by finding the C_l and C_D values from a lookup table for the given airfoil at that particular angle of attack and Mach

number. If $\vec{V} = V_x \hat{e}_x + V_y \hat{e}_y + V_z \hat{e}_z$ is the velocity vector at position (x, y, z) , where the

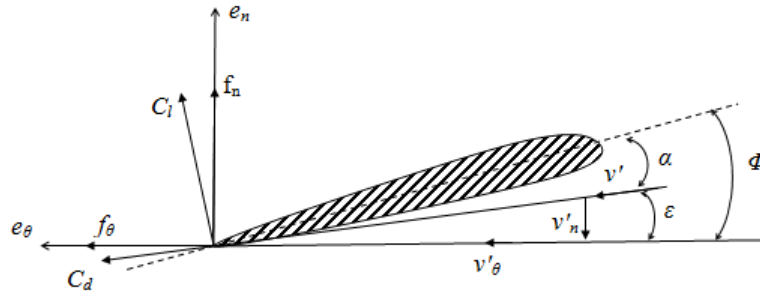


Figure 2.1 Aerodynamic forces on blade section

rotor passes, then it can be transferred to the blade coordinate system (n, θ, s) , such that the velocity vector in rotor plane becomes

$$\vec{V}' = v_n \hat{e}_n + v_\theta \hat{e}_\theta + V_s \hat{e}_s \quad (2.53)$$

If the rotor blade is flapping about the flapping hinge, then the tangential velocity of the center of the blade element, with respect to the flapping hinge, is given by

$$\vec{V}_{flap} = (\dot{\beta} R_f) \hat{e}_n \quad (2.54)$$

where R_f is the radial distance from the hinge offset and $\dot{\beta}$ is the flapping rate. In general, the flapping motion of the blade is given by the flapping angle, β , represented as a Fourier series of azimuthal angle ψ as

$$\beta = a_0 + \sum_{n=1}^N (a_n \cos n\psi + b_n \sin n\psi) \quad (2.55)$$

From the above equation the flapping rate can be calculated as

$$\dot{\beta} = \frac{\partial \beta}{\partial \psi} \omega \quad (2.56)$$

where ω is the angular velocity of rotor. Using the Eq. 2.53 and 2.54 the flow velocity relative

to the blade is given as

$$\begin{aligned}\vec{V}_{rel} &= \vec{V} - (\vec{V}_{bl} + \vec{V}_{flap}) \\ &= v'_n \hat{e}_n + v'_\theta \hat{e}_\theta + V'_s \hat{e}_s\end{aligned}\quad (2.57)$$

where \vec{V}_{bl} is the velocity of the blade in (n, θ, s) coordinate.

The local angle of attack, α , at any spanwise position, s , is given by

$$\alpha = \phi - \epsilon \quad (2.58)$$

where ϵ is inflow angle given by

$$\epsilon = \arctan(-v'_n/v'_\theta) \quad (2.59)$$

The twist angle, ϕ , at that section can be determined from the rotor blade geometry twist and from cyclic pitch variation of the blade root section θ_r as

$$\theta_r = A_0 + \sum_{n=1}^N (A_n \cos n\psi + B_n \sin n\psi) \quad (2.60)$$

The local Mach number is calculated from

$$M' = v'/a \quad (2.61)$$

where a is the speed of sound and v' is the relative velocity seen by the airfoil section which is $v' = \sqrt{v'^2_n + v'^2_\theta}$. After calculating the local Mach number and local angle of attack, the aerodynamic coefficients, C_l and C_d , are obtained from the airfoil lookup table. Determining the aerodynamic coefficients in this manner implicitly allows the compressibility effect on the aerodynamic characteristics of the blade section.

Hence, the lift and drag in the directions, \hat{e}_n and \hat{e}_θ , can be calculated as

$$\begin{aligned} f_n &= L \cos \epsilon - D \sin \epsilon \\ f_\theta &= L \sin \epsilon + D \sin \epsilon \end{aligned} \quad (2.62)$$

where L and D are given by

$$\begin{aligned} L &= \frac{1}{2} \rho v'^2 C_{lC} ds \\ D &= \frac{1}{2} \rho v'^2 C_{dC} ds \end{aligned} \quad (2.63)$$

The resultant force can be transformed to the computational domain to obtain the resultant force acting on the blade \vec{F} . The force acting on the fluid is $-\vec{F}$ which is added to the momentum source term. However, in the steady (time-averaged) rotor source model, this force is distributed to the computational cells passed by the rotor blade. The fraction of the force added to the cells is calculated as follows.

If t_{rev} is the time period of rotation of rotor, i.e., $t_{rev} = 2\pi/\omega$, then the time the blade element spends in a control volume with width $\Delta\theta$ is given by

$$t_{\Delta\theta} = \frac{\Delta\theta}{\omega} \quad (2.64)$$

Then, the fraction of the time blade element spends in a cell is

$$t_{frac} = \frac{\Delta\theta}{2\pi} \quad (2.65)$$

If there are N_b blades, then the time averaged source term is given by

$$\vec{S} = \frac{N_b \Delta\theta}{2\pi} (-F) \quad (2.66)$$

CHAPTER 3. DUST TRANSPORT MODELING

Dust particle entrainment during rotorcraft brownout is a process of soil particle movement by the aerodynamic force of impinging rotor downwash with distinct phases of particle lift-off, transport, and deposition. There are many factors which affect the physics of the process, which includes strength of rotor downwash, ground signature, aerodynamic roughness length, land-surface topography, soil texture, soil composition, etc. Although the phenomenon of particle entrainment and transport takes place in most of the surface types, the intensity and magnitude of entrainment is intense in desert arid region, where the percentage of dust in the soil is high and surface vegetation does not restrict the motion of particles.

One of the closely related physical phenomenon to rotorcraft brownout can be found in the geophysical process of aeolian sedimentology and particle transport. There have been a number of studies completed in the geophysical research group, which deals with the behavior of particle motion and transport by air as well as water. Although the basic physics of particle motion, both in geophysical process and rotorcraft brownout, remains the same, the condition in which this process takes place is different. In the geophysical level, flow is mainly parallel to the ground; whereas, in the brownout scenario, the flow impinges on the ground with many other complex aerodynamic processes. Development of mathematical formulations of wind erosion problem under rotor flow is scarce in literature. The present research uses a mathematical formulation based on empirical and semi-empirical relations from the geophysical research group. Most of the mathematical relations discussed in this chapter are related to wind erosion, Shao (2000) [24]. To model the transport of particles in the rotor flow field, the particle motion is modeled as a multi-phase flow. The governing equation for particle transport has been taken from the multi-phase research group, which formulates air as the

carrier medium and particle as the discrete medium ([25]).

3.1 Particle Characteristics

The particle transport process involves various complex interactions, like particle-flow interaction, particle-particle interaction, and particle-surface interaction. The behavior of these interactions are influenced by various physical properties of particles, like shape, size, density, terminal velocity, threshold velocity, etc.

3.1.1 Equivalent particle diameter

The particle size is one of the major factors determining particle transport behavior and characterization. In general, particle size is closely related to particle shape. The shape of a particle can be very irregular and varies from sphere to plates, very angular to well-rounded, and from rough to smooth in their texture. These properties can be defined by various morphological parameters, like sphericity, roundness, and surface roughness. However, it can be extremely difficult to precisely determine the size of the particle unless the shape is well defined. A simple and efficient way to characterize the particle is through **equivalent particle size or diameter**. Equivalent particle size of a particle is the diameter of the equivalent sphere which retains certain aerodynamic or optical properties as identical to the particle. Equivalent particle diameter can be based on mass, volume terminal velocity, drag, etc. For example, mass equivalent and volume equivalent diameter are:

$$d_m = \left(\frac{6m}{\pi \rho_p} \right)^{1/3} \quad d_v = \left(\frac{6V}{\pi} \right)^{1/3} \quad (3.1)$$

where m is particle mass, V is the particle volume, and ρ_p is the particle density. The choice of the type of particle equivalent diameter depends upon the problem studied. For the current research, equivalent diameter, based on drag and terminal velocity, is the most appropriate.

Based on the size, a particle can be characterized among roughly four categories as shown in Figure 3.1, i.e., gravel ($2000\mu m < d \leq 2m$), sand ($60 < d \leq 2000\mu m$), slit ($2 < d \leq 60\mu m$),

and clay ($d \leq 2\mu m$) (based on MIT and British Standards Institute). For simplicity, in the current work the particles have been divided in two categories - sand and dust. Sand particles ($d > 100\mu m$) are those particles, which are relatively heavier and cannot be suspended in the air for long time. They are deposited back in the ground, due to the gravitational effect, but they play a major role in dust entrainment by the process known as saltation. Dust particles ($d < 100\mu$) are those, which are relatively smaller and play a major role in forming dust clouds. Because of lower terminal velocity of dust particles, they are carried by the flow for longer distance and time, particularly by the effect of turbulent eddies.

		0.002	0.006	0.02	0.06	0.2	0.6	2.0mm		
British Standard Institution	CLAY	Fine	Medium	Coarse	Fine	Medium	Coarse	GRAVEL		
		SILT			SAND					
International Society of Soil and Science	CLAY	SILT			SAND			GRAVEL		
				Fine	Coarse					
		0.002	0.006	0.02	0.06	0.2	0.6	2.0mm		
		0.002		0.05	0.10	0.25	0.5	1.0	2.0mm	
United States Department of Agriculture	CLAY	SILT			VF	Fine	M	C	VC	GRAVEL
		SAND								
United States Public Roads Administration	CLAY	SILT			SAND				GRAVEL	
				Fine	Coarse					
		0.002		0.05	0.10	0.25	0.5	1.0	2.0mm	

Figure 3.1 Particle size characterization

Generally soil contains distribution of particle sizes which is represented by particle size distribution density function $p(d)$, Figure 3.2. If $P(d)$ is probability (or mass fraction) of particle with diameter less than d , then

$$P(d) = \int_0^d p(d)\delta d \quad (3.2)$$

Given the particle size distribution function of a given soil, the mass fraction of any range of size can be calculated. For example, mass fraction of a particle size between d_a and d_b is given

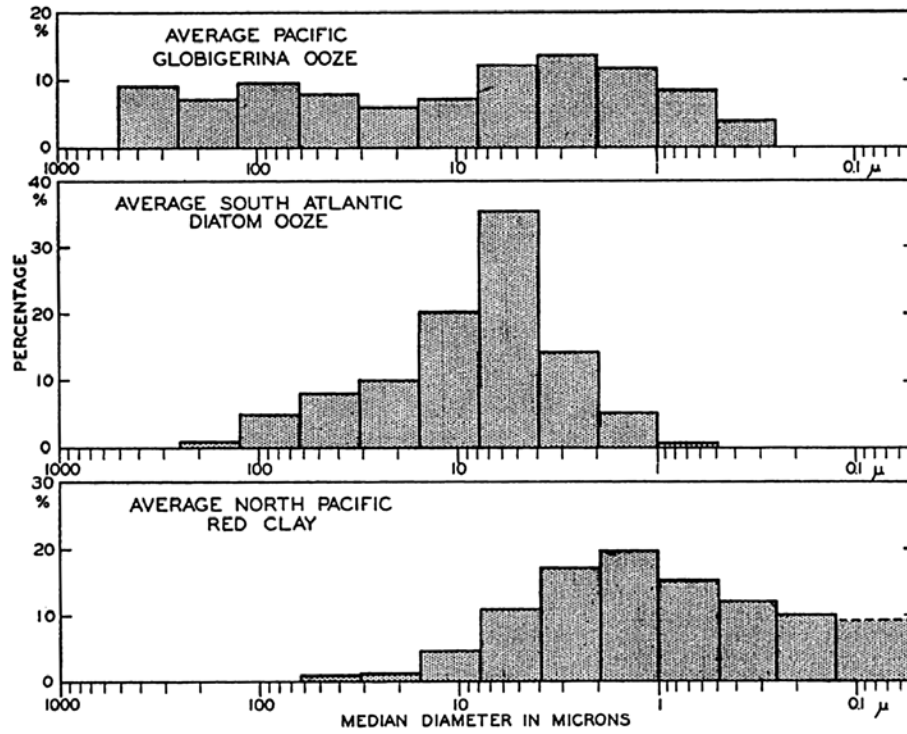


Figure 3.2 Particle size distribution in different regions

by

$$P(d_b) - P(d_a) = \int_{d_a}^{d_b} p(d) \delta d \quad (3.3)$$

3.1.2 Forces on particle

Various forces acting on a particle include

- Gravitational Force F_g
- Aerodynamics Drag F_d
- Aerodynamics Lift F_l
- Buoyancy Force F_b
- Magnus Force F_m
- Electrostatic Force F_e

- Particle-Particle Interaction F_p

Gravitational force is due to gravity, which is simply the weight of the particle acting vertically.

$$F_g = -mg \quad (3.4)$$

where g is the acceleration due to gravity.

Aerodynamic drag is produced when a particle moves relative to the surrounding fluid, creating a pressure difference Δp between frontal and wake regions, Figure 3.3. Additional force is also exerted by shear σ_{ij} of the fluid on the surface.

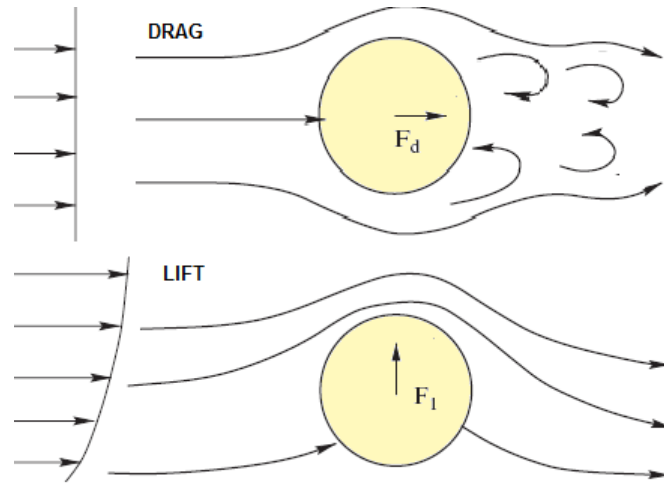


Figure 3.3 Aerodynamic drag and lift on spherical particle

$$F_{di} = - \int_S p n_i dS + \int_S \sigma_{ij} n_j dS \quad (3.5)$$

The above equation for aerodynamic drag can be quantified by using drag coefficient C_D by

$$F_d = \frac{1}{2} \rho C_D A |u_r| U_r \quad (3.6)$$

where $u_r = u - u_p$ is the relative velocity of particle, A is the representative area, and u_p is particle velocity.

Aerodynamic drag coefficient C_D is the function of the particle Reynolds number, $Re_p = \rho u_r d / \mu$, Figure 3.4. There has been numerous studies completed on the relationship between C_D and Re_p . In general, if $Re_p \ll 1$, then it is assumed to be Stokes flow. For this region, C_D varies inversely with Re_p . With increasing Re_p , C_D reaches a constant value around 0.45. Known as the inertial region, this region is between $750 < Re_p < 3.5 \times 10^5$. At a much higher Reynolds number, $Re_p > 3 \times 10^5$, there is a sudden decrease in the C_D value to around 0.1, due to turbulence.

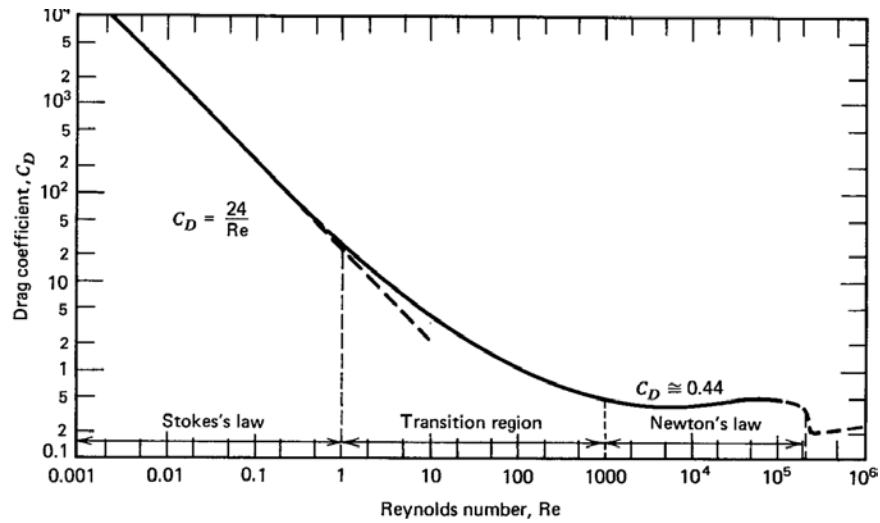


Figure 3.4 Aerodynamic drag coefficient, C_D , as a function of Reynolds number Re_p

At Stokes flow region, the flow is a creeping flow, where the inertial effect can be neglected. The governing equation in this region can be given by

$$\frac{\partial p}{\partial x_i} = \mu \frac{\partial^2 u_i}{\partial x_i \partial x_j} \quad (3.7)$$

By solving the above equation for flow over a spherical particle, force due to pressure can be found as

$$F_p = \pi \mu d_p U \quad (3.8)$$

where U is free stream velocity. Similarly, the shear force can be calculated as

$$F_\tau = 2\pi\mu d_p U \quad (3.9)$$

Thus, total drag force in Stokes region can be given as

$$F_d = 3\pi\mu d_p U \quad (3.10)$$

and in terms of relative velocity,

$$F_d = 3\pi\mu d_p u_r \quad (3.11)$$

Using the F_d , the drag coefficient for Stokes flow can be found as

$$C_D = \frac{24}{Re_p} \quad (3.12)$$

With an increase in Reynolds number, the inertial forces become more significant and the drag coefficient is higher than Stokes drag. In the current work, a simpler expression of $C_D(Re_p)$ is used

$$C_D = \frac{24}{Re_p} f_{drag} \quad (3.13)$$

where f_{drag} is known as the drag function and can be calculated as [25]

$$f_{drag} = \begin{cases} 1 + 0.15Re_p^{0.687} & \text{if } Re_p \leq 1000 \\ 0.0183Re & \text{if } Re_p > 1000 \end{cases} \quad (3.14)$$

Similar to aerodynamic drag, aerodynamic lift is produced due to a difference in pressure above and below the particle, due to difference in velocity (Bernoulli's effect) as shown in Figure 3.3. Aerodynamic lift can also be approximately calculated [24] through

$$F_l = \frac{1}{2} C_l \rho A (\nabla U^2) d \quad (3.15)$$

where ∇U^2 is a gradient of U and C_l is the aerodynamic lift coefficient roughly proportional to C_D , as $C_l = 0.85C_D$.

The buoyancy force, F_b , on the particle is proportional to the density ratio of the particle to fluid. In the present case, the density of particle is of the order of 10^3 ; whereas, the density of fluid is of the order of 1. Since the density ratio is of the order of 10^3 , F_b has been neglected.

Magnus force, F_m , is force caused by rotation of the particle and acts perpendicular to both the direction of motion and rotation. Electrostatic force, F_e , is caused by electrostatic charge on particle and electric field near the surface. In the present work, F_l, F_m and F_e have been neglected.

Particle-particle F_p interaction can occur for two reasons. The first is due to particle-particle collision, which happens when the particle density is high. This also is neglected in the current research. The other interaction is caused by a cohesive force, due to inter-molecular attraction. This force is dominant when particle size is small.

3.1.3 Particle terminal velocity

Particle terminal velocity is the particle to fluid relative velocity, when the aerodynamic forces balance the gravitational force on the particle [24]. At this instance, the particle experiences zero acceleration $du_{pi}/dt = 0$. Neglecting all external forces, except the aerodynamic drag force, F_d , and gravitation force, F_g , the simplified equation for particle motion can be written as

$$m \frac{du_{pi}}{dt} = 3\pi\mu d_p f_{drag} u_{ri} + \delta_{i3} mg \quad (3.16)$$

Using the expression for f_{drag} from Eq. (3.13), the equation of particle motion can be written as

$$\frac{du_{pi}}{dt} = \frac{f_{drag}}{\tau_v} u_{ir} + \delta_{i3} g \quad (3.17)$$

where τ_v is the **particle velocity response time**,

$$\tau_v = \frac{\rho_p d_p^2}{18\mu} \quad (3.18)$$

Applying $du_{pi}/dt = 0$ in Eq. (3.17), horizontal components of terminal velocity are found to be zero. The vertical component, w_t , is

$$w_t = \frac{g\tau_v}{f_{drag}} \quad (3.19)$$

Using Eq. (3.13) and Eq. (3.18), the vertical terminal velocity can be written as

$$w_t = \frac{4gd_p\sigma_p}{3C_D(Re_{pt})w_t} \quad (3.20)$$

where $\sigma_p = \rho_p/\rho$ is the particle density ratio. $Re_{pt} = w_t d_p/\nu$ is particle Reynolds number at terminal velocity. In general, the above equation is an implicit equation in w_t , since C_D is the function of Re_{pt} , which, in turn, is a function of w_t . This equation is solved using numerical iteration. In the special case for flow around Stokes region, $C_D = 24/Re_p$ and, thus, $w_t = \sigma_p g d_p^2 / 18\nu$. At a very high Reynolds number, $C_D = 0.48$ and $w_t = 1.66(\sigma_p g d_p)^{(1/2)}$. Plot showing the variation of terminal velocity with particle diameter at three different density ratios are shown in Figure 3.5.

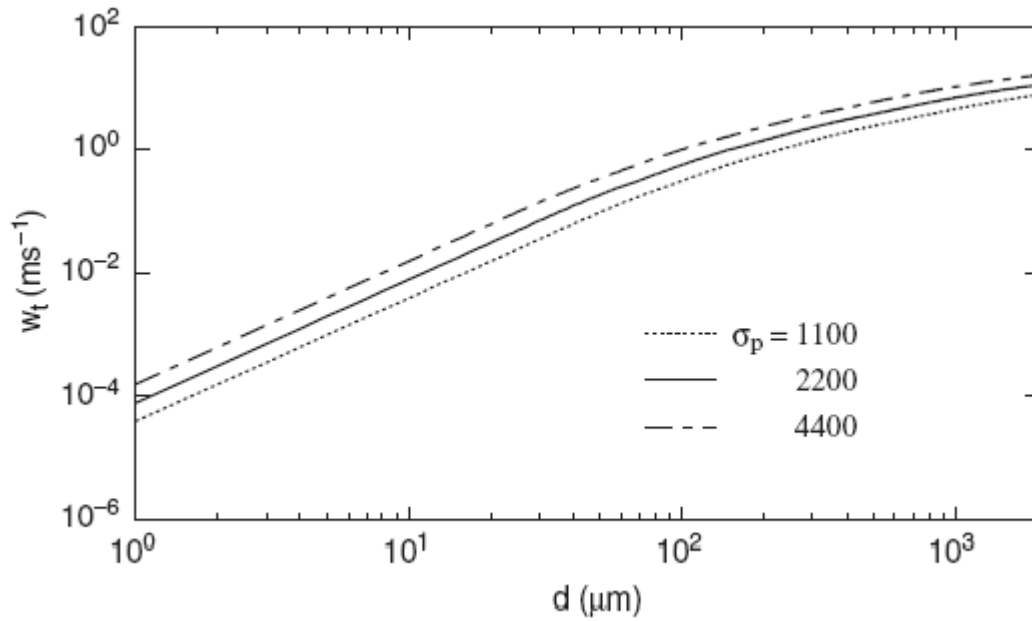


Figure 3.5 Particle terminal velocity, w_t , Shao (2000) [24]

3.1.4 Particle threshold friction velocity

Particle threshold friction velocity, u_{*t} , is the minimum friction velocity, $u_* = \sqrt{\tau_w/\rho}$, required to give the initial motion to the particle on the ground against the retarding gravitational force and cohesive forces. The forces which drive the initial motion are mainly

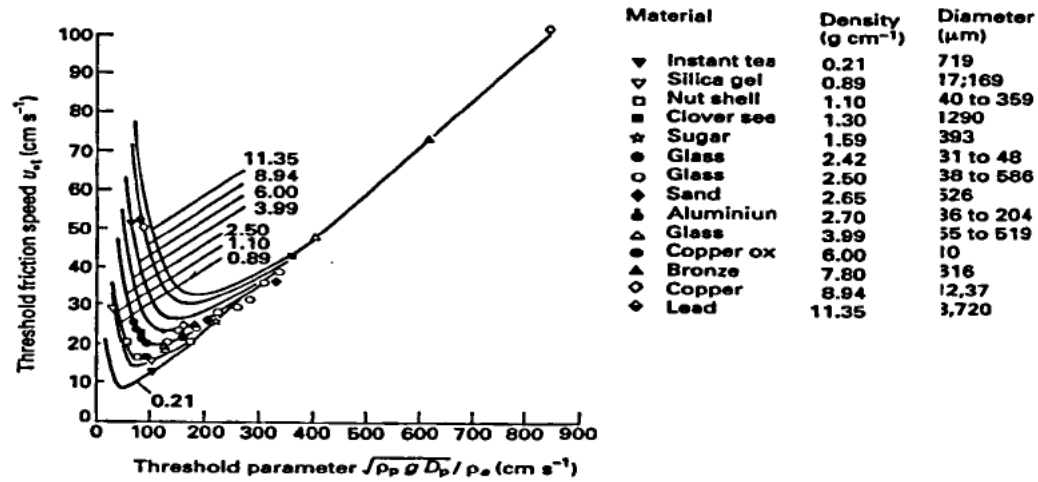


Figure 3.6 Particle threshold friction velocity u_{*t} Iversen et al. (1976) [26]

the aerodynamic drag F_d and lift F_l , which are directly proportional to wall shear near the ground. Particle threshold velocity depends upon capacity of the surface to resist wind erosion, essentially a function of surface properties. In general, threshold velocity depends on various factors like

- Particle diameter (d_p)
- Particle size distribution ($p(d)$)
- Particle density (ρ_p)
- Fluid density (ρ)
- Impact of impinging particle (air, water)
- Particle friction Reynolds number (Re_*)

There have been many theories developed to calculate the threshold friction velocity. One of the earliest theories, known as **Bagnold Scheme** [27] or **Bagnold Formulae**, was proposed by Ralph Alger Bagnold (founder and first commander of the British Army's Long Range Desert Group during World War II).

$$u_{*t} = A_B \sqrt{\sigma_p g d_p} \quad (3.21)$$

where the coefficient $A_B = A_B(Re_{*t})$ depends on particle threshold Reynolds number ($Re_{*t} = u_{*t} d_p / \nu$). It was found empirically to be in the range of 0.1 and 0.2. A problem with this scheme was it predicts a lower threshold friction velocity for particles below the viscous sub layer. Later Greeley and Iversen [28] hypothesized that A_B is not constant but is a function of aerodynamic drag and the inter particle cohesive force.

$$A_B = A_1 F(Re_{*t}) G(d) \quad (3.22)$$

where $G(d)$ is the function which takes cohesive force into account. The threshold friction velocity for different particle types are plotted in Figure 3.6.

Very recently Lu and Shao [29] proposed that under ideal conditions, u_{*t} can be described as a function of particle property alone

$$u_{*t} = \frac{1}{\kappa} \sqrt{a_1 \left(\frac{\rho_p}{\rho} g d_p + \frac{a_2}{\rho d_p} \right)} \quad (3.23)$$

where κ represents a surface roughness factor taken to be 1.0 in this current research. From experiments the value of the coefficient a_1 and a_2 are found to be approximately 0.0123 and $3 \times 10^{-4} kgs^{-2}$, respectively. In the current research the above semi-empirical expression for u_{*t} has been used.

3.2 Modes of Particle Transport

Based on different categories of particle and flow condition, the particle adopts a different type of transport mechanism [24] (Figure 3.2).

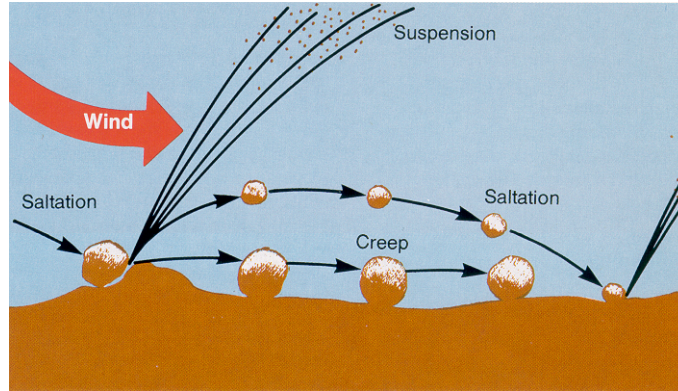


Figure 3.7 Modes of particle transport

- ***Suspension***

This type of particle transport is common among relatively smaller particles, referred to as dust particles here. Once the particle has lift-off from the ground, it stays in the air for a longer time and travels longer distance. Due to its low terminal velocity, it is easily influenced by turbulent fluctuating velocities. Thus, for this type of particle, turbulent diffusion plays a very important role in the transport mechanism. For most geophysical processes, particles below $\lesssim 70\mu m$ are considered to have a suspension type of motion. Also, if the terminal velocity of the particle is very small compared to the vertical turbulent velocity, then the particle follows the suspension mode. If the vertical terminal velocity is approximated as κu_* , then the particle goes to suspension, if $w_t/\kappa u_* \ll 1$.

- ***Saltation***

When fluid friction velocity is higher than the threshold friction velocity, the relatively larger sand particle is entrained into the flow. Since the terminal velocity is large for these particles, they fall to the ground, due to gravitational force. While in flight these particles extract momentum from the flow and hit the ground with higher energy. This

impact further intensifies the emission of more particles and dust into the flow. Thus, this mechanism plays a very important role in dust particle entrainment.

The layer in which saltating particles moves is called *saltation layer*. The thickness of this layer, known as saltation layer thickness (z_m), is the maximum height the saltating particle attains. The height of the saltation layer depends upon the friction velocity. As predicted by Owen [30], saltation layer thickness can be given by

$$z_m = c \frac{u_*^2}{2g} \quad (3.24)$$

where c is a constant assumed to be 1.6. Owen also hypothesized the saltation layer behaves as a rough surface with roughness length, z_{os} , proportional to the saltation layer thickness, z_m , for the flow above the saltation layer.

- **Creep**

Larger particles $> 1,000\mu m$ are too heavy to be lifted by aerodynamic force. These particles roll (or creep) along the ground. One of the major causes of surface creep is the momentum imparted to the heavy particles from the impact of saltating particles.

3.2.1 Dust emission mechanism and modeling

So far in this chapter, various characteristics and properties of all sizes of particle have been described. Since much anecdotal evidence suggests that in the case of brownout, relatively small, fine, powder-like particles are the main ingredient of the brownout cloud [6], focus of this research will be on dust particles. In general, there are three mechanisms of dust emission as depicted in Figure 3.8.

1. **Aerodynamic Lift** This occurs when aerodynamic lift is large enough to pick the dust particles from the ground. Generally, these particles are very small, where the gravitational and aerodynamic lift are much smaller; whereas, the cohesive force can be dominant. Dust emission, due to this mechanism, is small.

2. ***Saltation Bombardment*** As discussed before, when the saltating particle falls on the ground, due to high momentum content, it transfers energy to the dust particles, which helps overcome the binding forces. The dust emission, due to this mechanism, is an order in magnitude higher than aerodynamic lift.
3. ***Disaggregation*** This happens when sand particles coated with dust disintegrate under strong wind erosion.

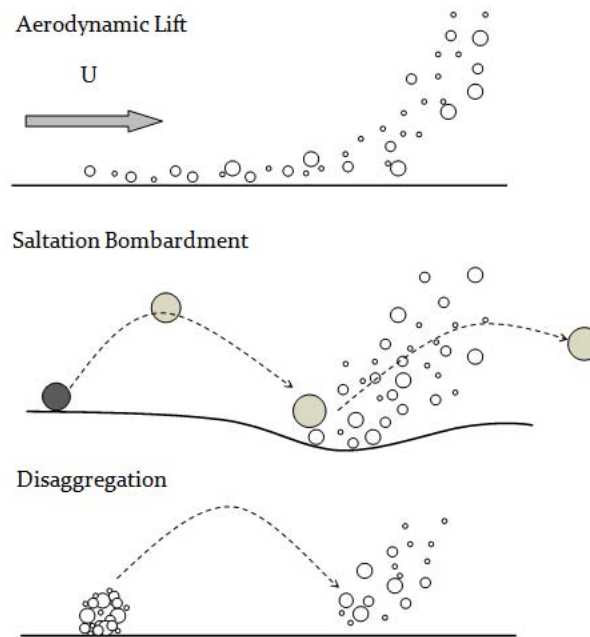


Figure 3.8 Dust emission mechanism from Shao (2000) [24]

3.2.2 Vertical particle flux

Experiments conducted by Nalpanis [31] showed vertical particle flux, F , decreases exponentially with height.

$$F = F_o e^{\frac{-\lambda g z}{u_*^2}} \quad (3.25)$$

where F_o is vertical particle flux at ground, z is the height from ground, and λ is a parameter which around 50%. Through various field measurement with different kinds of soils accom-

plished by Gillette [32], it was found that F_o is proportional to u_*^n , where n varies between 2.9 and 4.4 depending on soil type. Based on this relation, there has been a number of dust emission schemes proposed by various researchers. Although a generalized scheme has not been developed due to the large numbers of parameters involved, it has been found that dust emission is directly linked with intensity of saltation and indirectly related to the binding strength of dust particles. For the current research, a scheme proposed by Marticorena and Bergametti [33] has been used. The vertical particle flux depends upon saltation or horizontal particle flux Q as

$$F_o = Qe^{13.4f-6.0} \quad (3.26)$$

where f is percentage of clay in soil. For this research $f = 0.1$ was used.

Similar to vertical particle flux, saltation flux also depends on friction velocity u_* . The present research uses a model developed by Bagnold [27] to calculate the saltation flux Q .

$$Q = \begin{cases} 0 & \text{if } u_* < u_{*t} \\ \frac{c_o \rho}{g} u_*^3 \left(1 - \frac{u_{*t}^2}{u_*^2}\right) & \text{if } u_* \geq u_{*t} \end{cases} \quad (3.27)$$

where $c_o = 0.25 + \frac{0.33w_t}{u_*}$.

As discussed earlier, particle entrainment happens when ground friction velocity, u_* , is greater than threshold friction velocity, u_{*t} . The friction velocity is calculated from ground stress as $u_* = \sqrt{(\tau_w/\rho)}$. In most geophysical research, like uniform steady parallel flow, the ground stress is calculated from the gradient of mean flow velocity (the first moment of velocity field). But, in the experiment conducted by Haehnel [10] on particle entrainment under impinging jet, it was found that there was significant particle entrainment in the jet centerline stagnation zone, where the wall stress based on gradient of mean flow velocity is zero. Instead of wall stress based on first moment of velocity field, Haehnel found the driving force of the particle entrainment is the Reynolds stress, $\overline{v'w'}$ (second moment of velocity field), due to turbulent velocity fluctuation. Although, Reynolds stress is same as average shear stress based

on the mean velocity field for steady parallel flows, it does not go to zero at the stagnation region, as in the case of impinging jet. Haehnel also suggested the relationship of the Reynolds stress with the turbulent kinetic energy as $\overline{v'w'} = 0.2k$. The current research uses Reynolds stress, as suggested by Haehnel, to calculate the dust flux.

3.3 Dust Transport Modeling

A system or flow consisting of a mixture solid, liquid and gas phases is called a multiphase system or flows. Multiphase flows can be classified into different categories, depending upon the nature of the system or the flow regime. Based on the phases involved, multiphase flows can be classified [34, 25] into various categories.

- Gas liquid flows
- Gas solid flows
- Liquid solid flows
- Three phase flows

In the case of rotorcraft brownout, flow can be considered as a solid-gas multiphase turbulent dispersed flow, where air is the carrier phase and dust is the discrete phase. Both phases have separately defined volume fraction and velocity field. Conservation equations for the flow of each phase are solved to get the density and velocity field. Transfer of mass, momentum, and energy between the phases are taken care through coupling between the phases.

The two different theoretical models used to solve multiphase flows are Eulerian-based multi-fluid model and Lagrangian-based particle tracking model. In both models the fluid is solved as a continuum phase. In the Eulerian-based model, a cloud of dust is also solved as continuum, where as in the Lagrangian-based model each dust particle is treated as an independent entity and the trajectories are calculated individually.

The advantages and disadvantages of both of these models have been described by many researchers (Durst et al (1984) [35], Shirolkara et al. (1996) [36], Crowe et al. (1996) [37]). In

the Lagrangian-based model, since each particle is tracked separately, this model gives good insight into particle dynamics. A disadvantage with this model is it becomes computationally expensive when the number of particles is large. The Eulerian-based approach for particle transport is easy to interpret and is computationally more efficient, since it solves an additional transport equation for the discrete phase.

Mathematical modeling of multiphase flows depends on various properties of dispersed phase flows. Some of the important properties which apply specifically to particle-gas flows are described next.

3.3.1 Particle Stokes number

Stokes number is a dimensionless number which gives an idea of particle behavior in fluid particle flows. The Stokes number of a particle can be defined as

$$St_v = \frac{\tau_v}{\tau_F} \quad (3.28)$$

where τ_v is particle velocity response time given in Eq. 3.18 and τ_F is time characteristic of flow field which can be given by

$$\tau_F = \frac{L_{ref}}{U_{ref}} \quad (3.29)$$

where U_{ref} is the reference velocity of the flow field and L_{ref} is characteristic reference length.

If $St_v \ll 1$, then the response time for particles to react to a change in flow behavior is small. So particles will have enough time to respond to the change in flow and the particle will have almost the same velocity as that of fluid (velocity equilibrium). If $St_v \gg 1$, then particle response time is high and relative velocity of the particle with respect to the flow will be significant. An approximate relation between particle velocity, fluid velocity, and Stokes number is given by

$$\frac{u_p}{u} \sim \frac{1}{1 + St_v} \quad (3.30)$$

It can be seen as $St_v \rightarrow 0$, particle velocity attains fluid velocity; whereas, when $St_v \rightarrow \infty$, the particle velocity approaches zero.

3.3.2 Particle volume fraction

Particle volume fraction, α_p , is defined as volume of the particle per unit volume.

$$\alpha_p = \lim_{\delta V \rightarrow \delta V^o} \frac{\delta V_p}{\delta V} \quad (3.31)$$

where δV_p is the volume of the particle in the volume.

3.3.3 Particle bulk density (Dust cloud density)

Particle bulk density is the mass of particle per unit volume of mixture. In this current work, it has also been reported as **Dust Cloud Density**, ρ_d .

$$\rho_d = \lim_{\delta V \rightarrow \delta V^o} \frac{\delta M_p}{\delta V} \quad (3.32)$$

where δM_p is the mass of particle in volume. Dust cloud density is related to particle volume fraction, α_p , and particle density, ρ_p , as

$$\rho_d = \alpha_p \rho_p \quad (3.33)$$

3.3.4 Particle loading

The ratio of mass flux of particle to that of mass flux of fluid is called loading Z .

$$Z = \frac{\dot{M}_p}{\dot{M}_f} \quad (3.34)$$

where \dot{M}_p is the mass flow rate of particle and \dot{M}_f is the mass flow rate of fluid. For small Stokes number it can be approximated as $Z = \rho_d / \rho$.

3.3.5 Dilute versus dense flows and phase coupling

Dilute flow is a flow where the motion of a particle is governed by the forces acting upon them by the fluid, whereas in a dense flow particle motion is governed by the collisions. In

general, if particle collision time, τ_c , is very large compared to particle response time, τ_v , then the flow is called dilute flow, otherwise, it is a dense flow.

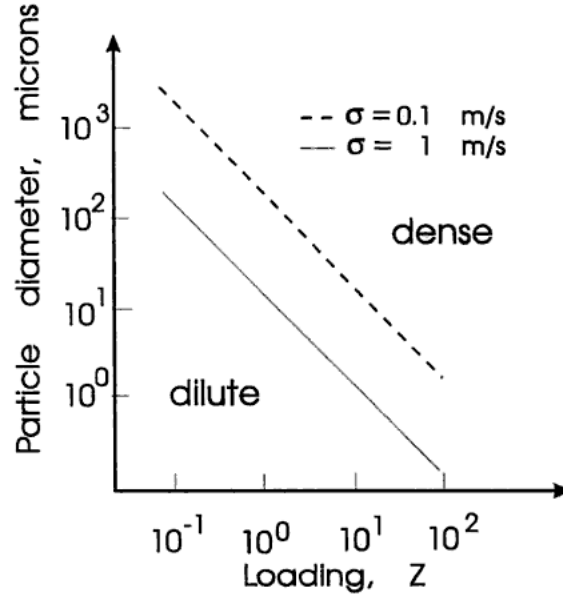


Figure 3.9 Dilute vs dense flows Crowe et al. (1998) [25]

Another way to differentiate dilute flow from dense flow [25] can be given in terms of particle diameter as

$$d_p < \frac{3\mu}{Z\rho u_r} \quad (3.35)$$

This relation is depicted in the Figure 3.9. For turbulent flows the relation can be given in terms of standard deviation, σ , of particle fluctuation velocity as

$$d_p < \frac{1.33\mu}{Z\rho\sigma} \quad (3.36)$$

The exchange of mass, momentum, and energy between phases is governed by phase coupling parameter. Since in the rotorcraft brownout case there is no phase change of particle, mass coupling is not considered. Similarly, energy coupling is also neglected in this present research. Three types of momentum coupling can be considered.

1. *One-way coupling*: Particle is influenced by fluid through aerodynamic drag; whereas

fluid is not being affected by the presence of particles.

2. *Two-way coupling*: Both particle and fluid affect each other through aerodynamic drag and turbulence transfer.
3. *Four-way coupling*: In addition to two-way coupling, particle-particle collision is also taken into consideration.

The type of coupling required for modeling multiphase flows varies from problem-to-problem. In general, one-way coupling is straightforward and efficient. Requirement of two- or four-way coupling is estimated through parameter magnitude estimation, which generally depends upon factor-like particle loading Z , particle Stokes number St_v , particle bulk density ratio $C = \rho_d/\rho$, etc.

One of the commonly used parameters to decide upon the coupling is known as *momentum coupling parameter*, Π_{mom} . An approximate definition of momentum coupling parameter is given by Crowe et al. (1998) [25]

$$\Pi_{mom} = \frac{C}{1 + St_v} \quad (3.37)$$

If $\Pi_{mom} \ll 1$, then coupling of momentum between phases is insignificant, and one way coupling is used.

3.3.6 Rotorcraft Brownout Model

From the field studies achieved by Chatten [2] (Midwest Research Institute), on brownout cloud characteristics on six rotorcraft configurations at the Yuma Proving Ground (YPG), it was found that brownout dust cloud contains particles ranging from $2\mu m$ to larger than $350\mu m$ (Figure 3.10). The mass concentration (mg/m^3) at rotor tip location for various particle sizes ranges from $10mg/m^3$ to $700mg/m^3$.

Based on these test data and other anecdotal reports, it can be inferred that the major contributor to brownout clouds is a relatively smaller particle ($0 - 62\mu m$), since number of particle per unit volume (number density) is highest. High particle number density causes

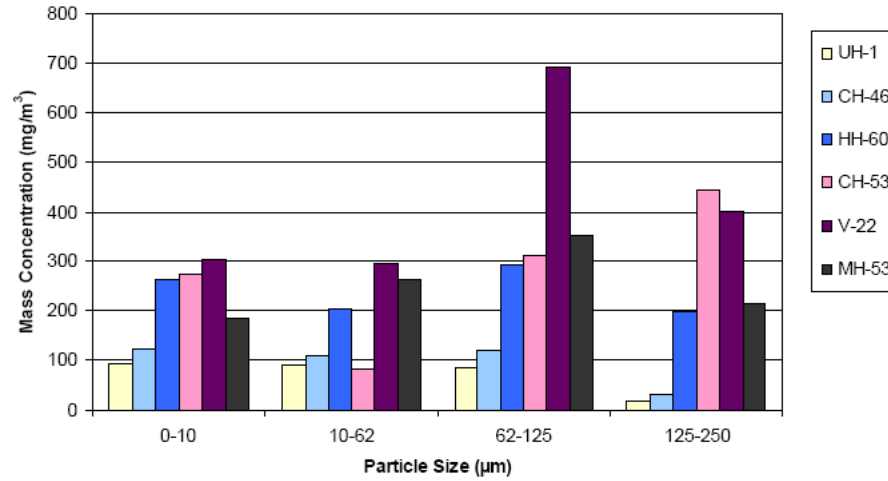


Figure 3.10 Mass concentration of various particle size ranges at rotor tip location during Sandblaster-2 field test on rotorcraft brownout (from Midwest Research Institute (MRI) technical report (Chatten (2007) [2]))

more scattering of light, thus causing visibility problems. Therefore, the focus of this current research is on relatively small dust particles.

Particle Stokes Number in brownout: Considering particle density of $\rho_p = 2800 \text{ kg/m}^3$ and air viscosity of $\mu = 1.7 \times 10^{-5}$, the particle response time varies from $9 \times 10^{-4} \text{ s} \lesssim \tau_v \lesssim 3.5 \times 10^{-2} \text{ s}$ for particle range of $10 \mu\text{m}$ to $62 \mu\text{m}$. Time characteristic of fluid τ_F can be found in the range of $0.15 \text{ s} \lesssim \tau_F \lesssim 0.6 \text{ s}$, using $L_{ref} = 6 - 12 \text{ m}$ (rotor radius) and $U_{ref} = 20 - 40 \text{ m/s}$ (wall jet velocity or rotor-induced velocity). Based on the time characteristics of particle and fluid, the particle Stokes number varies between $1.5 \times 10^{-3} \lesssim St_v \lesssim 0.23$. This shows the Stokes number is $St_v < 1$ for all dust particle sizes and $St_v \ll 1$ for smaller dust particles.

Particle loading in brownout: At a lower Stokes number, particle loading is approximated as $Z = \rho_d/\rho$. As seen from the test data, particle loading is of the order of $Z \sim 10^{-3}$, the brownout flow condition can be considered as a dilute flow.

Phase coupling in brownout: With particle bulk density ratio $C = \rho_d/\rho < 7^{-4}$, momentum coupling parameter $\Pi_{mom} \ll 1$. Accordingly, flow can be considered as one-way coupled. However, the particle bulk density ratio has been found to be comparatively large

near the ground, which is better suited for two-way coupling. Irrespective of this, since this zone (saltation and entrainment zone) of high bulk density ratio is generally much smaller compared to the overall flow field, two-way coupling has been ignored for this region.

Considering the above properties of particle discrete phase during brownout and the fact the number of particles involved is large, the Eulerian-based dust transport model has been used to model and calculate the dust transport for the present case. With very low particle volume fraction, volume fraction of fluid is almost equal to unity. With the one-way coupling assumption, the fluid flow is not affected by the particle and the conservation equations (given in **CHAPTER 2**) for turbulent rotor flow are solved independent of particle flow.

3.3.6.1 Dust Transport Equation

The mass transport equation of a particle can be calculated by summing the mass change of the particle in the control volume to net efflux of mass from the control surface and the rate of dust generation in this volume.

$$\frac{\partial}{\partial t}(\alpha_p \rho_p) + \frac{\partial}{\partial x_i}(\alpha_p \rho_p u_{pi}) - \frac{\partial}{\partial x_3}(\alpha_p \rho_p w_t) = S_d \quad (3.38)$$

where u_p is particle velocity and S_d is dust source term. The third term, $\frac{\partial}{\partial x_3}(\alpha_p \rho_p w_t)$, takes care of the settling effect on a particle, due to gravity. The dust source term, S_d , is equal to dust generation near the ground due to dust emission. The magnitude of S_d is equal to vertical dust flux given by Eq. 3.25.

The above equation can be written in terms of particle dust density, using the relation $\rho_d = \alpha_p \rho_p$ as

$$\frac{\partial}{\partial t}(\rho_d) + \frac{\partial}{\partial x_i}(\rho_d u_{pi}) - \frac{\partial}{\partial x_3}(\rho_d w_t) = S_d \quad (3.39)$$

In turbulent flows, the particle velocity u_{pi} and dust density ρ_d can be divided into two components, i.e., average component and fluctuating component (similar to derivation of RANS equation) as

$$u_{pi} = \bar{u}_{pi} + u'_{pi} \quad (3.40)$$

$$\rho_d = \bar{\rho}_d + \rho'_d \quad (3.41)$$

Replacing this in the transport equation and time averaging the equation [25], the equation can be rewritten as

$$\frac{\partial}{\partial t}(\bar{\rho}_d) + \frac{\partial}{\partial x_i}(\bar{\rho}_d \bar{u}_{pi}) - \frac{\partial}{\partial x_3}(\bar{\rho}_d w_t) = S_d - \frac{\partial}{\partial x_i}(\overline{\rho'_d u'_{pi}}) \quad (3.42)$$

With reference to Fick's Law, the dispersion of the dust in turbulent flows can be modeled as

$$-\overline{\rho'_d u'_{pi}} = \Gamma_d \frac{\partial \bar{\rho}_d}{\partial x_i} \quad (3.43)$$

where Γ_d is dispersion or diffusion coefficient of dust in turbulent flows. The magnitude of Γ_d depends upon the flow characteristics and can be determined through experiments. One of the semi-empirical formulations used in geophysical research ([24]) is

$$\Gamma_d = \Gamma_F \left(1 + 4 \frac{\beta^2 w_t^2}{\sigma^2} \right) \quad (3.44)$$

where β is a dimensionless coefficient, Γ_F is the fluid diffusion coefficient, and σ is the standard deviation of turbulent velocity. In the current research, a relatively simple expression for Γ_d , mostly used in multiphase research [36], has been used.

$$\Gamma_d = \frac{\mu_t^p}{\sigma_t^p} \quad (3.45)$$

where μ_t^p is turbulent particle viscosity and σ_t^p is turbulent particle Schmidt number, which varies from 0.34–0.7. Turbulent particle viscosity μ_t^p is related to turbulent fluid eddy viscosity μ_t by

$$\mu_t^p = \frac{\mu_t}{1 + \frac{\tau_f}{\tau_f}} \quad (3.46)$$

where τ_f is fluid relaxation time given by $\tau_f = 0.2k/\epsilon$ [36].

3.3.6.2 Dust Particle Velocity

The relative velocity between the dust particle and fluid is defined as

$$\vec{u}_r = \vec{u}_p - \vec{u} \quad (3.47)$$

For dilute flows with low particle response time ($0.001 < \tau_v < 0.01s$), an algebraic slip formulation [38, 23] is used to calculate particle relative velocity. Assuming that local equilibrium has been reached between the particle and fluid, the relative velocity can be given by

$$\vec{u}_r = \frac{\tau_v}{f_{drag}} \frac{(\rho_p - \rho)}{\rho_p} \vec{a} \quad (3.48)$$

where \vec{a} is acceleration given by the mixture velocity (fluid velocity for low particle volume fraction) as

$$\vec{a} = \vec{f} - (\vec{u} \cdot \nabla) \vec{u} - \frac{\partial \vec{u}}{\partial t} \quad (3.49)$$

where \vec{f} is the acceleration due to body force. Since no electrostatic, magnetic effect, or other body forces have been considered and the effect of gravitational force has already been taken into account in the particle transport equation using the terminal velocity, w_t , $f = 0$ has been used to calculate particle relative velocity.

In turbulent flow, a diffusion term is added to the relative velocity to accommodate the effect of turbulent fluctuations.

$$\vec{u}_r = \frac{\tau_v}{f_{drag}} \frac{(\rho_p - \rho)}{\rho_p} \vec{a} + \vec{u}_r^t \quad (3.50)$$

where

$$\vec{u}_r^t = \mu_t^p \frac{1}{\rho_d} \nabla \rho_d \quad (3.51)$$

CHAPTER 4. NUMERICAL METHOD AND ALGORITHM

The transport equation for all the flow variables are solved using Finite Volume Method (FVM). Structured Cartesian grid has been used to discretize the domain.

4.1 General Convection-Diffusion Equation

The general Convection-Diffusion equation in three-dimensional Cartesian system can be written as:

$$\frac{\partial}{\partial t}(\rho\phi) + \frac{\partial}{\partial x}\left(\rho u\phi - \Gamma\frac{\partial\phi}{\partial x}\right) + \frac{\partial}{\partial y}\left(\rho v\phi - \Gamma\frac{\partial\phi}{\partial y}\right) + \frac{\partial}{\partial z}\left(\rho w\phi - \Gamma\frac{\partial\phi}{\partial z}\right) = S \quad (4.1)$$

where S is the external source term, and u , v and w denote the velocity components in the x , y and z directions, respectively.

The equation can be simplified as:

$$\frac{\partial(\rho\phi)}{\partial t} + \frac{\partial J_x}{\partial x} + \frac{\partial J_y}{\partial y} + \frac{\partial J_z}{\partial z} = S \quad (4.2)$$

where J_x , J_y and J_z represent the total (convection plus diffusion) fluxes defined by:

$$J_x \equiv \rho u\phi - \Gamma\frac{\partial\phi}{\partial x} \quad (4.3)$$

$$J_y \equiv \rho v\phi - \Gamma\frac{\partial\phi}{\partial y} \quad (4.4)$$

$$J_z \equiv \rho w\phi - \Gamma\frac{\partial\phi}{\partial z} \quad (4.5)$$

For a control volume given in Figure 4.1, the scalar variable ϕ is located at the control volume

center, P . The discretized form of this equation is obtained upon integration over the control volume and is given by the following equation.

$$\begin{aligned} [(\rho\phi) - (\rho\phi)^0] \frac{\Delta x \Delta y \Delta z}{\Delta t} + \alpha(J_{\phi-e} - J_{\phi-w} + J_{\phi-n} - J_{\phi-s} + J_{\phi-t} - J_{\phi-b}) + \\ (1 - \alpha)((J_{\phi-e}^0 - J_{\phi-w}^0 + J_{\phi-n}^0 - J_{\phi-s}^0 + J_{\phi-t}^0 - J_{\phi-b}^0) = \\ \alpha(S_C + S_P\phi) + (1 - \alpha)(S_C^0 + S_P^0\phi^0)\Delta x \Delta y \Delta z \end{aligned} \quad (4.6)$$

The subscripts e , w , etc. refer to the values computed at the control volume faces, as seen in Figure 4.1. The source term S has been linearized as $S = S_C + S_P\phi$. For the unsteady term, ρ and ϕ are assumed to prevail over the entire control volume. The 'old' values from the previous time step are denoted by subscript o .

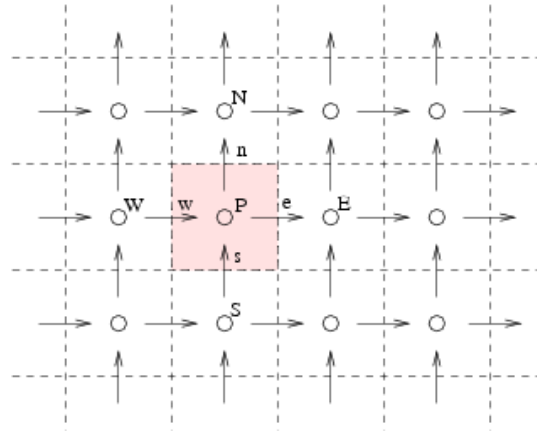


Figure 4.1 The control volume for scalar variable ϕ .

For incompressible flows, the continuity equation reduces to:

$$(F_e - F_w + F_n - F_s + F_t - F_b) = 0 \quad (4.7)$$

$$(F_e^0 - F_w^0 + F_n^0 - F_s^0 + F_t^0 - F_b^0) = 0 \quad (4.8)$$

Multiplying the continuity equation (Eq. 4.8) by $\alpha\phi$ for the current values and $(1 - \alpha)\phi^0$ for the 'old' values and subtracting them from the discretized Convection-Diffusion Equation, we

get:

$$\begin{aligned}
& (\phi - \phi^0)\rho^0 \frac{\Delta x \Delta y \Delta z}{\Delta t} + \alpha[(J_{\phi-e} - F_e\phi) - (J_{\phi-w} - F_w\phi) + \\
& \quad (J_{\phi-n} - F_n\phi) - (J_{\phi-s} - F_s\phi) + \\
& \quad (J_{\phi-t} - F_t\phi) - (J_{\phi-b} - F_b\phi)] + \\
& (1 - \alpha)[(J_{\phi-e}^0 - F_e^0\phi^0) - (J_{\phi-w}^0 - F_w^0\phi^0) + \\
& \quad (J_{\phi-n}^0 - F_n^0\phi^0) - (J_{\phi-s}^0 - F_s^0\phi^0) + \\
& \quad (J_{\phi-t}^0 - F_t^0\phi^0) - (J_{\phi-b}^0 - F_b^0\phi^0)] \\
& = \alpha(S_C + S_P\phi) + (1 - \alpha)(S_C^0 + S_P^0\phi^0)\Delta x \Delta y \Delta z \tag{4.9}
\end{aligned}$$

The terms, such as $(J_{\phi-e} - F_e\phi)$, can be rewritten as follows:

$$J_{\phi-e} - F_e\phi = a_E(\phi - \phi_E) \tag{4.10}$$

$$J_{\phi-w} - F_w\phi = a_W(\phi_W - \phi) \tag{4.11}$$

$$J_{\phi-n} - F_n\phi = a_N(\phi - \phi_N) \tag{4.12}$$

$$J_{\phi-s} - F_s\phi = a_S(\phi_S - \phi) \tag{4.13}$$

$$J_{\phi-t} - F_t\phi = a_T(\phi - \phi_T) \tag{4.14}$$

$$J_{\phi-b} - F_b\phi = a_B(\phi_B - \phi) \tag{4.15}$$

where the coefficients are obtained by the following equations:

$$a_E = D_e A(|P_e|) + [[-F_e, 0]] \tag{4.16}$$

$$a_W = D_w A(|P_w|) + [[F_w, 0]] \tag{4.17}$$

$$a_N = D_n A(|P_n|) + [[-F_n, 0]] \tag{4.18}$$

$$a_S = D_s A(|P_s|) + [[F_s, 0]] \tag{4.19}$$

$$a_T = D_t A(|P_t|) + [[-F_t, 0]] \tag{4.20}$$

$$a_B = D_b A(|P_b|) + [[F_b, 0]] \tag{4.21}$$

The subscripts E , W , etc. denote the neighboring control volume center values.

The diffusion terms are computed from:

$$D_e = \frac{\Gamma_e \Delta y \Delta z}{(\delta x)_e} \quad (4.22)$$

$$D_w = \frac{\Gamma_w \Delta y \Delta z}{(\delta x)_w} \quad (4.23)$$

$$D_n = \frac{\Gamma_n \Delta x \Delta z}{(\delta y)_n} \quad (4.24)$$

$$D_s = \frac{\Gamma_s \Delta x \Delta z}{(\delta y)_s} \quad (4.25)$$

$$D_t = \frac{\Gamma_t \Delta y \Delta x}{(\delta z)_t} \quad (4.26)$$

$$D_b = \frac{\Gamma_b \Delta y \Delta x}{(\delta z)_b} \quad (4.27)$$

and the Peclet numbers from:

$$P_e = \frac{F_e}{D_e} \quad (4.28)$$

$$P_w = \frac{F_w}{D_w} \quad (4.29)$$

$$P_n = \frac{F_n}{D_n} \quad (4.30)$$

$$P_s = \frac{F_s}{D_s} \quad (4.31)$$

$$P_t = \frac{F_t}{D_t} \quad (4.32)$$

$$P_b = \frac{F_b}{D_b} \quad (4.33)$$

For the Power Law scheme, the function $A(|P|)$ is computed from:

$$A(|P|) = \llbracket 0, (1 - 0.1|P|)^5 \rrbracket \quad (4.34)$$

and the equation becomes

$$\begin{aligned}
& \phi \frac{\rho \Delta x \Delta y \Delta z}{\Delta t} + \alpha (a_E + a_W + a_N + a_S + a_T + a_B - S_P \Delta x \Delta y \Delta z) \phi \\
= & \alpha (a_E \phi_E + a_W \phi_W + a_N \phi_N + a_S \phi_S + a_T \phi_T + a_B \phi_B) + \\
& (1 - \alpha) [a_E^0 \phi_E^0 + a_W^0 \phi_W^0 + a_N^0 \phi_N^0 + a_S^0 \phi_S^0 + a_T^0 \phi_T^0 + a_B^0 \phi_B^0] - \\
& (1 - \alpha) [a_E^0 + a_W^0 + a_N^0 + a_S^0 + a_T^0 + a_B^0 - S_P^0 \Delta x \Delta y \Delta z] \phi^0 + \\
& \phi^0 \frac{\rho \Delta x \Delta y \Delta z}{\Delta t} + \Delta x \Delta y \Delta z (\alpha S_C + (1 - \alpha) S_C^0)
\end{aligned} \tag{4.35}$$

This equation can be rewritten as:

$$\rho \frac{\Delta x \Delta y \Delta z}{\Delta t} \phi + \alpha a_P \phi = \alpha (a_E \phi_E + a_W \phi_W + a_N \phi_N + a_S \phi_S + a_T \phi_T + a_B \phi_B) + b_{total} \tag{4.36}$$

where:

$$a_P = a_E + a_W + a_N + a_S + a_T + a_B - S_P \Delta x \Delta y \Delta z \tag{4.37}$$

$$b_{total} = \alpha b + b_o \tag{4.38}$$

$$b = S_C \Delta x \Delta y \Delta z \tag{4.39}$$

$$\begin{aligned}
b_o = & (1 - \alpha) [a_E^0 \phi_E^0 + a_W^0 \phi_W^0 + a_N^0 \phi_N^0 + a_S^0 \phi_S^0 + a_T^0 \phi_T^0 + a_B^0 \phi_B^0] \\
& - (1 - \alpha) a_P^0 \phi^0 + \rho \frac{\Delta x \Delta y \Delta z}{\Delta t} \phi^0 + (1 - \alpha) b^0
\end{aligned} \tag{4.40}$$

4.1.1 Scalar variables

The scalar variables ϕ , diffusion coefficient Γ , and source term (S) for each scalar transport equation is given in Table 4.1.

It should be noted that for dust transport equation particle density ρ_p and particle velocities u_{pi} is used in place of fluid density ρ and fluid velocities u_i respectively.

Source term linearization is completed in the following manner.

Table 4.1 Coefficient and source term for scalar transport equations

	ϕ	Γ	S
Spalart-Allmaras	$\tilde{\nu}$	$\frac{\rho}{\sigma}(\nu + \tilde{\nu})$	$\rho C_{b1}[1 - f_{t2}]\tilde{S}\tilde{\nu} + \frac{\rho}{\sigma}C_{b2} \nabla\nu ^2$ $+ \rho \left[C_{w1}f_w - \frac{C_{b1}}{\kappa^2}f_{t2} \right] \left(\frac{\tilde{\nu}}{d} \right)^2 + \rho f_{t1}\Delta U^2$
Standard $k - \epsilon$	k	$\left(\mu + \frac{\mu_t}{\sigma_k} \right)$	$P_k - \rho\epsilon$
	ϵ	$\left(\mu + \frac{\mu_t}{\sigma_\epsilon} \right)$	$C_{1\epsilon}\frac{\epsilon}{k}P_k - C_{2\epsilon}\rho\frac{\epsilon^2}{k}$
Realizable $k - \epsilon$	k	$\left(\mu + \frac{\mu_t}{\sigma_k} \right)$	$P_k - \rho\epsilon$
	ϵ	$\left(\mu + \frac{\mu_t}{\sigma_\epsilon} \right)$	$\rho C_1 S\epsilon - \rho C_2 \frac{\epsilon^2}{k + \sqrt{\nu\epsilon}}$
Dust Transport	α_p	$\frac{\mu_p^t}{\sigma_p^t}$	F

Spalart-Allmaras

For $\tilde{\nu}$ equation

$$\begin{aligned}
 S_C &= \frac{\rho}{\sigma}C_{b2}|\nabla\nu|^2 + \rho f_{t1}\Delta U^2 \\
 &\quad + \tilde{\nu} \max \left[0, \rho C_{b1}[1 - f_{t2}]\tilde{S} + \rho \left[C_{w1}f_w - \frac{C_{b1}}{\kappa^2}f_{t2} \right] \left(\frac{\tilde{\nu}}{d^2} \right) \right] \\
 S_P &= \min \left[0, \rho C_{b1}[1 - f_{t2}]\tilde{S} + \rho \left[C_{w1}f_w - \frac{C_{b1}}{\kappa^2}f_{t2} \right] \left(\frac{\tilde{\nu}}{d^2} \right) \right]
 \end{aligned} \tag{4.41}$$

Standard $k - \epsilon$ For k equation

$$\begin{aligned} S_C &= P_k \\ S_P &= -\rho \frac{c_{\mu} \rho k}{\mu_t} \end{aligned} \quad (4.42)$$

For ϵ equation

$$\begin{aligned} S_C &= C_{1\epsilon} \frac{\epsilon}{k} P_k \\ S_P &= -C_{2\epsilon} \rho \frac{\epsilon}{k} \end{aligned} \quad (4.43)$$

Realizable $k - \epsilon$ For k equation

$$\begin{aligned} S_C &= P_k \\ S_P &= -\rho \frac{c_{\mu} \rho k}{\mu_t} \end{aligned} \quad (4.44)$$

For ϵ equation

$$\begin{aligned} S_C &= \rho C_1 S \epsilon \\ S_P &= -\rho C_2 \frac{\epsilon}{k + \sqrt{\nu \epsilon}} \end{aligned} \quad (4.45)$$

Dust TransportFor α_P equation

$$\begin{aligned} S_C &= F \\ S_P &= 0 \end{aligned} \quad (4.46)$$

4.2 Momentum Equations

The discretized momentum equations for the velocities can be derived similarly from the general Convection-Diffusion Equation with the ϕ term replaced by the velocity components u , v and w . In this research, a staggered mesh is used. This means the velocity components u , v and w are positioned at different control volume faces as seen in Figure 4.2. Therefore, the equations must be adjusted accordingly.

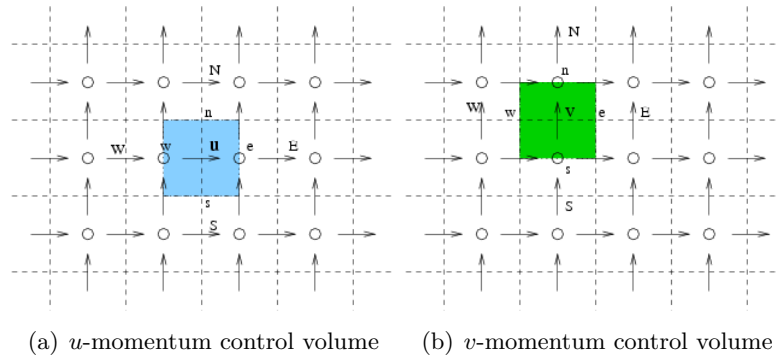


Figure 4.2 Control volumes of u and v momentum

If the source term (b_{total}) of u , v , and w momentum equations in the discretized momentum are denoted as b_u^{total} , b_v^{total} , and b_w^{total} , then the discretized form of the momentum equation for u becomes:

$$\rho \frac{\Delta x \Delta y \Delta z}{\Delta t} u_P + \alpha a_P^u u_P = \alpha (a_E u_E + a_W u_W + a_N u_N + a_S u_S + a_T u_T + a_B u_B) + b_u^{total} \quad (4.47)$$

where

$$a_P^u = a_E + a_W + a_N + a_S + a_T + a_B - S_P^u \Delta x \Delta y \Delta z \quad (4.48)$$

$$b_u^{total} = \alpha b_u + b_o^u + (p_W - p_E) \Delta y \Delta z \quad (4.49)$$

$$b_u = S_C^u \Delta x \Delta y \Delta z \quad (4.50)$$

$$b_o^u = (1 - \alpha)[a_E^0 u_E^0 + a_W^0 u_W^0 + a_N^0 u_N^0 + a_S^0 u_S^0 + a_T^0 u_T^0 + a_B^0 u_B^0] \\ - (1 - \alpha)(a_P^u u_P)^0 + \rho \frac{\Delta x \Delta y \Delta z}{\Delta t} u^0 + (1 - \alpha) b_u^0 \quad (4.51)$$

Similar expressions can be written for v - and w - momentum equations as:

$$\rho \frac{\Delta x \Delta y \Delta z}{\Delta t} v_P + \alpha a_P^v v_P = \alpha (a_E v_E + a_W v_W + a_N v_N + a_S v_S + a_T v_T + a_B v_B) + b_v^{total} \quad (4.52)$$

where

$$a_P^v = a_E + a_W + a_N + a_S + a_T + a_B - S_P^v \Delta x \Delta y \Delta z \quad (4.53)$$

$$b_v^{total} = \alpha b_v + b_o^v + (p_S - p_N) \Delta x \Delta z \quad (4.54)$$

$$b_v = S_C^v \Delta x \Delta y \Delta z \quad (4.55)$$

$$b_o^v = (1 - \alpha)[a_E^0 v_E^0 + a_W^0 v_W^0 + a_N^0 v_N^0 + a_S^0 v_S^0 + a_T^0 v_T^0 + a_B^0 v_B^0] \\ - (1 - \alpha)(a_P^v v_P)^0 + \rho \frac{\Delta x \Delta y \Delta z}{\Delta t} v^0 + (1 - \alpha) b_v^0 \quad (4.56)$$

and

$$\rho \frac{\Delta x \Delta y \Delta z}{\Delta t} w_P + \alpha a_P^w w_P = \alpha (a_E w_E + a_W w_W + a_N w_N + a_S w_S + a_T w_T + a_B w_B) + b_w^{total} \quad (4.57)$$

where

$$a_P^w = a_E + a_W + a_N + a_S + a_T + a_B - S_P^w \Delta x \Delta y \Delta z \quad (4.58)$$

$$b_w^{total} = \alpha b_w + b_o^w + (p_B - p_T) \Delta x \Delta y \quad (4.59)$$

$$b_w = S_C^w \Delta x \Delta y \Delta z \quad (4.60)$$

$$b_o^w = (1 - \alpha)[a_E^0 w_E^0 + a_W^0 w_W^0 + a_N^0 w_N^0 + a_S^0 w_S^0 + a_T^0 w_T^0 + a_B^0 w_B^0] \\ - (1 - \alpha)(a_P^w w_P)^0 + \rho \frac{\Delta x \Delta y \Delta z}{\Delta t} w^0 + (1 - \alpha) b_w^0 \quad (4.61)$$

4.2.1 Pressure correction equation

The discretized momentum can be solved similar to discretized scalar equations, if the pressure field is given. Since the correct pressure field is not known initially, a guessed pressure field is used to solve for the velocity field. Since the pressure field is not correct, the calculated velocity field may not satisfy the continuity equation. Thus, a correction (pressure) is applied to correct the velocity field such that the mass conservation is satisfied in each computational cell. The pressure correction is calculated by solving the pressure correction equation.

For the pressure control volume P_p , the discretized momentum equation of east face u velocity can be written similar to Eq. 4.51 as

$$a_e u_e = \Sigma a_{nb} u_{nb} + b + (p_P - p_E) A_e \quad (4.62)$$

where subscript nb denotes neighboring point and b is the source term without the pressure term. If the guessed pressure field is denoted by p^* , then the imperfect velocity is denoted as u^* , v^* , and w^* . These imperfect velocity fields are solution of the following discretized equation

$$a_e u_e^* = \Sigma a_{nb} u_{nb}^* + b + (p_P^* - p_E^*) A_e \quad (4.63)$$

$$a_n v_n^* = \Sigma a_{nb} v_{nb}^* + b + (p_P^* - p_N^*) A_n \quad (4.64)$$

$$a_t w_e^* = \Sigma a_{nb} w_{nb}^* + b + (p_P^* - p_T^*) A_t \quad (4.65)$$

Solving the velocities using the discretized momentum equation with guessed pressure field p^* in general will not satisfy the continuity equation. If p' is the pressure correction required to get the correct pressure field then

$$p = p^* + p' \quad (4.66)$$

The velocity is corrected as

$$\begin{aligned} u &= u^* + u' \\ v &= v^* + v' \\ w &= w^* + w' \end{aligned} \quad (4.67)$$

Subtracting Eq. 4.65 from Eq. 4.62, and using Eq. 4.67, we have

$$a_e u'_e = \Sigma a_{nb} u'_{nb} + (p'_P - p'_E) A_e \quad (4.68)$$

by dropping the $\Sigma a_{nb} u'_{nb}$ term

$$a_e u'_e = (p'_P - p'_E) A_e \quad (4.69)$$

$$u'_e = d_e (p'_P - p'_E) \quad (4.70)$$

where

$$d_e \equiv \frac{A_e}{a_e}. \quad (4.71)$$

The Eq. 4.70 is called the velocity-correction formula. The corrected velocities are given as

$$\begin{aligned} u_e &= u_e^* + d_e (p'_P - p'_E) \\ v_n &= v_n^* + d_n (p'_P - p'_N) \\ w_t &= w_t^* + d_t (p'_P - p'_T) \end{aligned} \quad (4.72)$$

The discretized equation of p' is obtained from continuity equation. The continuity equation

is

$$\frac{\partial \rho}{\partial t} + \frac{\partial(\rho u)}{\partial x} + \frac{\partial(\rho v)}{\partial y} + \frac{\partial(\rho w)}{\partial z} = 0 \quad (4.73)$$

Integrating the equation over the pressure control volume yields

$$\begin{aligned} \frac{(\rho_P - \rho_P^0)\Delta x\Delta y\Delta z}{\Delta t} + [(\rho u)_e - (\rho u)_w] \Delta y\Delta z + [(\rho v)_n - (\rho v)_s] \Delta z\Delta x \\ + [(\rho w)_t - (\rho w)_b] \Delta x\Delta y = 0 \end{aligned} \quad (4.74)$$

Substituting the velocity component by the velocity correction expression (Eq. 4.72) gives

$$a_P p'_P = a_E p'_E + a_W p'_W + a_N p'_N + a_S p'_S + a_T p'_T + a_B p'_B + b \quad (4.75)$$

where

$$\begin{aligned} a_E &= \rho_e d_e \Delta y \Delta z \\ a_W &= \rho_w d_w \Delta y \Delta z \\ a_N &= \rho_n d_n \Delta z \Delta x \\ a_S &= \rho_s d_s \Delta z \Delta x \\ a_T &= \rho_t d_t \Delta x \Delta y \\ a_B &= \rho_b d_b \Delta x \Delta y \\ a_P &= a_E + a_W + a_N + a_S + a_T + a_B \\ b &= \frac{(\rho_P - \rho_P^0)\Delta x\Delta y\Delta z}{\Delta t} + [(\rho u^*)_e - (\rho u^*)_w] \Delta y \Delta z \\ &\quad + [(\rho v^*)_n - (\rho v^*)_s] \Delta z \Delta x + [(\rho w^*)_t - (\rho w^*)_b] \Delta x \Delta y \end{aligned} \quad (4.76)$$

4.2.2 The pressure equation

Since, in the velocity correction equations, the neighbor-point velocity correction is not considered, the pressure correction has the entire responsibility to correct the velocity field. This leads to severe pressure-correction fields, which is efficient in correcting the velocity field,

but pressure field may not be calculated properly. To overcome this problem, the pressure is calculated through pressure equation and pressure-correction is only used for correcting the velocities.

The momentum equation can be re-written as

$$u_e = \frac{\sum a_{nb} u_{nb} + b}{a_e} + d_e(p_P - p_E) \quad (4.77)$$

Defining pseudo-velocity \hat{u}_e by

$$\hat{u}_e = \frac{\sum a_{nb} u_{nb} + b}{a_e} \quad (4.78)$$

The momentum equation can be written as

$$u_e = \hat{u}_e + d_e(p_P - p_E) \quad (4.79)$$

Similarly other velocities can be written as

$$v_n = \hat{v}_n + d_n(p_P - p_N) \quad (4.80)$$

$$w_t = \hat{w}_t + d_t(p_P - p_T) \quad (4.81)$$

Replacing the above definition of velocity in discretized continuity equation (Eq. 4.74) we have

$$a_P p_P = a_E p_E + a_W p_W + a_N p_N + a_S p_S + a_T p_T + a_B p_B + b \quad (4.82)$$

where $a_E, a_N, a_S, a_T,$ and a_B are similar to pressure correction coefficient as given in Eqn. 4.76 and b is given by

$$\begin{aligned} b = & \frac{(\rho_P - \rho_P^0) \Delta x \Delta y \Delta z}{\Delta t} + [(\rho \hat{u})_e - (\rho \hat{u})_w] \Delta y \Delta z \\ & + [(\rho \hat{v})_n - (\rho \hat{v})_s] \Delta z \Delta x + [(\rho \hat{w})_t - (\rho \hat{w})_b] \Delta x \Delta y \end{aligned} \quad (4.83)$$

4.2.3 The SIMPLER algorithm

The SIMPLER algorithm [11] consist of solving the pressure equation to obtain the pressure field and uses the pressure-correction field only to correct the velocity field. The algorithm follows :

1. Start with a given initial flow field.
2. Calculate the unsteady portion of the center coefficients.
3. Calculate the unsteady portion of the source terms.
4. Calculate the coefficients of the momentum equations and the pseudo-velocities.
5. Using the pseudo-velocities, calculate the source term for the pressure equation.
6. Calculate the coefficients for the pressure equation and solve the pressure equation to obtain the pressure field.
7. Using the calculated pressure field, solve the momentum equations to obtain the velocity field (u , v , and w).
8. Calculate the source terms of the pressure correction equation and solve for the pressure corrections.
9. Correct the velocities using the velocity correction equations.
10. Return to Step 4 and repeat until convergence.
11. Go to Step 2 and start with a new time level.

4.3 Boundary conditions

To solve the discretized equations, boundary conditions are needed for each transport equation. Mainly three boundary conditions, inlet, outlet, and wall boundary conditions, have been used in almost all the simulations carried out in this current research.

4.3.1 Inlet boundary conditions

Momentum Equation: Inlet velocity is provided.

Spalart-Allmaras Model: Turbulent viscosity ratio, ν_t/ν , is provide at the inlet. In general, the turbulent viscosity ratio varies from 3.0 to 10.0.

$k - \epsilon$ Model: Turbulent intensity (I) and turbulent length scale (l) are provided, based on the turbulent kinetic energy and turbulent dissipation calculated.

$$k_{inlet} = \frac{3}{2}(U I)^2 \quad (4.84)$$

$$\epsilon_{inlet} = C_\mu^{\frac{3}{4}} \frac{k^{\frac{3}{2}}}{l} \quad (4.85)$$

Turbulent intensity of 1 to 10% has been used. Turbulent length scale of the order rotor radius ($l \approx R$), has been used.

Dust Transport Model: Dust concentration at inlet is zero $\alpha_p = 0$.

4.3.2 Outlet boundary conditions

Momentum Equation: Outlet velocity is calculated, based on mass conservation, such that

$$\dot{m}_{out} = \dot{m}_{in} \quad (4.86)$$

where \dot{m}_{out} is total mass outflow from all outlet boundaries and \dot{m}_{in} is the inflow from inlet boundaries.

Spalart-Allmaras Model: Neumann boundary condition is used such that

$$\frac{\partial \tilde{\nu}}{\partial n} = 0 \quad (4.87)$$

$k - \epsilon$ Model: Neumann boundary condition is used such that

$$\begin{aligned}\frac{\partial k}{\partial n} &= 0 \\ \frac{\partial \epsilon}{\partial n} &= 0\end{aligned}\quad (4.88)$$

Dust Transport Model: Neumann boundary condition is used such that

$$\frac{\partial \alpha_p}{\partial n} = 0 \quad (4.89)$$

4.3.3 Wall boundary condition

Momentum Equation: No-slip boundary condition is used such that velocity on the face of the wall is zero. In the case of $k - \epsilon$ model, μ_e is calculated on the wall faces using the function approach (discussed in APPENDIX-1). For the cells which lie inside the body geometry, the diffusion is set to infinite.

Spalart-Allmaras Model:

$$\tilde{\nu} = 0 \quad (4.90)$$

$k - \epsilon$ Model: $k - \epsilon$ model cannot be integrated to the wall. To bridge this, wall function (discussed in APPENDIX-1) is used to provide the boundary condition.

Dust Transport Model: Dust concentration at the wall has been taken to be zero.

$$\alpha_p = 0 \quad (4.91)$$

4.3.4 Computational process

During the computational process, RANS equation is solved first at each time step. While solving the RANS, the rotor source model is invoked at each iteration to add the rotor source terms. From the converged flowfield, the turbulent properties are solved by solving turbulence models. After the calculation of flow field variables, the dust transport model is started, which is solved for dust concentration. The entire algorithm is given in the flow chart shown in Figure

4.3.

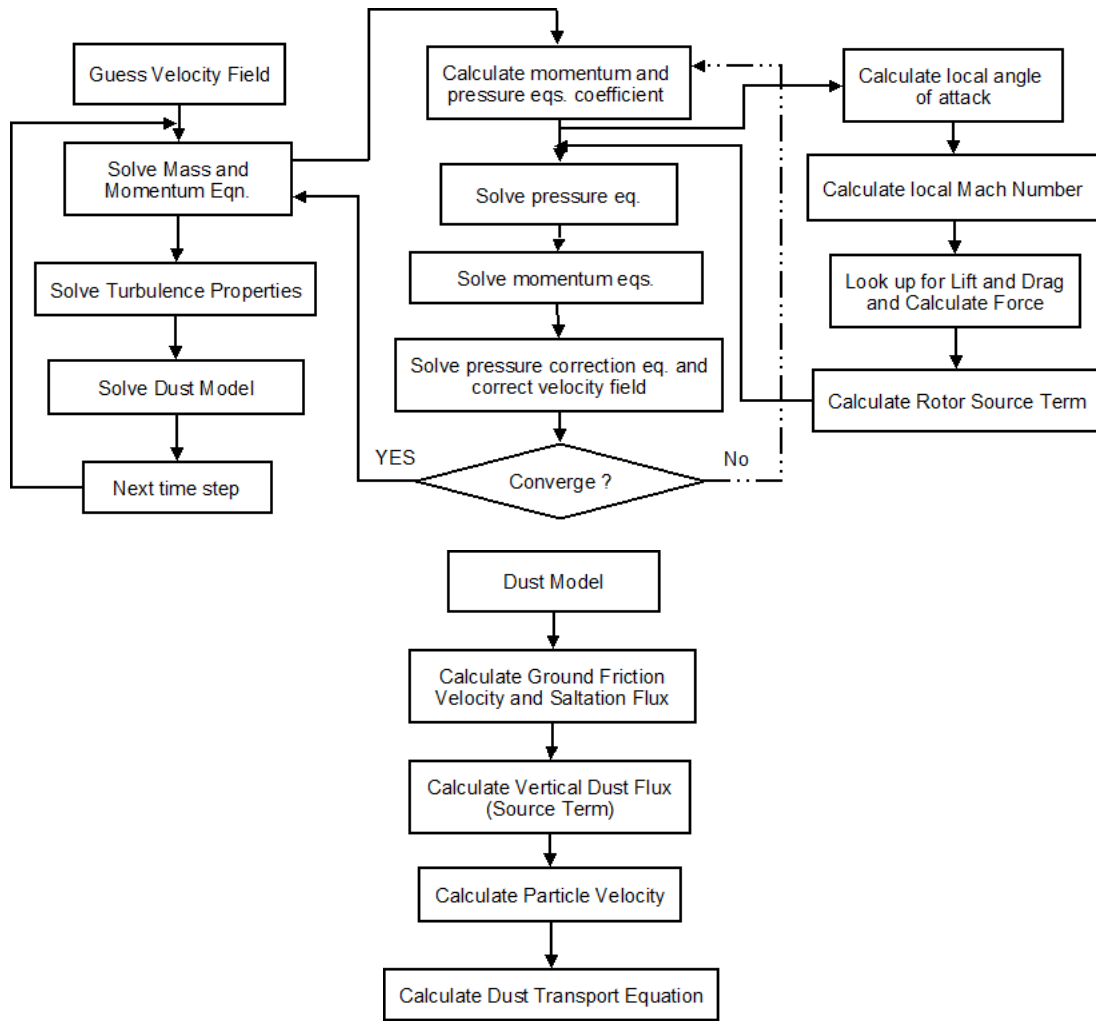


Figure 4.3 Flowchart of Rotorcraft Brownout Model

CHAPTER 5. RESULTS

A three-dimensional Cartesian grid-based incompressible laminar solver has been developed from an existing two-dimensional solver. This three-dimensional solver has been used as a testbed for implementing, validating, and testing various turbulence models and the brownout dust transport model. For solving the rotor flow, the existing rotor source model has been integrated with the turbulent solver.

5.1 Validation

5.1.1 3D incompressible solver

To validate the three-dimensional laminar incompressible solver, a standard test case of lid driven cavity has been used. In this test case, the cavity is cube shaped with $1m$ length(l) and the lid moves at constant speed (U_{lid}) of $1m/s$. The test has been completed at two Reynolds numbers of 100 and 400, where the Reynolds number is defined as

$$Re = \frac{\rho U_{lid} l}{\mu} \quad (5.1)$$

The wall of the cavity has been modeled as viscous no slip boundary condition. The domain is discretized into a $42 \times 42 \times 42$ non-uniform grid.

Results of center plane velocity distributions are compared with Flux Corrector Method (FCM) used by Wirogo [39]. At $Re = 100$, horizontal velocity, u , and vertical velocity, v , at center plane are plotted in Figure 5.1. For $Re = 400$, horizontal velocity (u) and vertical velocity (v) at center plane are plotted in Figure 5.2. The contour plot of velocity magnitude at center plane for both Reynolds numbers is plotted in Figure 5.3

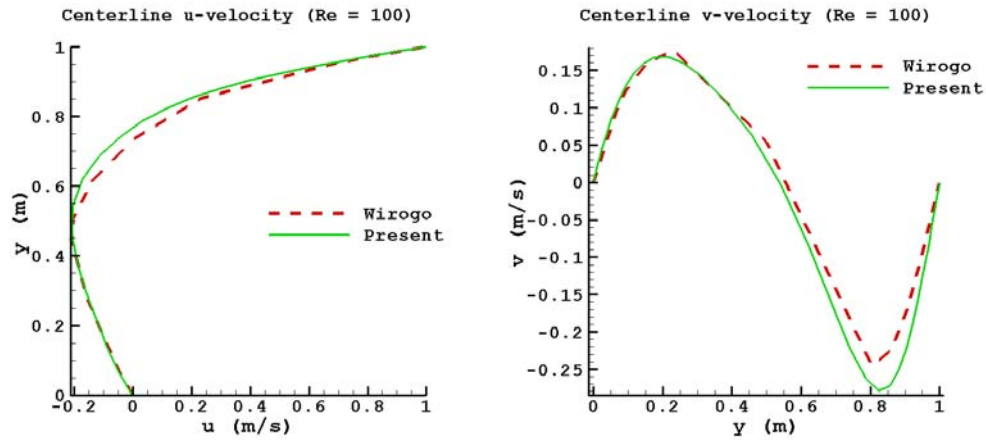


Figure 5.1 u and v velocity at center plane in driven cavity at $Re = 100$

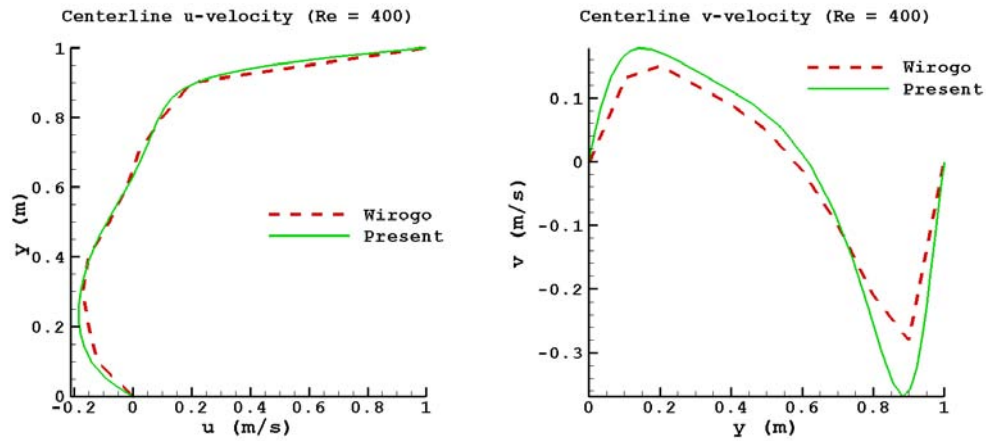


Figure 5.2 u and v velocity at center plane in driven cavity at $Re = 400$

At both the Reynolds numbers, u velocity profiles match well with FCM. In the v velocity profile, the present scheme (Power-Law) predicts a higher maximum velocity, due to the high numerical diffusivity caused by the first order scheme.

5.1.2 Turbulence models

Four turbulence models have been integrated with the 2D and 3D incompressible solvers. The first test is achieved by simulating turbulent flow over the 2D flat plate. Skin friction coefficient ($C_f = 2\tau_w/\rho V_{inf}^2$) is plotted against Reynolds number ($Re = \rho V_{inf} x/\mu$) for all turbulence models in Figure 5.4. Results are compared with empirical formulation for skin

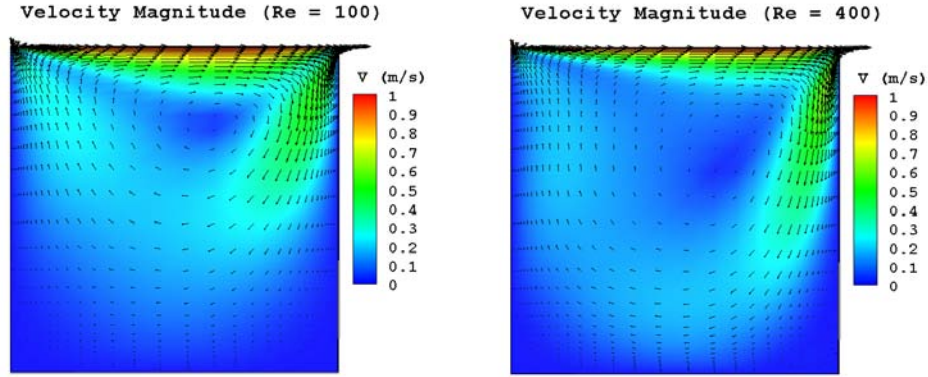


Figure 5.3 Velocity magnitude contour plot at center plane of driven cavity at Re = 100 and 400

friction over the square plate for turbulent flows by Schlichting [40]

$$C_f = \frac{0.059}{Re_x^{(1/5)}} \quad (5.2)$$

The Baldwin-Lomax and Spalart-Allmaras models give good comparisons for most of the Reynolds number range. Both $k - \epsilon$ models over-predict skin friction at a relatively low Reynolds number ($< 3.0 \times 10^5$). This is because both $k - \epsilon$ models used are for high Reynolds number fully turbulent flows. Among both $k - \epsilon$ models, Realizable $k - \epsilon$ gives a better results.

Another case of 3D circular impinging jet is used for comparing the turbulence models. Circular impinging jet closely resembles rotorcraft in ground effect, which have various features like recirculation, stagnation zone, and wall jet.

The simulation set-up is shown in Figure 5.5. Set-up and flow condition are similar to experiments carried out by Cooper et al. [41]. In this present case, the H/D ratio is taken to be 2 and Reynolds number is 70,000, where Reynolds number is based on impinging bulk velocity and diameter of nozzle.

Velocity profiles at three different radial locations ($r/R = 1.0, 2.0$ and 3.0) are plotted in Figure 5.6 for all turbulent models and have been compared with the experimental results. Velocity magnitude contour plots for all the cases are shown in Figure 5.7.

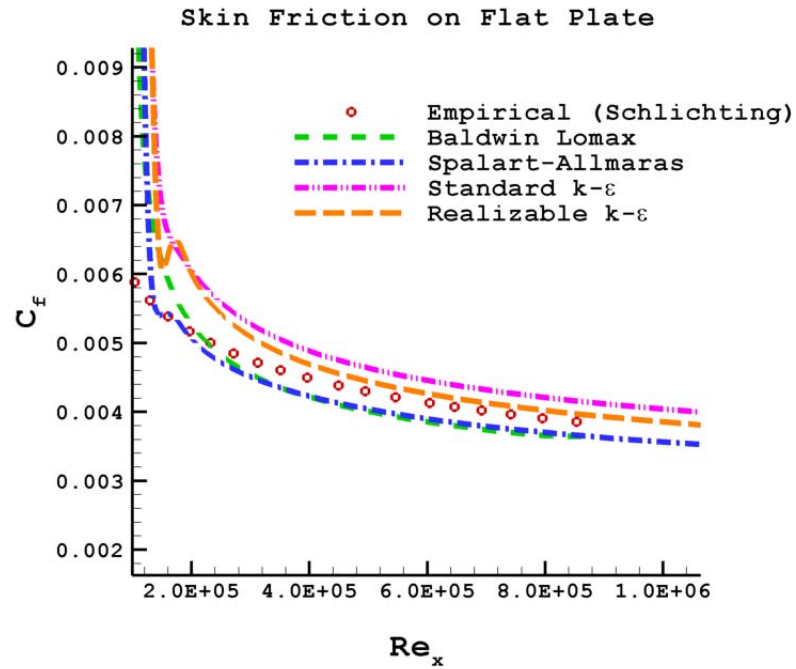


Figure 5.4 Skin friction coefficient with Reynolds number on flat plate

It can be seen that at $r/R = 1.0$, Laminar and the Baldwin-Lomax model give the best result. Further downstream in the wall jet region, both laminar and Baldwin-Lomax model over-predict the maximum wall jet velocity and at higher heights under-predict the profile velocity. In the wall jet region, one-equation model and two-equation model give better comparisons.

Turbulent shear stress $\overline{u'w'}$ is also plotted at various radial locations in Figure 5.8. It can be seen that none of the linear eddy viscosity-based model predicts the turbulent shear stress accurately. The reason, as given by Craft et al. [42], is due to anisotropic behavior of turbulent fluctuating velocity in the impinging jet case, where turbulent kinetic energy is dominated by normal straining and fluctuating velocity normal to the wall is larger than that parallel to the wall at the impingement zone. Nevertheless, after comparing all the results, the two-equation model seems to give the best qualitative results.

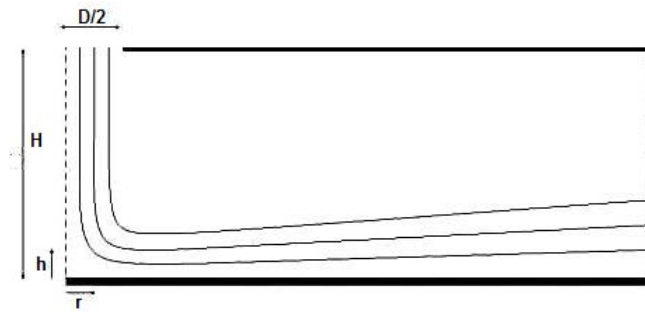


Figure 5.5 Impinging jet simulation set up

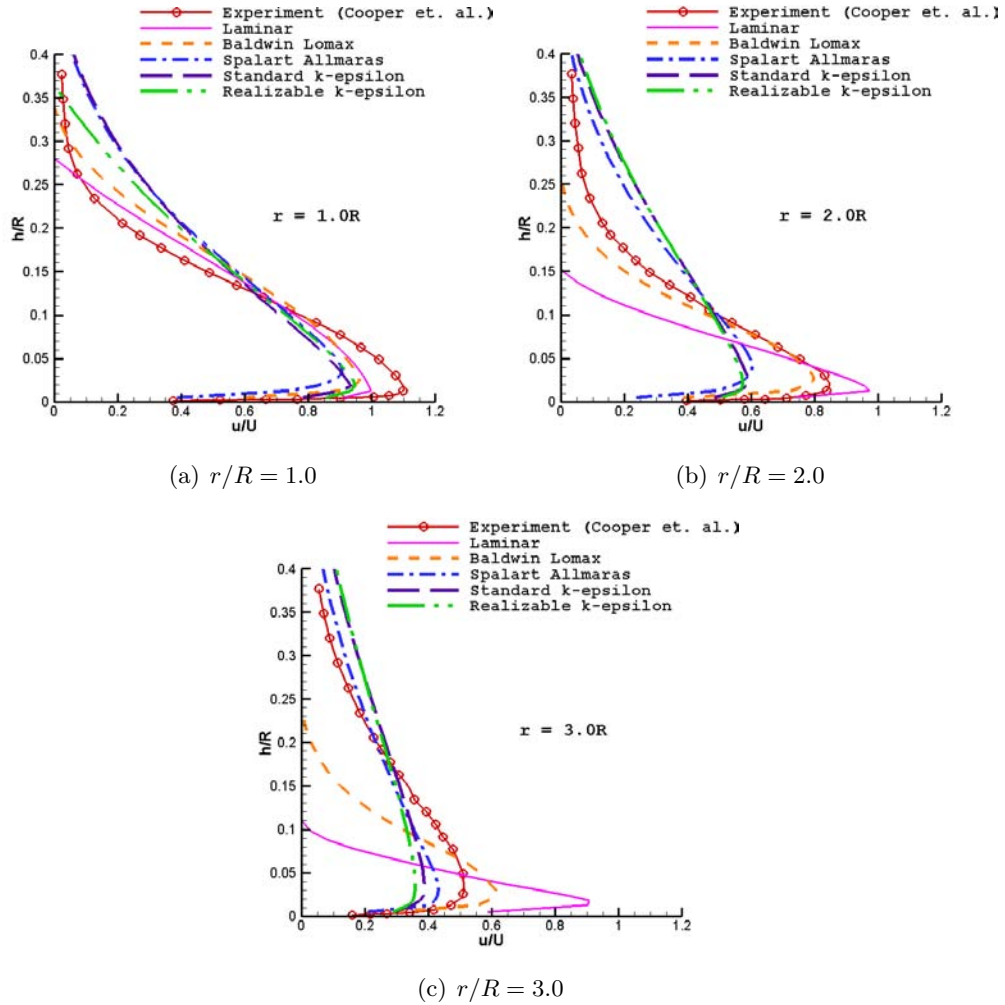


Figure 5.6 Impinging jet velocity profile

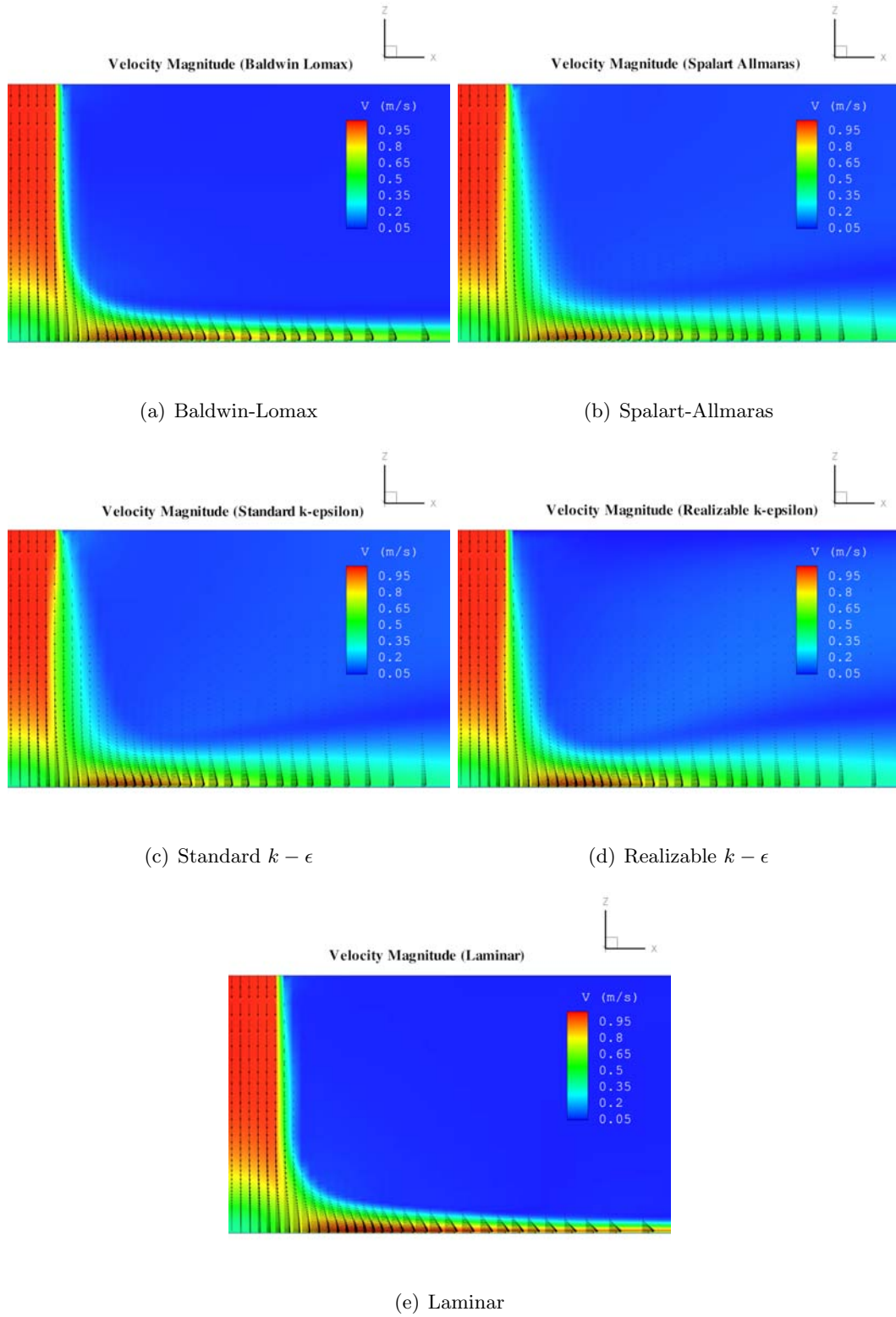


Figure 5.7 Velocity magnitude contour plot (impinging jet)

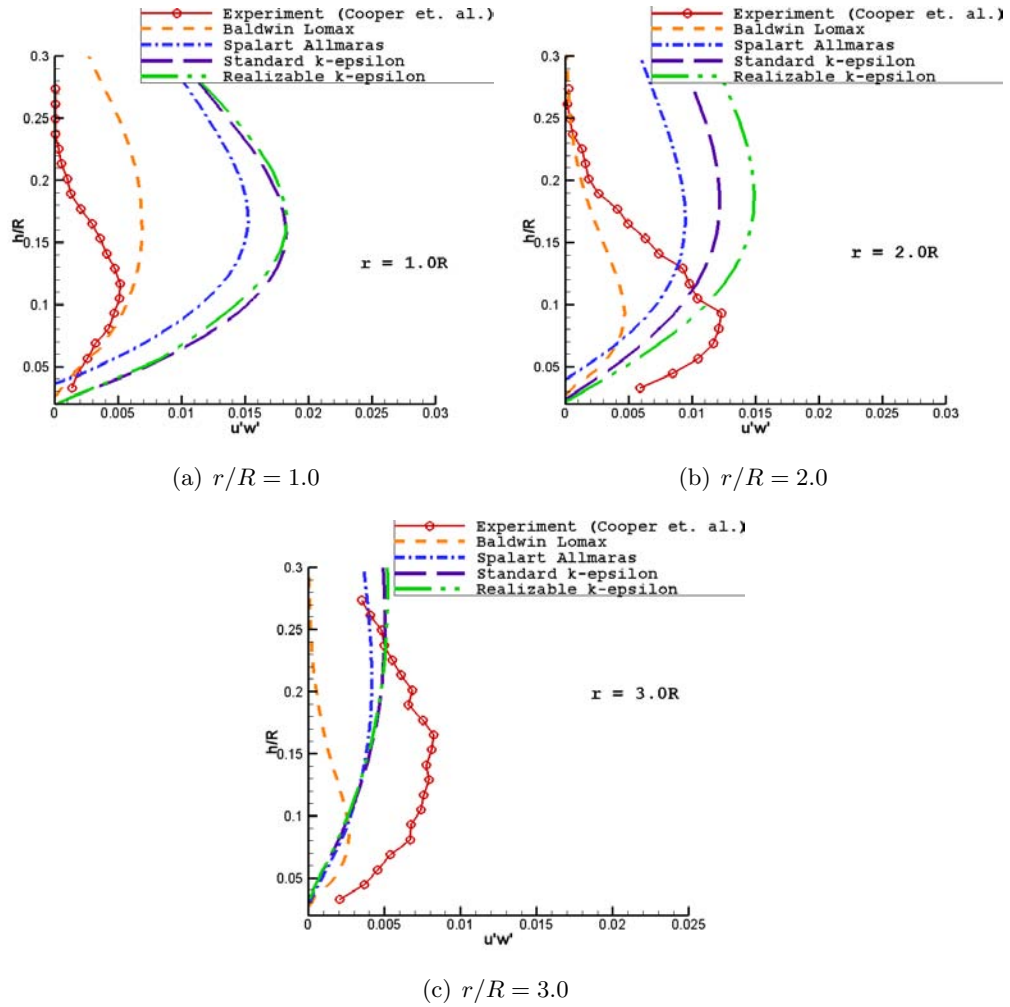


Figure 5.8 Reynolds Shear Stress $\overline{u'w'}$ in impinging jet

5.1.3 Rotor model validation

To validate rotor source modeling, simulation has been accomplished on a rotor similar to experiments completed by Rabbott [43]. A two-bladed rotor has been used with 15ft diameter. Simulations were carried out at various collective pitches (Θ). For the current simulation, NACA0012 airfoil was used. Chord length was 0.153 times the radius and there was zero twist along the blade. The variation of aerodynamic blade load with radial locations at various collective pitches is plotted in Figure 5.9.

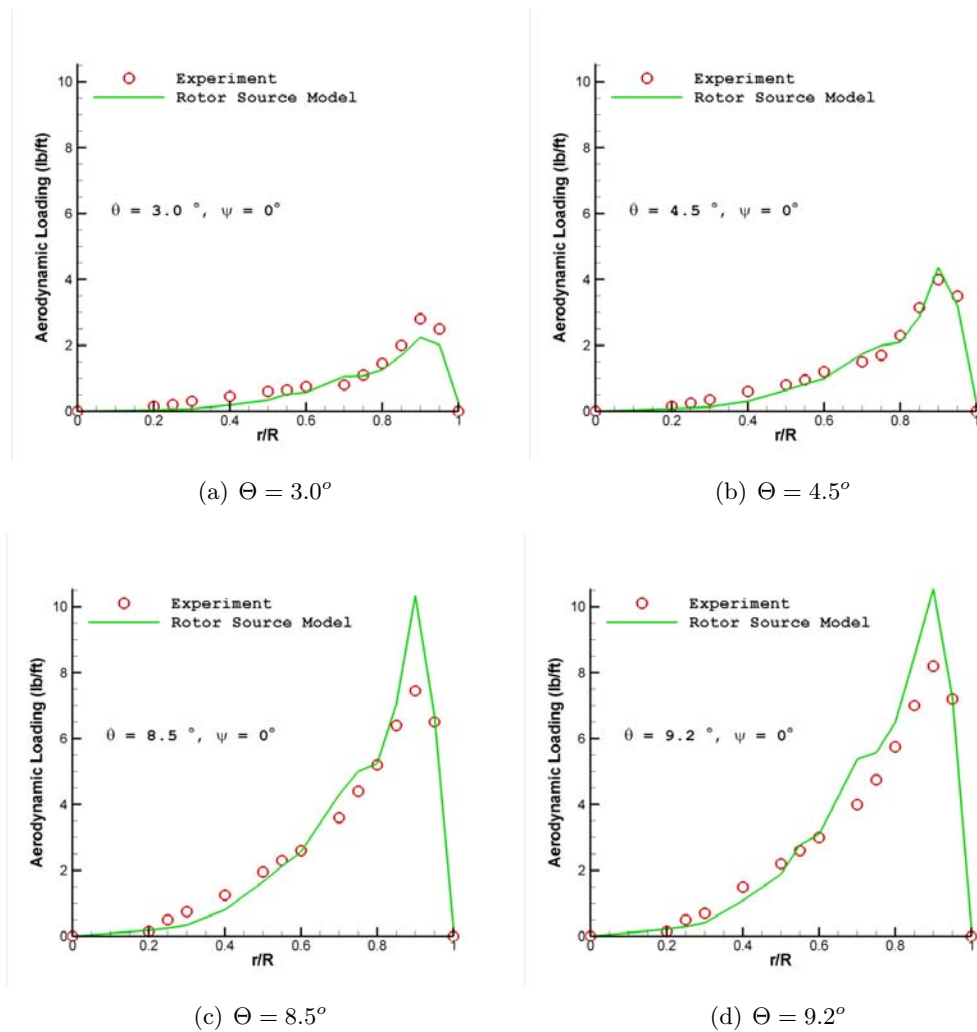


Figure 5.9 Aerodynamic blade load comparisons with Rabbott's experiment at various Θ

The rotor source model with tip correction, is able to perfectly capture the trend of the

aerodynamic load along the blade radius.

5.1.4 Brownout model validation

It is very difficult to validate the brownout model. There have not been many quantitative experimental data on brownout. The present model has been qualitatively validated with wind tunnel experiments conducted by Nathan and Green [44] at University of Glasgow. In their experiment, a small model rotor was used and was placed at one radius above the ground. The wind tunnel speed was set so the thrust-normalized advanced ratio μ^* is equal to 0.65. Thrust-normalized advanced ratio was given by

$$\mu^* = \frac{\mu}{\sqrt{(C_T/2)}} \quad (5.3)$$

where μ is rotor advance ratio and C_T is coefficient of thrust.

$$\mu = V \cos \alpha / (\Omega R) \quad (5.4)$$

where α is tilt angle, Ω is angular velocity, and R is the radius of rotor. C_T is given by

$$C_T = \frac{T}{\rho(\Omega R)^2 A} \quad (5.5)$$

where T is rotor thrust and A is rotor disc area. In their experiment, very fine, powder-like particles were used as dust. The motion of the particle transported by rotor flow was captured by high speed camera (Figure 5.10). Simulation was achieved on a similar rotor and flow condition using the current brownout model. Dust particle density distribution and velocity are shown in Figure 5.11. It can be seen that the numerical model was able to capture the same extent of the brownout cloud. Another remarkable feature captured by the present model is the stagnation region of the dust particle on the ground at about one radius upstream.

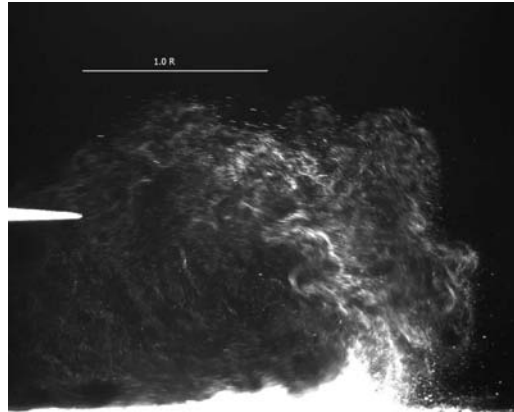
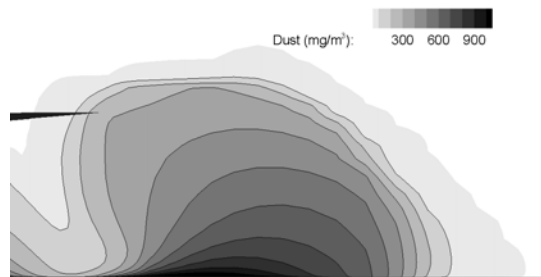
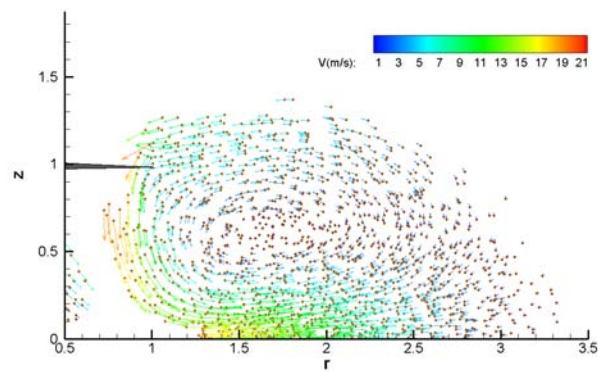


Figure 5.10 Particle transport by rotor downwash in wind tunnel experiment (Nathan et al. (2008) [44])



(a) Dust particle Density



(b) Particle velocity vector

Figure 5.11 Dust particle distribution predicted by brownout model

5.2 Turbulence Model Comparison for Rotor in Ground Effect

For the selection of an appropriate turbulence model for further studies, simulation was carried out with all turbulence models to solve for turbulent rotor flow. The focus of this study was to verify the ability of various turbulence model to predict rotor outwash and wall jet of a hovering rotor in ground effect. This study used the CH-53E rotor, hovering at a height of two rotor radius at thrust coefficient $C_T = 0.007$. The field test data are documented by Preston [45].

Comparisons of various turbulence models (Laminar, Baldwin-Lomax, Spalart Allmaras, Standard $k-\epsilon$, and Realizable $k-\epsilon$) with flight test data and Vorticity Transport Model (VTM) used by Phillips and Brown [46] for ground velocity profiles at different radial locations are shown in Figure 5.12.

As seen in these plots, all models under-predict the maximum wall jet velocity particularly close to the rotor, at radial position $r/R = 1.0, 1.25$ and 1.5 . The reason might be due to the presence of the fuselage in flight test data not modeled in the current simulations. In the wall jet region at $r/R = 1.75$ and above, all models closely predict maximum wall jet velocity. Although at farther radial locations, models predict lower velocity at higher height. This might be due to numerical diffusion caused by first order schemes and the turbulence models used. Near the wall jet region, Standard $k-\epsilon$ and Realizable $k-\epsilon$ have the best comparisons.

Based on the these outcomes and results from the circular impinging jet case, the Realizable $k-\epsilon$ model was found to be most suitable and was used for all subsequent simulations.

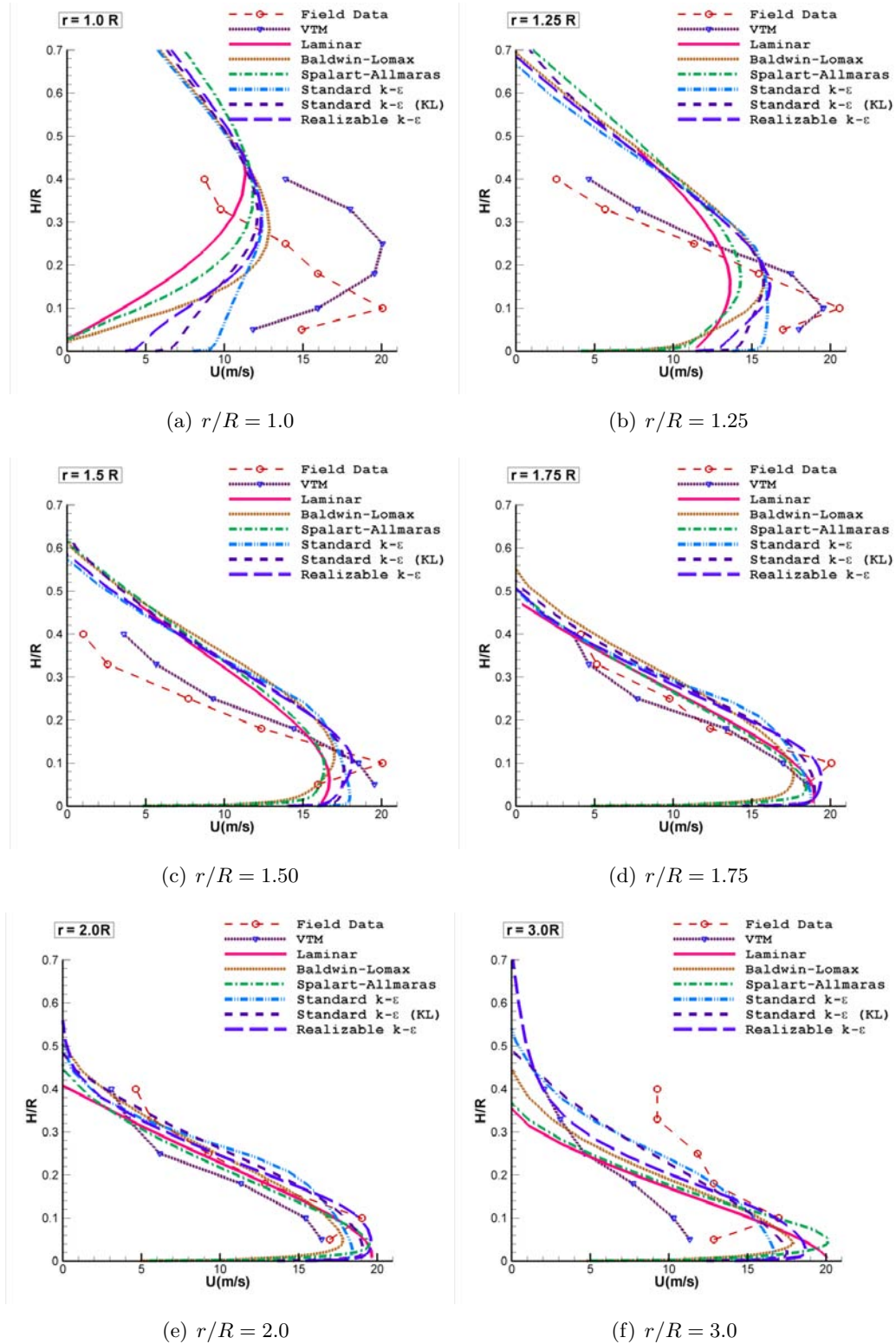


Figure 5.12 Ground velocity profile for hovering CH-53E rotor

5.3 Fuselage Effect on Wake and Ground Signature

To study the effects of body (fuselage) on wake and ground signature of the rotor, single rotor helicopter was used for simulation at different heights in ground effect (IGE). Two sets of simulations were completed, first without the fuselage (named rotor configuration) and second with fuselage (named rotor-fuselage configuration). Height of the rotor center was varied from $H = 0.5R$ to $8R$. The properties of the rotor are given in Table 5.1.

Table 5.1 Rotor properties for helicopter in hover

Rotor radius(R)	12m
Number of blades	7
Twist	-17° (linear)
Root cutout	0.325
Hinge offset	0.0633
Chord	0.0617R

The blade collective pitch was maintained so that the coefficient of thrust was 0.007 when hovering at $H = 1.0R$.

Simulation was in full turbulence mode, with Realizable $k - \epsilon$ model. The mesh size of 103 and 84 in x and y direction, respectively, was used, with a refined grid around the body. Approximately 50 cells were used along the rotor diameter were used to properly capture the rotor flow. The mesh size in the z direction varied from 75 to 94 for rotors at different heights with a refined grid around the body and rotor. The refined grid with stretching was used near the ground to capture the rotor outwash properly. Simulation time for each configuration was between 15 to 25s, depending upon the time required by the wall jet to reach the steady state.

The ground signature was represented as the distribution of friction velocity ($u_* = \sqrt{\tau_w/\rho}$) along the ground. This gave an idea of erosion capability of the rotor downwash and outwash. The erosion and dust entrainment took place in the region where the ground friction velocity was higher than the particle threshold friction velocity. Ground signature of rotor wake and oil flow pattern, with and without fuselage, at different heights are shown in Figures 5.13 to 5.21. The black color circle shows the position of the rotor.

As seen, effects of fuselage are significant at most heights. At lower height of $H = 0.5$ and

$0.75R$, the strength and extent of ground signature outside the rotor perimeter is not much different for rotor and rotor-fuselage configuration, except near the tail of fuselage. There is a fuselage footprint of low friction velocity zone just below the rotor. The effect is more pronounced between height of $H = 1.0$ and $3R$. A zone of high ground friction velocity around the perimeter of rotor was observed for rotor-fuselage configuration between these heights. This is due to an increase in downwash velocity in the presence of a body in the rotor wake. The extent of the ground signature is almost the same between both configurations except it is a little distorted due to the tail of the fuselage in the rotor-fuselage configuration.

An interesting observation was found in the pattern of oil flow distribution for rotor-fuselage configuration. With an increase in rotor height, the shadow of the fuselage (tadpole-like shape made by the oil flow pattern) can be seen rotating counter-clock wise. This is due to the swirling flow nature of the rotor wake.

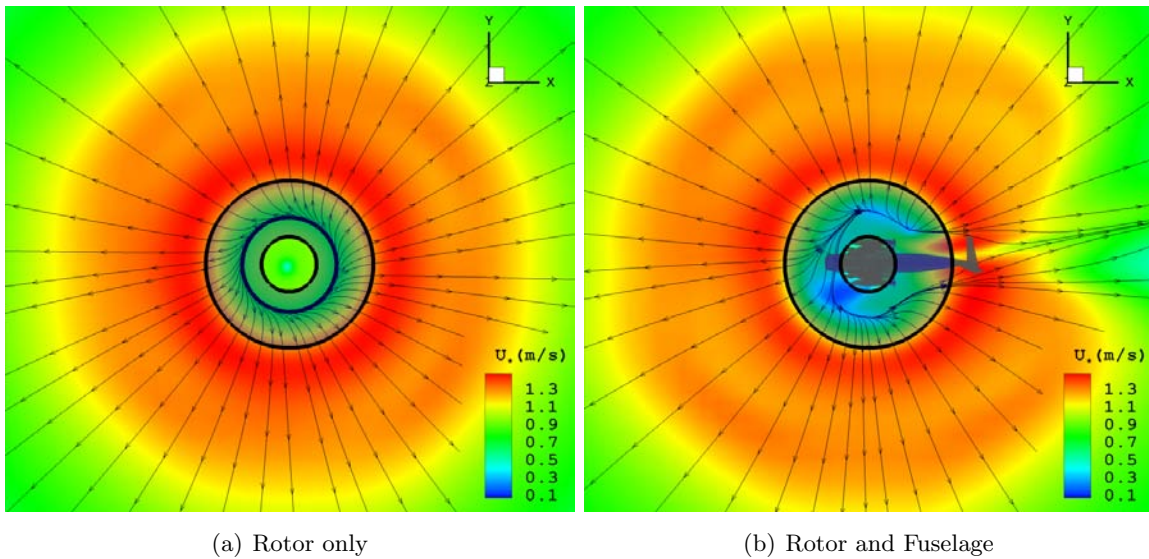


Figure 5.13 Ground friction velocity at rotor height $H = 0.5R$

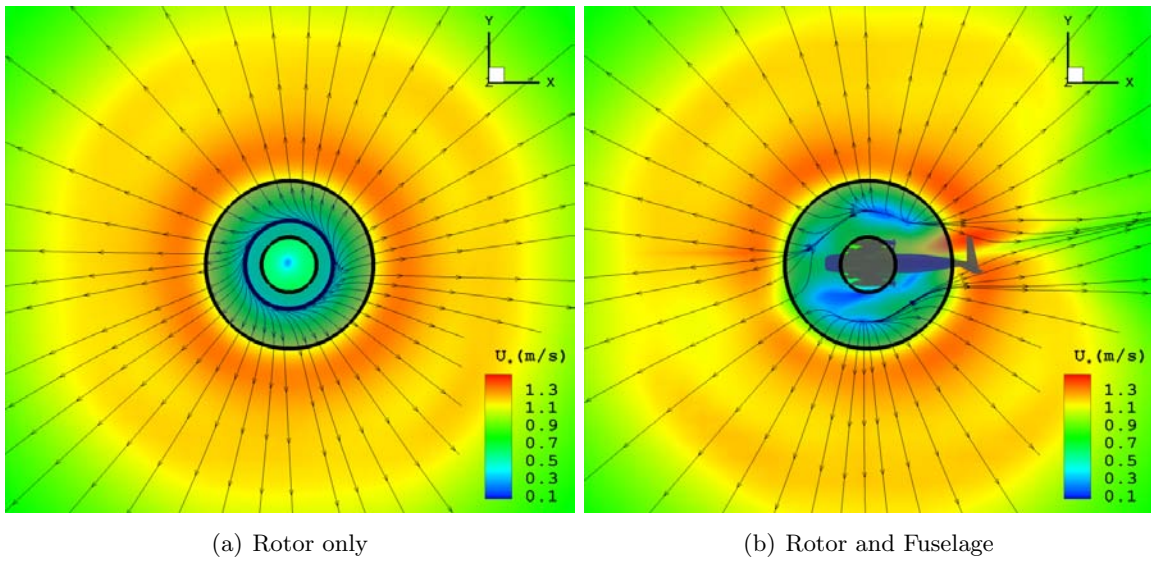


Figure 5.14 Ground friction velocity at rotor height $H = 0.75R$

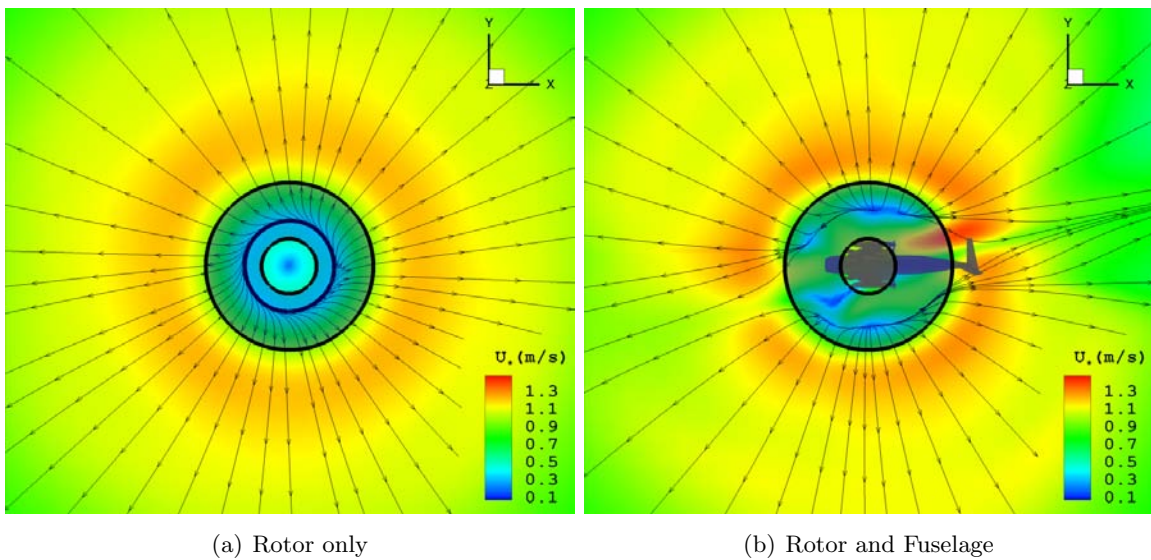


Figure 5.15 Ground friction velocity at rotor height $H = 1.0R$

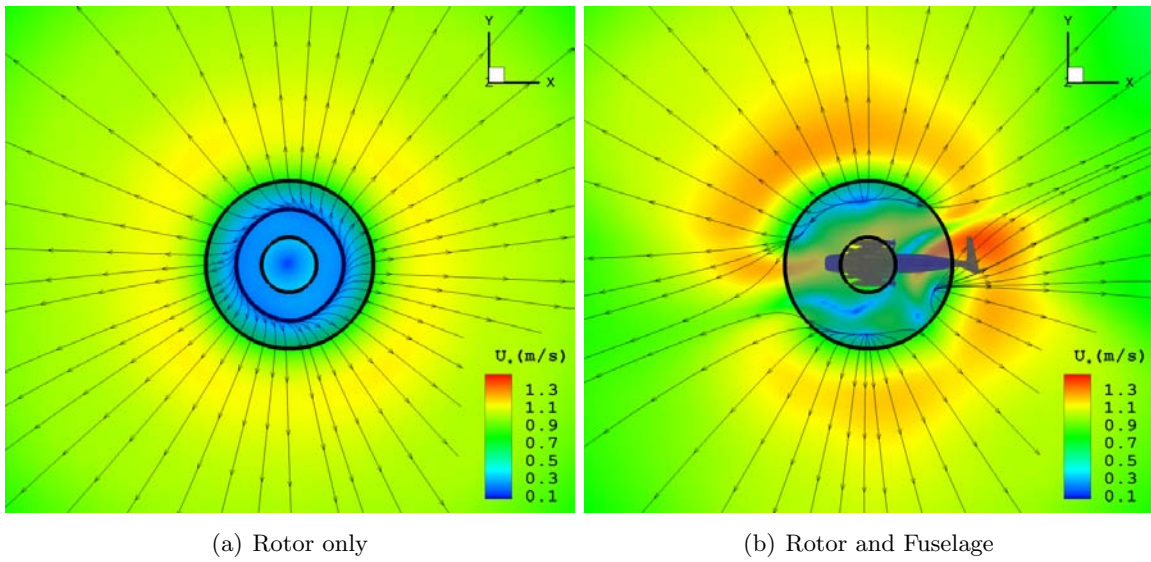


Figure 5.16 Ground friction velocity at rotor height $H = 1.5R$

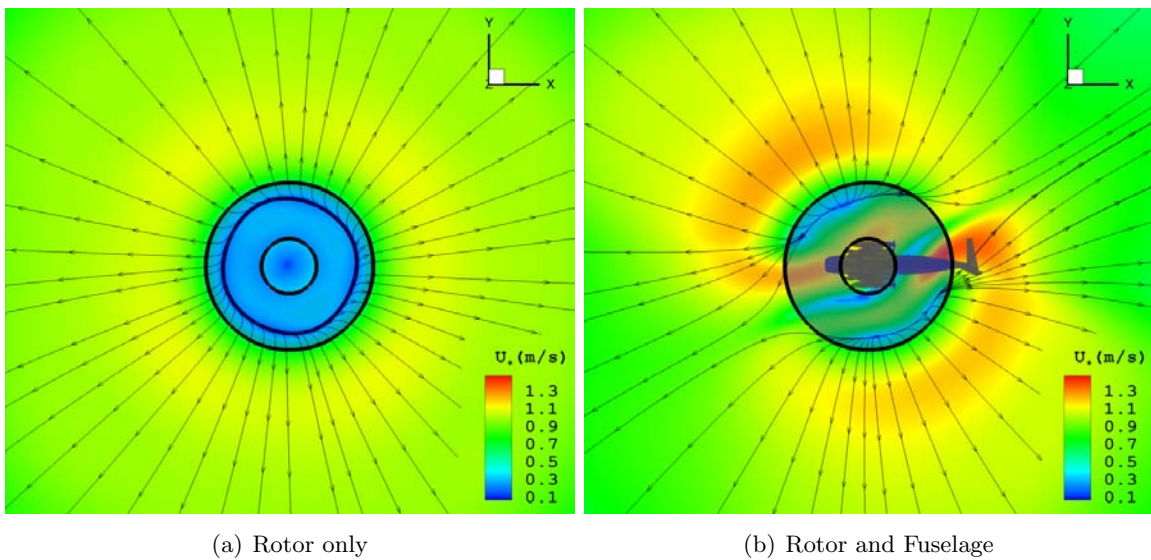


Figure 5.17 Ground friction velocity at rotor height $H = 2.0R$

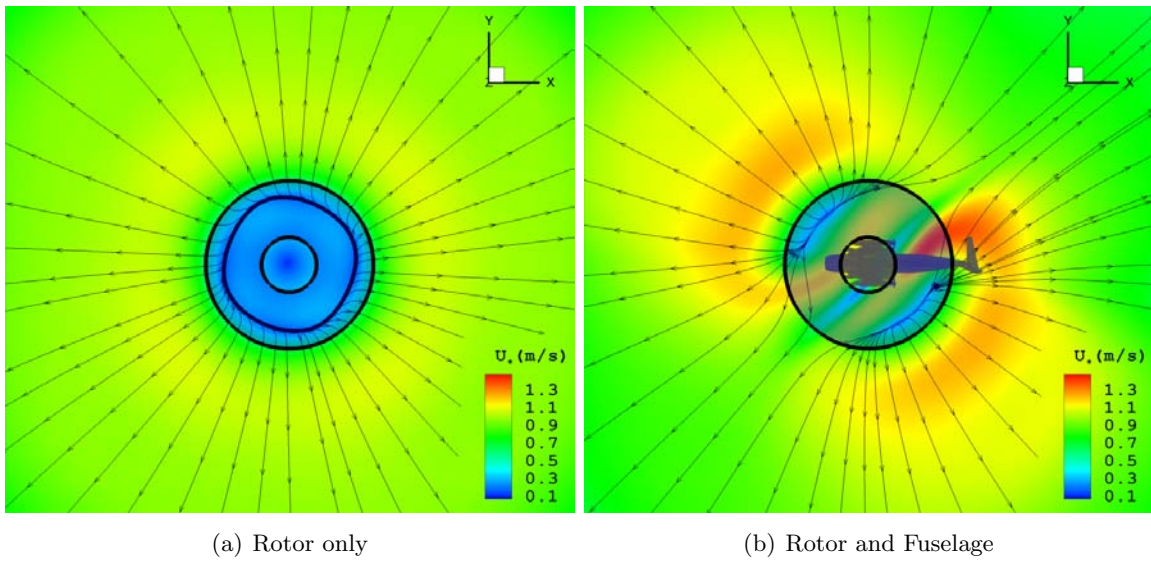


Figure 5.18 Ground friction velocity at rotor height $H = 2.5R$

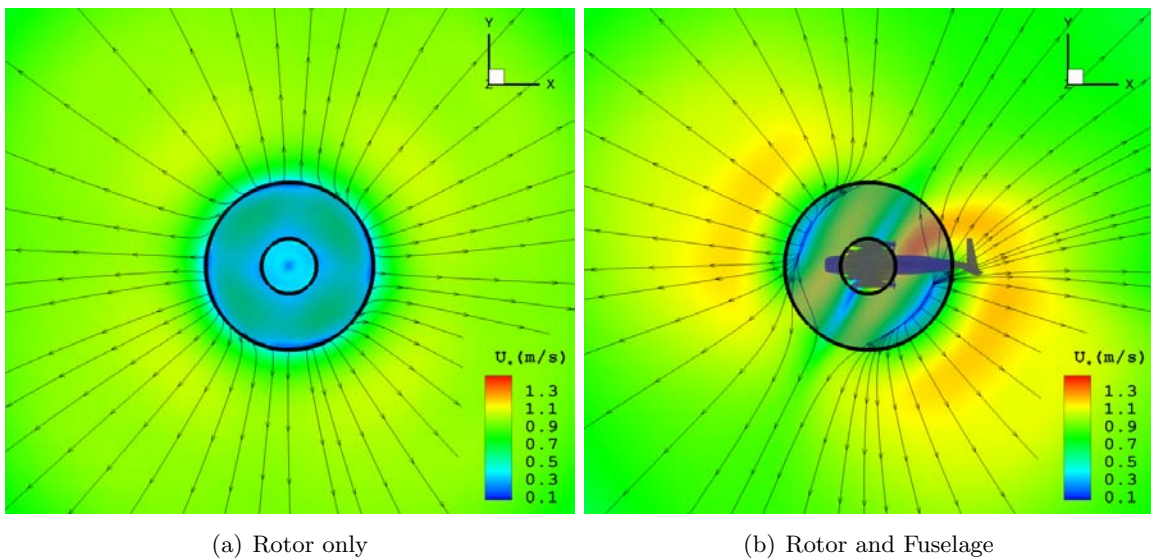


Figure 5.19 Ground friction velocity at rotor height $H = 3.0R$

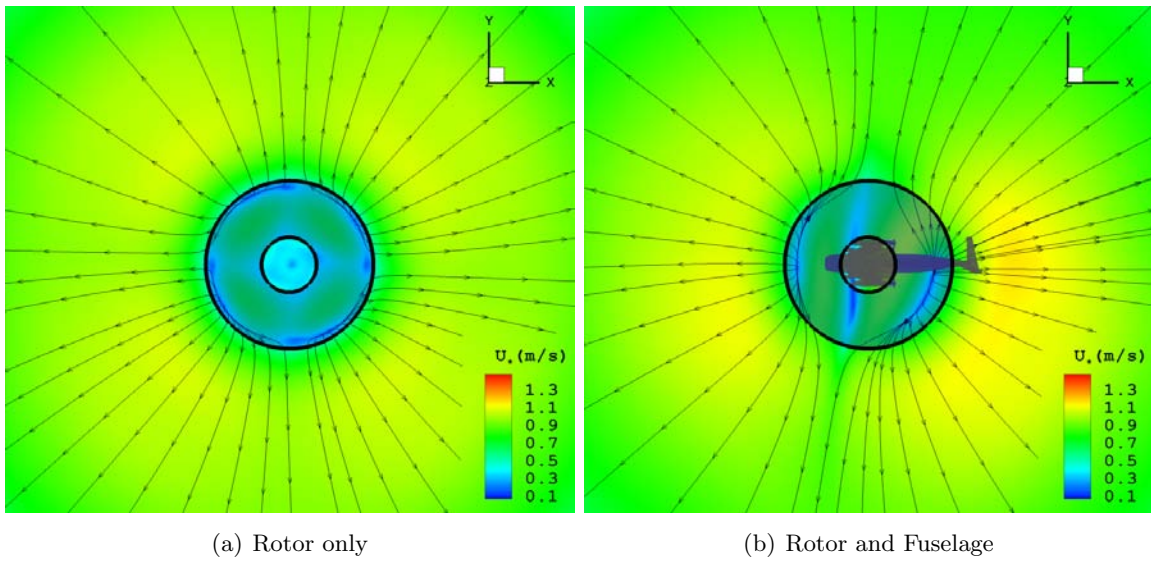


Figure 5.20 Ground friction velocity at rotor height $H = 4.0R$

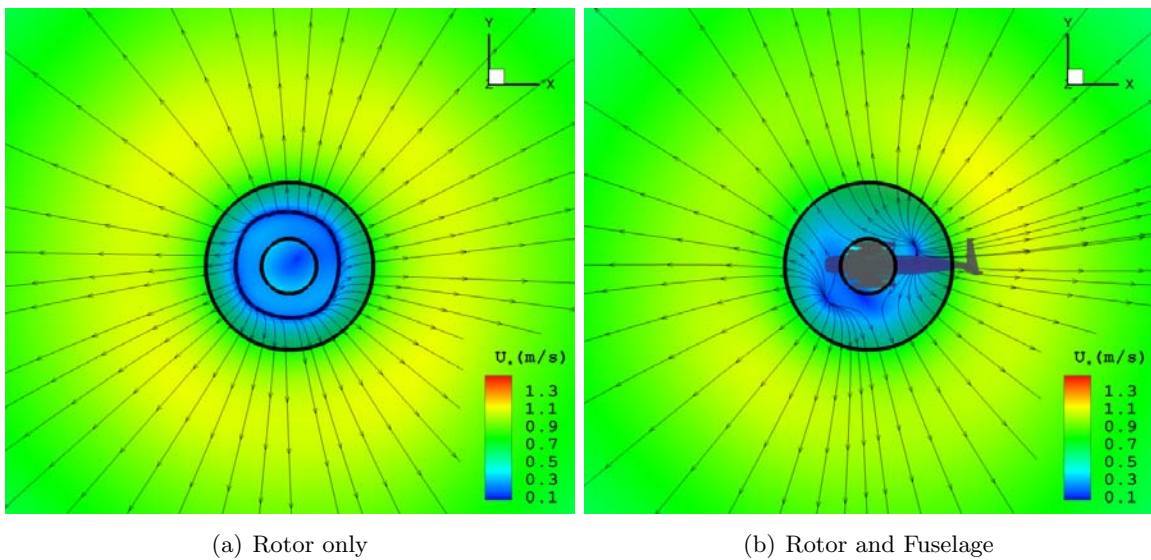
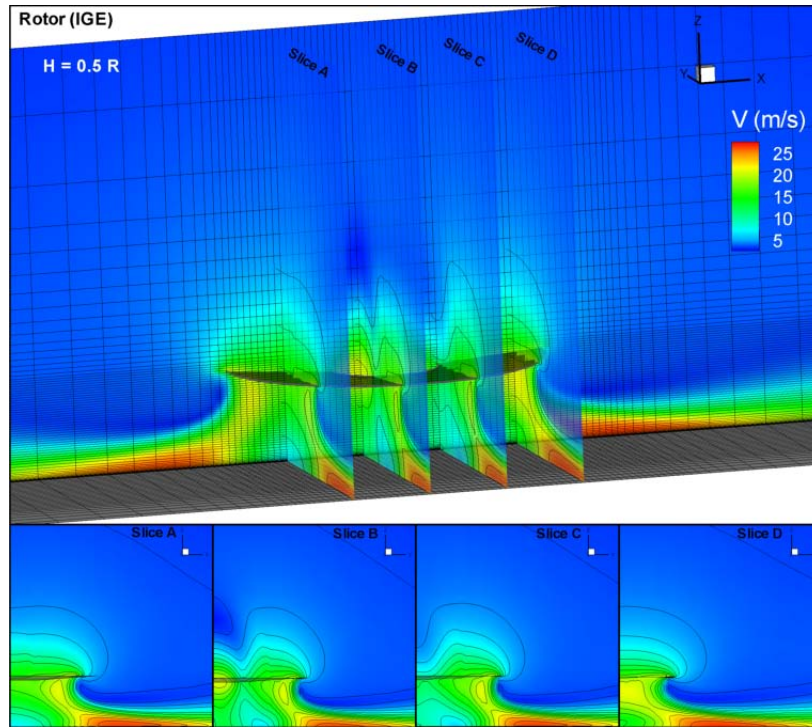


Figure 5.21 Ground friction velocity at rotor height $H = 8.0R$

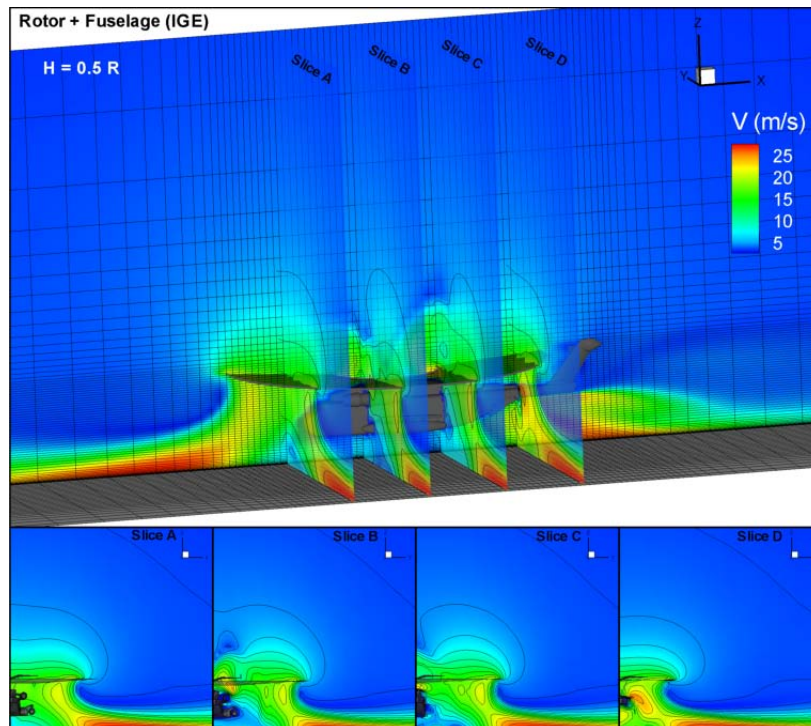
The contour plot of velocity magnitude for rotor and rotor-fuselage configuration at rotor height of $H = 0.5$ to $2R$ is shown in Figures 5.22 to 5.25. This plot is shown in the longitudinal plane (along the fuselage) and four cross planes (slices) as show in the figures. A front view of all planes (slice A to D) is shown in four thumbnails below each figure.

It is observed that at height $0.5R$, the rotor wake and outwash are not much affected by the presence of the fuselage. The same observation can be found in the ground signature discussed earlier. At heights $H = 1.0$ to $2.0R$, the effect of fuselage can be clearly seen in all slices. In addition to the unsteady behavior below the fuselage, two major differences are the increase in the bulk velocity of rotor wake and increase in the wall jet velocity. Presence of fuselage decreases the flow area, thus, the fuselage increases the downwash velocity. Increase in downwash velocity increases the wall jet velocity.

The ground velocity profile at three different lateral positions from rotor center ($y = 1, 2,$ and $3R$) for different rotor heights are shown in Figure 5.26. The comparison has been made between rotor configurations and rotor-fuselage configurations. As seen in the figure, the velocity profile for both configurations are not much different at lower heights ($H = 0.5$ and $0.75R$). As observed earlier, fuselage effect is most significant between $H = 1.0$ to $3R$, after which the effect starts to decrease. The maximum wall jet velocity at three radial locations for different heights is plotted in Figure 5.27. At the lateral position $y = 1.0R$, the wall jet velocity first decreases with height for heights below $3R$ and then increases for higher heights for both configurations. At all the heights, the wall jet velocity for the rotor-fuselage configuration is always higher at this position. At the lateral position $y = 2.0R$, the wall jet velocity decreases and becomes asymptotic to a constant value. At lower heights, $H < 2.5R$, wall jet velocity for the rotor-fuselage configuration is higher than the rotor configuration. There is a crossover at $H = 2.5R$. The wall jet velocity for the rotor is higher. This same trend is observed at $y = 3.0R$, but the crossover takes place at $H = 2R$. The difference in wall jet velocity between both configurations follows the same trend at all the locations, which reaches a maximum around $H = 1.5R$.

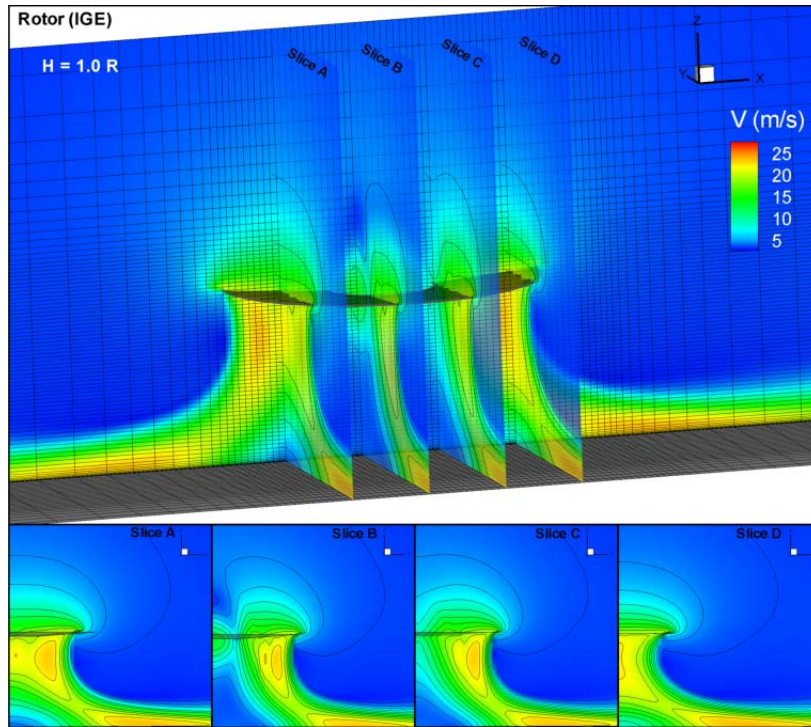


(a) Rotor only

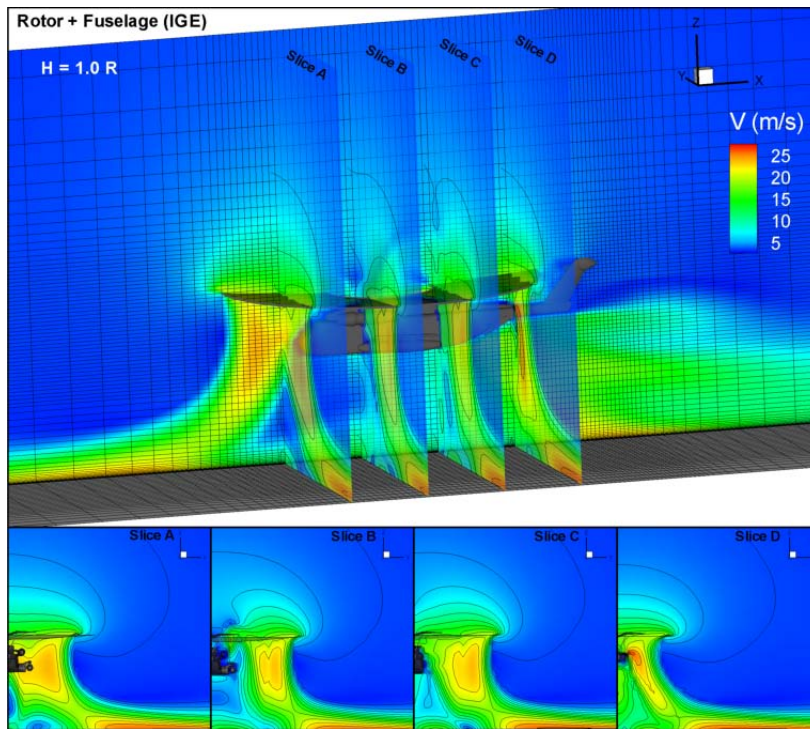


(b) Rotor and Fuselage

Figure 5.22 Velocity magnitude contours at $H = 0.5R$

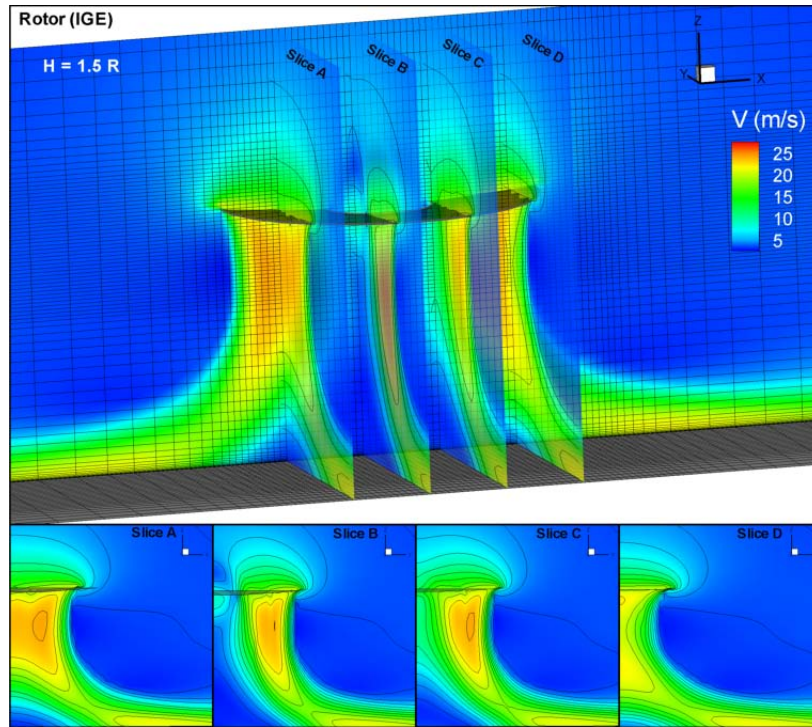


(a) Rotor only

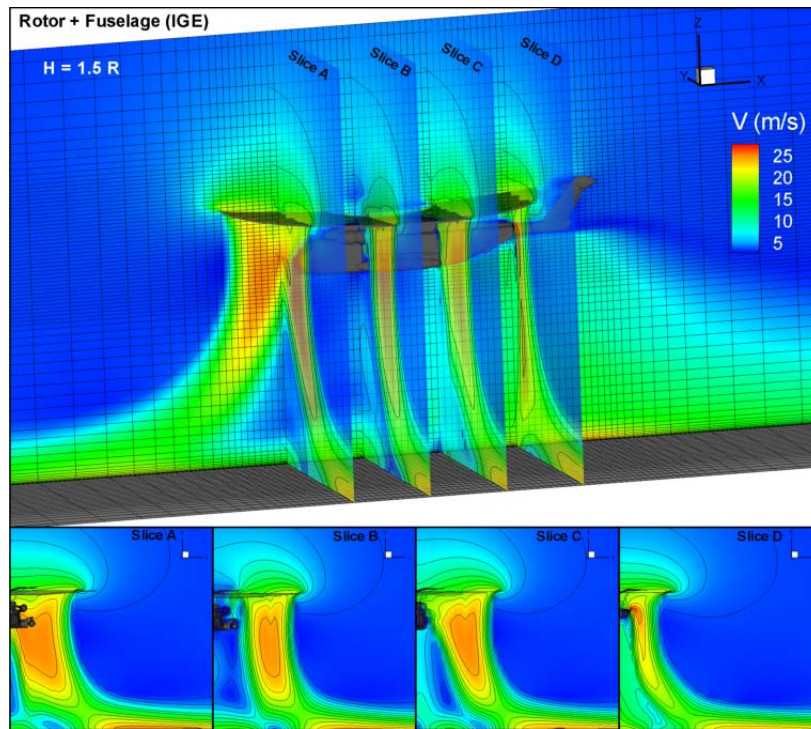


(b) Rotor and Fuselage

Figure 5.23 Velocity magnitude contours at $H = 1.0R$

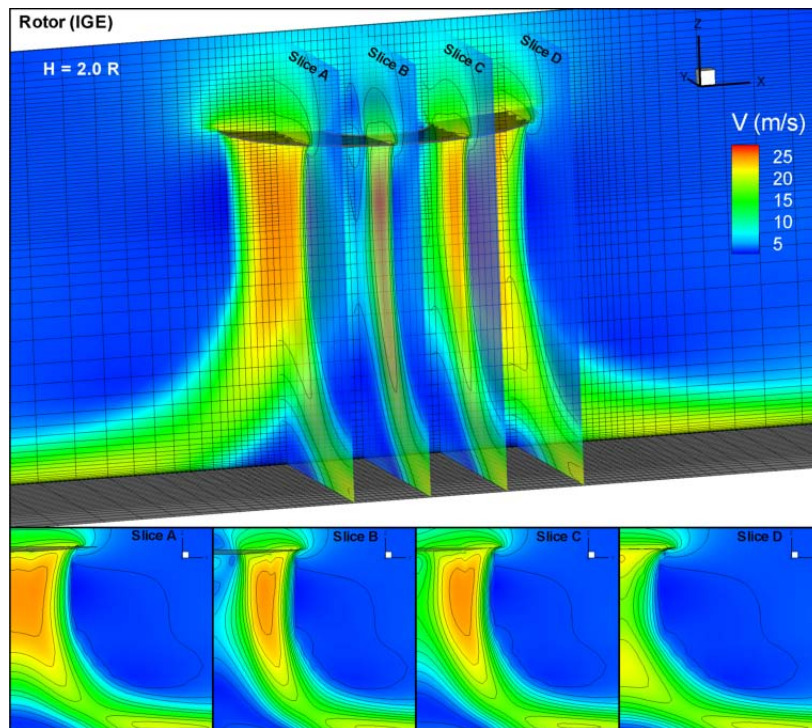


(a) Rotor only

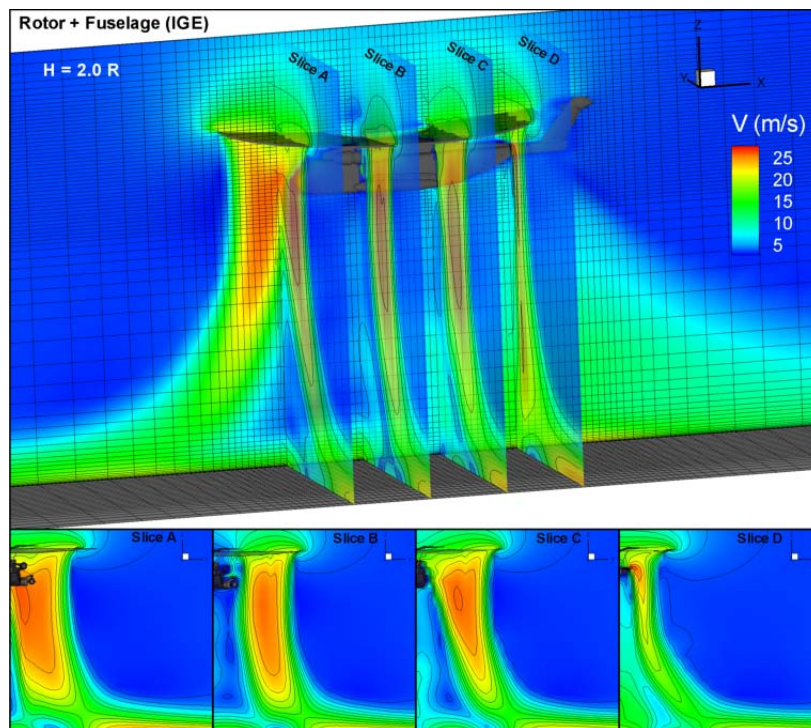


(b) Rotor and Fuselage

Figure 5.24 Velocity magnitude contours at $H = 1.5R$



(a) Rotor only



(b) Rotor and Fuselage

Figure 5.25 Velocity magnitude contours at $H = 2.0R$

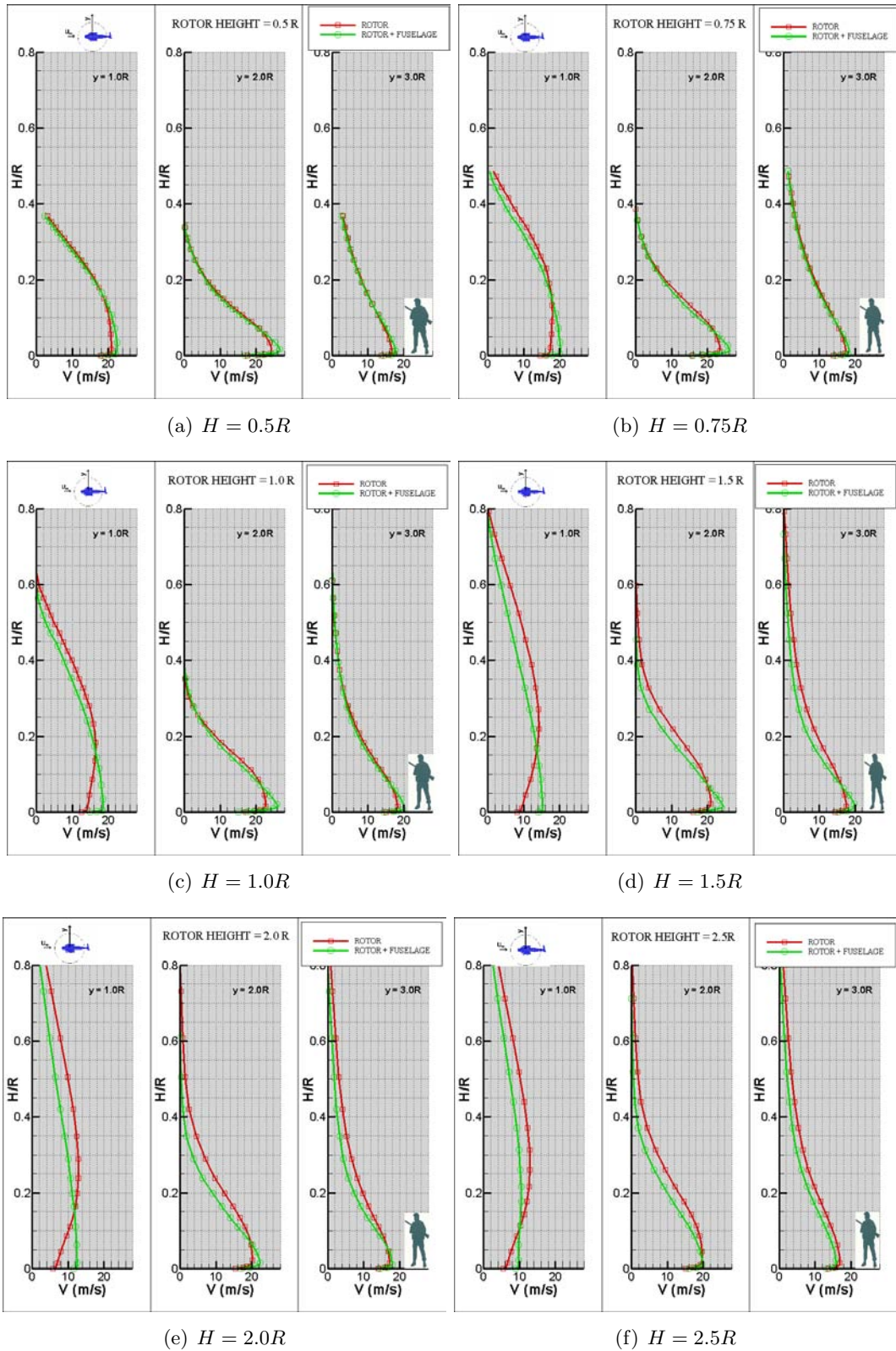


Figure 5.26 Ground velocity profile at different radial location for different rotor heights

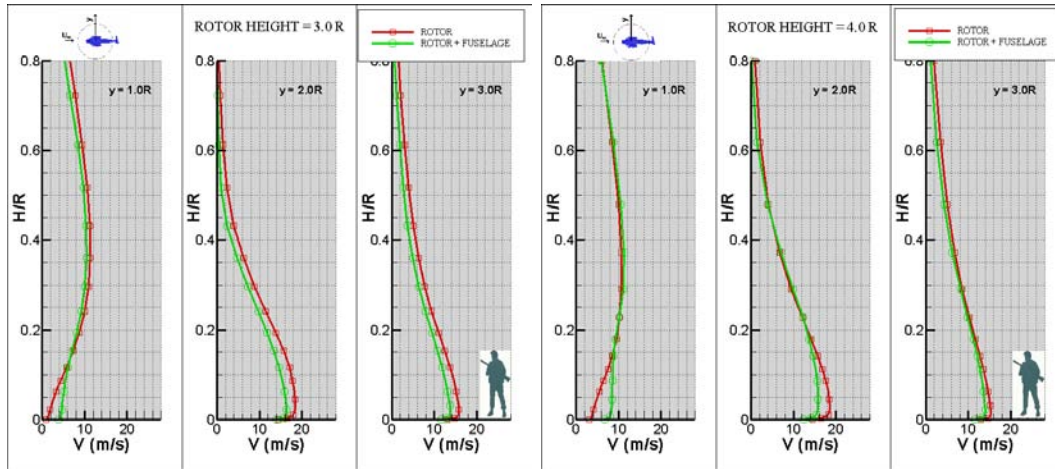
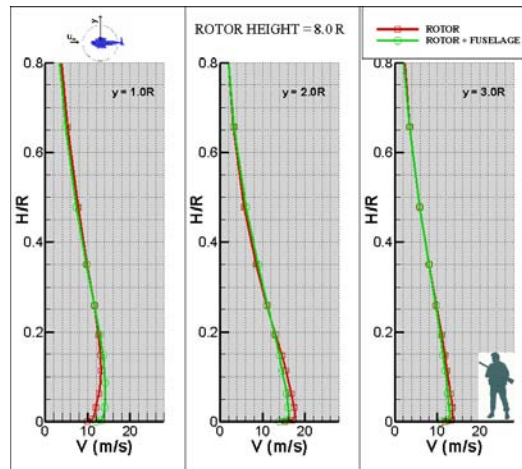
(a) $H = 3.0R$ (b) $H = 4.0R$ (c) $H = 8.0R$

Figure 5.26 (continued) Ground velocity profile at different radial location for different rotor heights

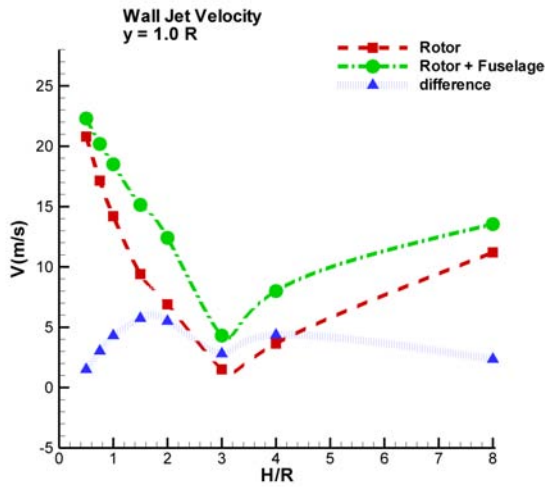
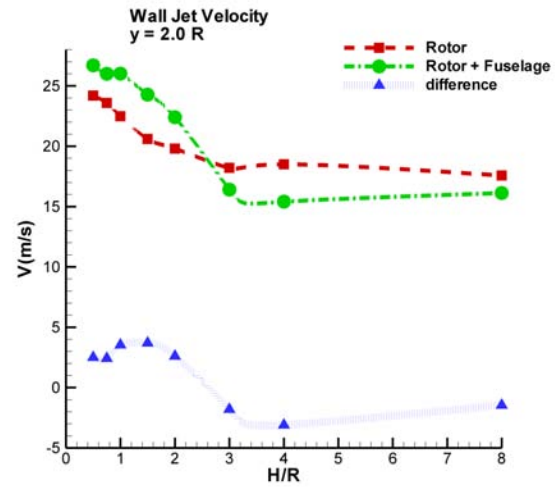
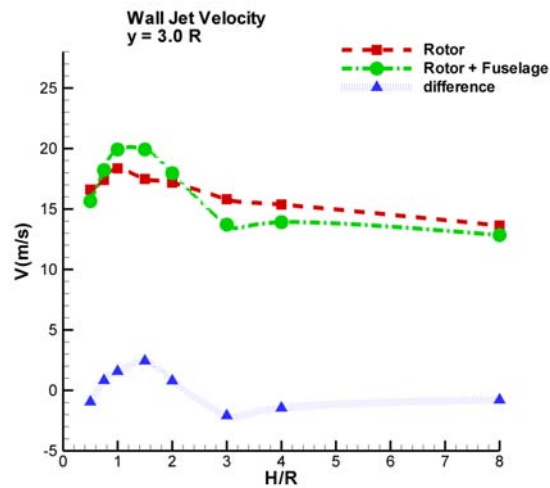
(d) $y = 1.0R$ (e) $y = 2.0R$ (f) $y = 3.0R$

Figure 5.27 Wall jet velocity at different radial locations

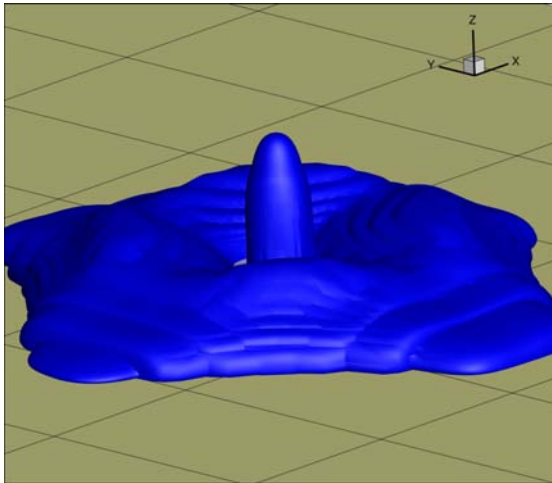
5.4 Fuselage Effect on Brownout

To study the fuselage effect of the brownout, the particle transport model has been used for two configurations, rotor-only configuration and rotor-fuselage configuration, at different heights. Rotor properties are the same as in the last section with *NACA0012* airfoil. For all subsequent simulations, particle size of $d_p = 10\mu m$ is used with a particle density of $\rho_d = 2800kg/m^3$. The roughness length on the ground is taken as $z_o = 250\mu m$.

The brownout cloud after $t = 5s$ (≈ 15 rotor revolution) is shown in Figure 5.28 for both configurations. Dust clouds shown in the images are the iso-surface of dust cloud density (ρ_d) of $50mg/m^3$. At a height of $0.5R$, substantial differences in dust cloud patterns are observed. A fountain of dust can be seen coming out around the region of rotor center in rotor-only configuration. In rotor-fuselage configurations, the rise in dust is blocked by the presence of the body. To visualize the dust characteristics near the rotorcraft, the dust cloud in the rear of the rotor center lateral plane (y - z plane) is removed, as shown in Figure 5.29. The various layers (iso surface) of dust density can be seen through the removed side as seen in Figure 5.30, where the x -axis is normal to the images. These images also give an idea of the extent of dust cloud height forming ahead of the rotor. As the height of the rotor increases, the height of the dust fountain at the rotor's center decreases for rotor configurations, due to the effect of rotor downwash. In contrast, for the rotor-fuselage configurations, the height of the dust fountain just below the fuselage increases and attempts to catch up with the fuselage. This is caused by the recirculating flows in the wake of the fuselage, which lift the dust higher, as seen in the particle path lines plots in Figure 5.31. This effect of the recirculating flows and the height of the fountain below the fuselage decreases after a height of $2.0R$. At all these heights, the dust density in the dust fountain is much higher in the rotor-fuselage simulations. Even in the rotor outwash region, higher density clouds (larger iso-surface value) are found in the rotor-fuselage simulations.

Although the core of dust clouds in the rotor-fuselage configuration are determined denser, the average height achieved by the dust cloud is almost the same for both configurations at each height.

Rotor Only

(a) $H = 0.5R$

Fuselage and Rotor

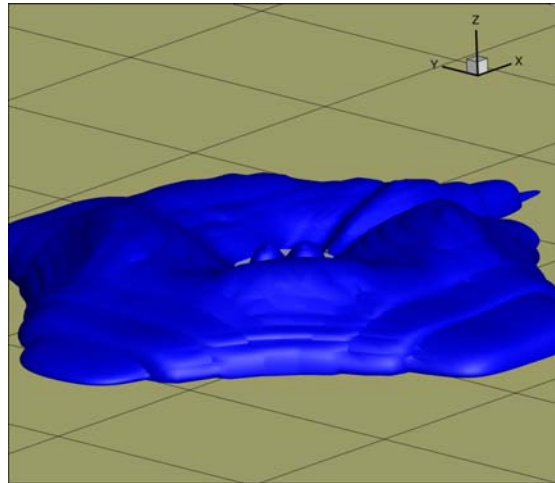
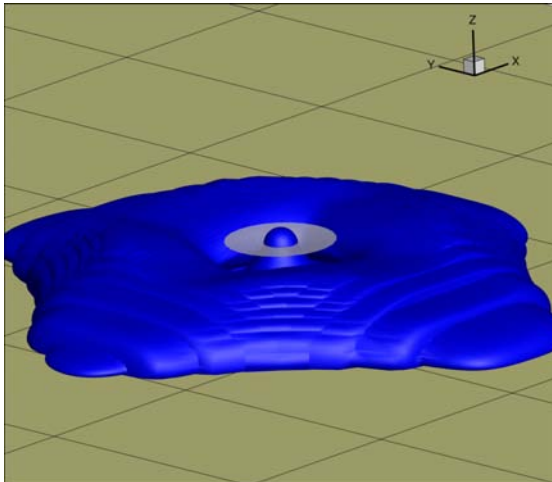
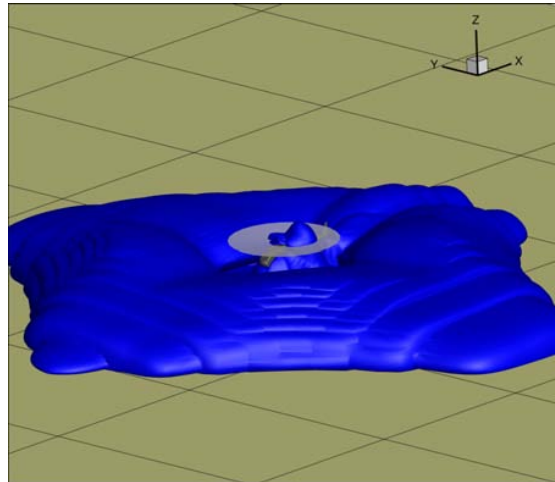
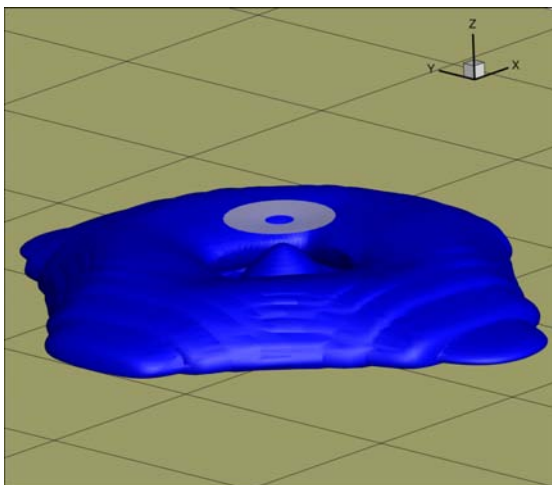
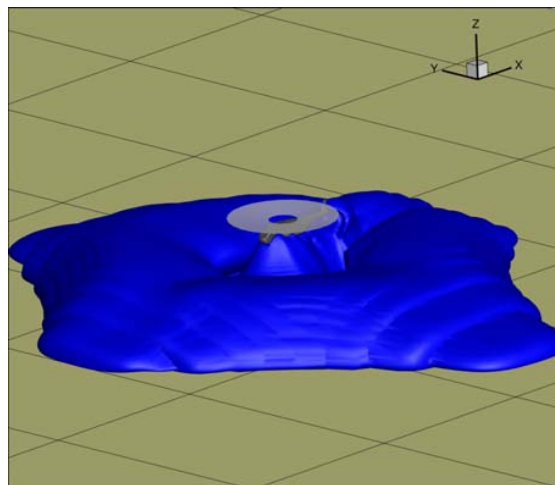
(b) $H = 0.5R$ (c) $H = 1.0R$ (d) $H = 1.0R$ (e) $H = 1.5R$ (f) $H = 1.5R$

Figure 5.28 Dust cloud formation after 5s for rotor-only and rotor-fuselage configuration

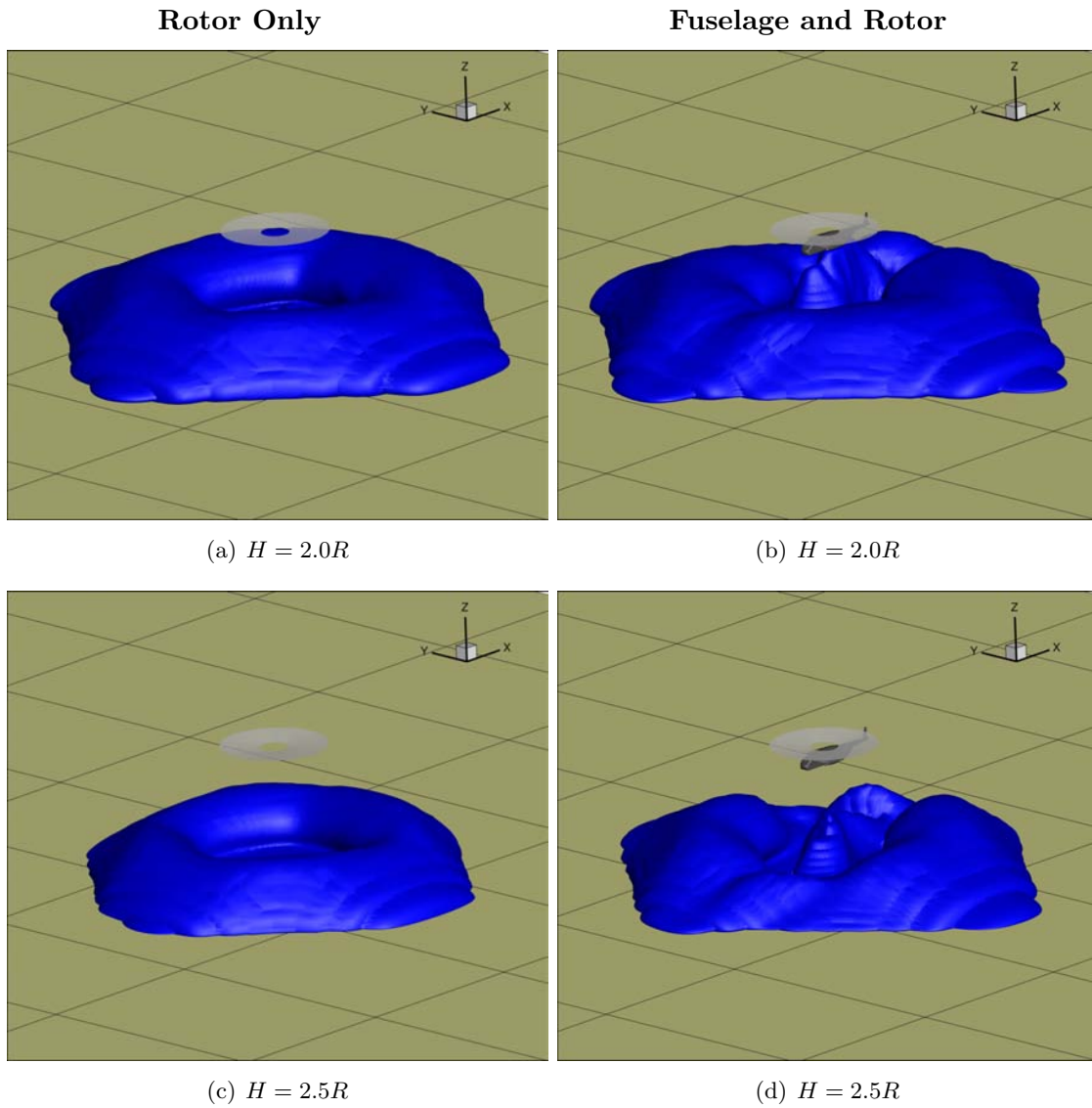


Figure 5.28 (continued) Dust cloud formation after 5s for rotor-only and rotor-fuselage configuration

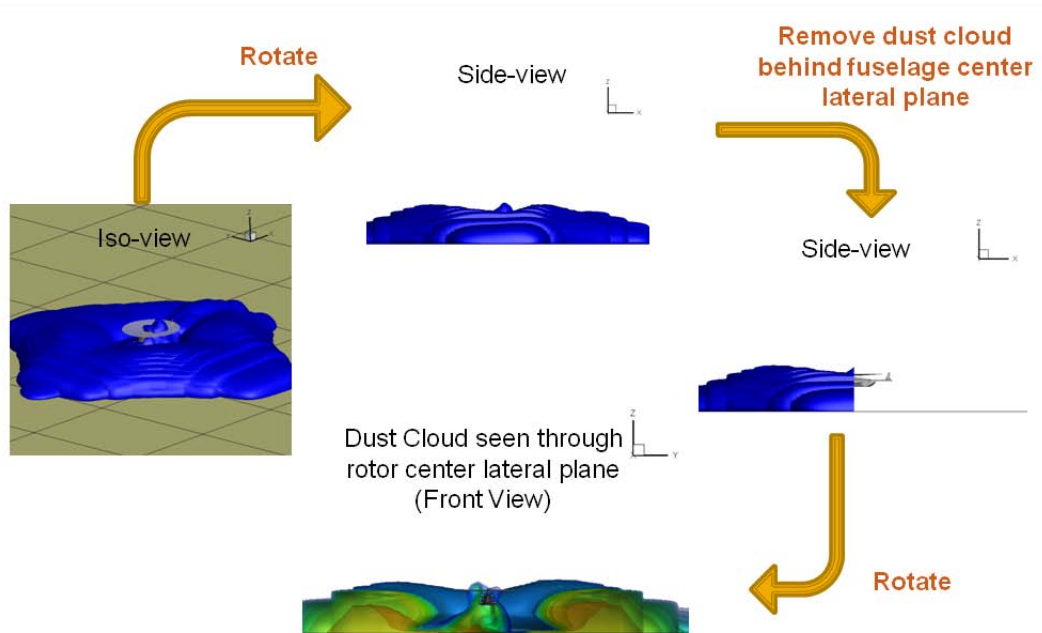


Figure 5.29 Visualizing dust cloud characteristics

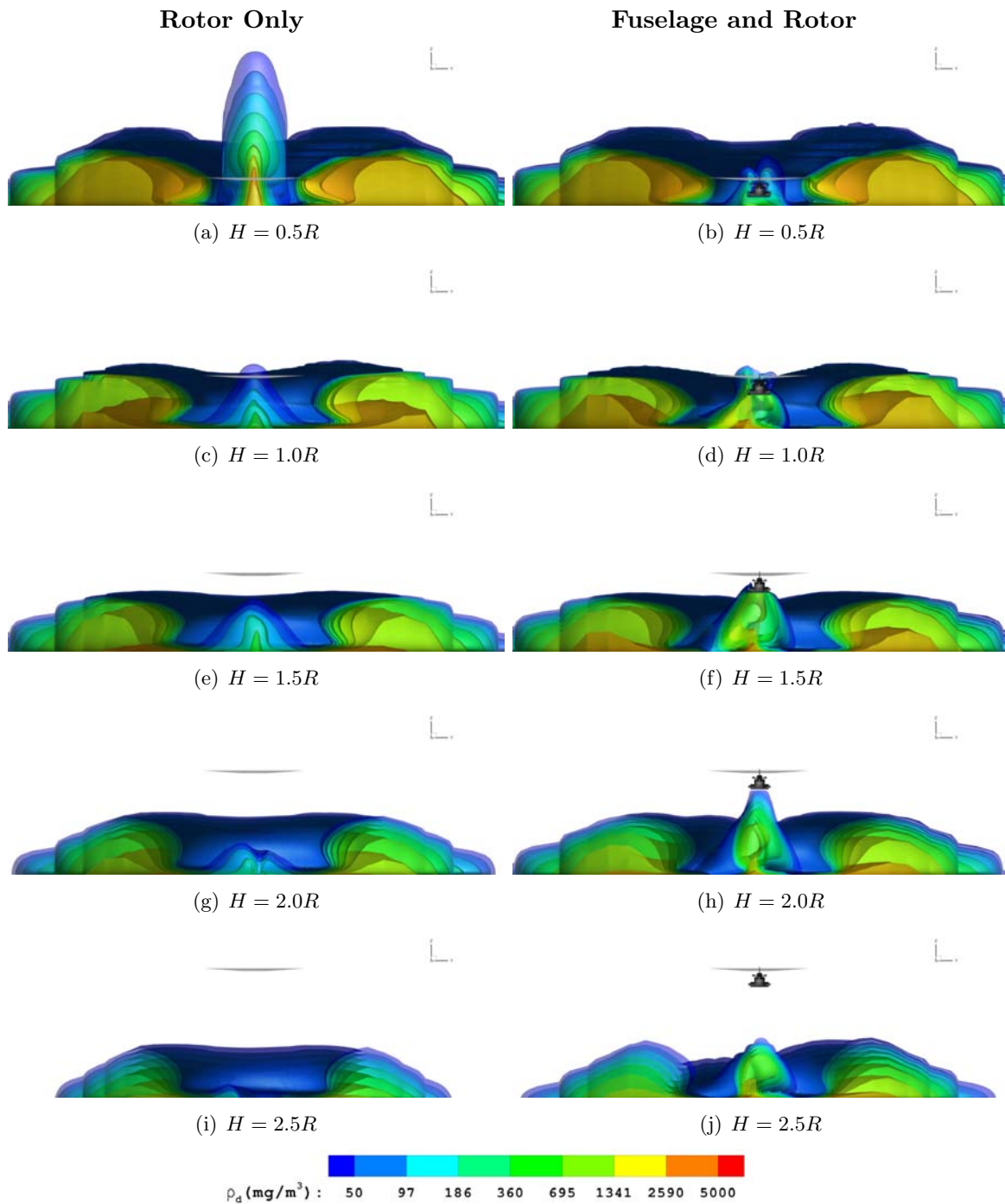


Figure 5.30 Dust cloud characteristics seen through rotor center cut plane for rotor-only and rotor-fuselage configurations

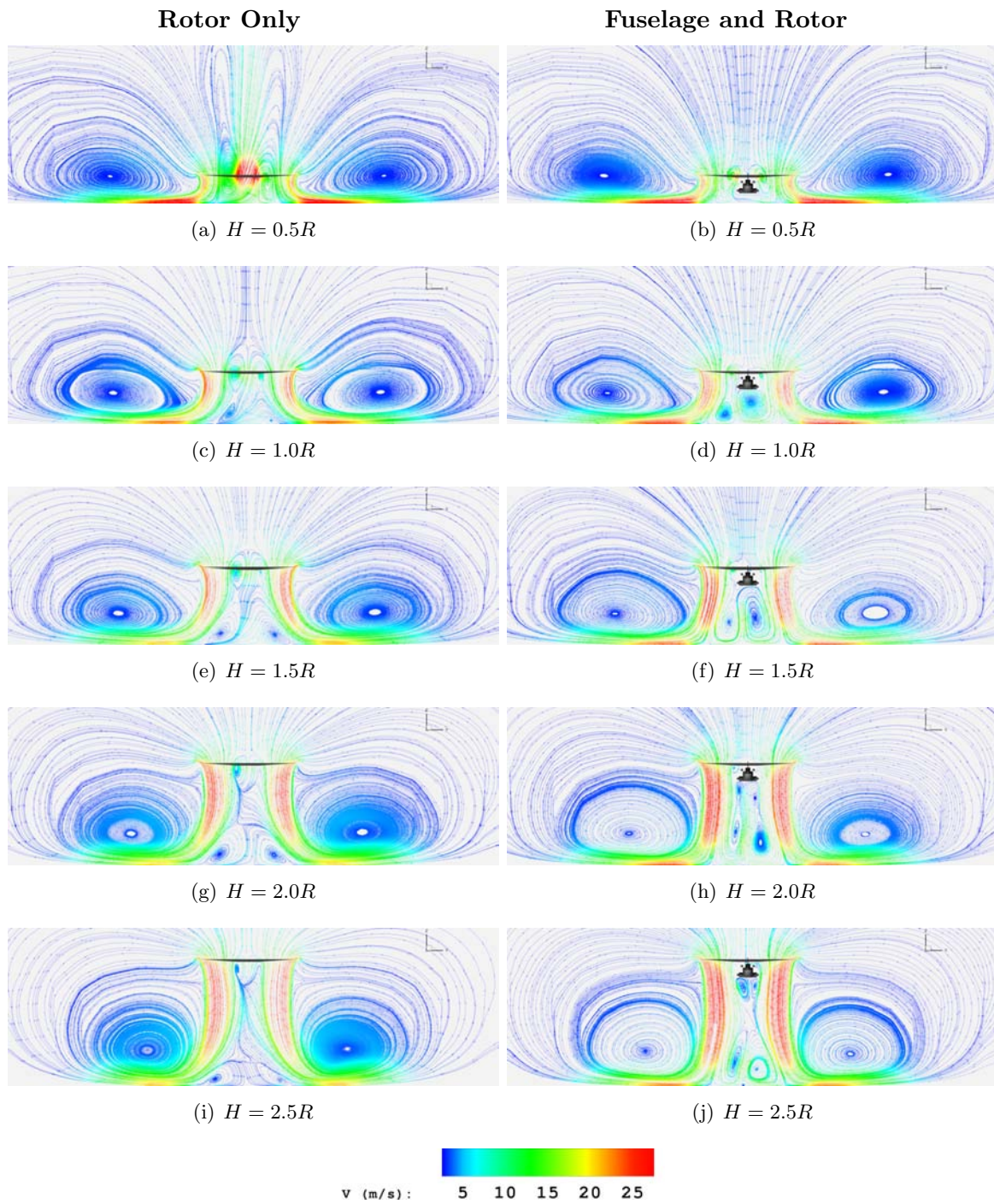


Figure 5.31 Particle path lines at rotor mid plane for rotor-only and rotor-fuselage configurations

5.5 Fuselage Shape Effect on Wake and Ground Signature

To study the effect of fuselage shape on wake and ground signature, four simplified geometries with circular, elliptical, square, and rectangular cross-sections have been used for the fuselage. The width of each fuselage is 9m. The height of elliptical and rectangular fuselage is 7m. The rotor properties are given in Table 5.2. Collective pitch has been set so the coefficient of thrust at $H = 1.0R$ is 0.007 for all the fuselage configurations. This is done by running the simulation for each rotor configuration at different collective pitches to obtain a relation of thrust coefficient and collective pitch, at a particular height. Using this relation, the collective pitch is calculated to get the desired coefficient of thrust.

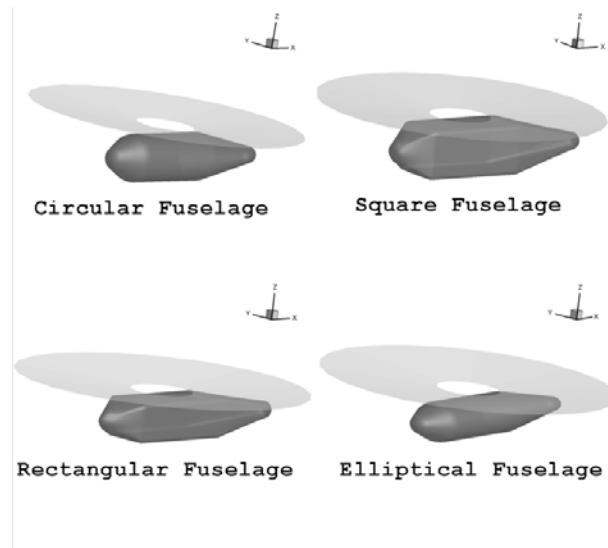


Figure 5.32 Four fuselage shapes used

Table 5.2 Rotor properties for helicopter with different fuselage shape

Rotor radius(R)	8.02m
Number of blades	4
Twist	-12° (linear)
Root cutout	0.2
Hinge offset	0.03
Chord	0.0617 R
Airfoil	<i>NACA0012</i>

The ground signature (ground friction velocity) of each fuselage shape at various heights is

plotted in Figures 5.33 to 5.37. As seen, no significant difference has been found in the ground signature for different fuselage shapes, if the projection of the fuselage on the ground is same.

Contour plot of velocity magnitude and streamline on lateral and longitudinal rotor mid plane are shown in Figures 5.38 to 5.40 for all fuselage shapes at heights of $0.6R$, $1.0R$, and $1.5R$. At height $0.6R$, flow is mostly attached below the fuselage for all configurations, except there is a recirculation just below the fuselage nose for the square, rectangular, and elliptical configurations. At heights of $1.0R$, the region below the fuselage becomes highly unsteady for all configurations. Recirculating flows can be seen in the front view of all configurations. Flow is highly un-symmetric in all cases, due to unsteadiness and the swirling nature of the rotor's downwash. The recirculating region below the fuselage nose is also found in rectangular and square fuselages. Similar trends are observed for all higher heights ($H = 1.5R$ and above).

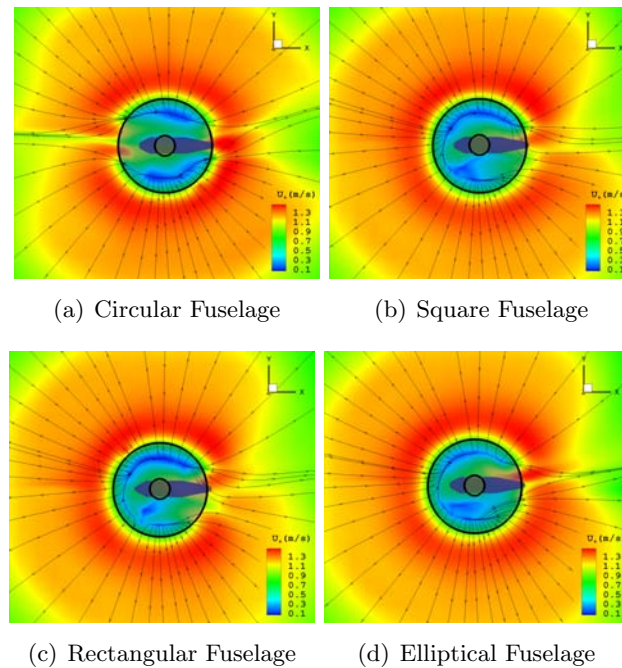


Figure 5.33 Ground friction velocity comparison at $H = 0.6R$

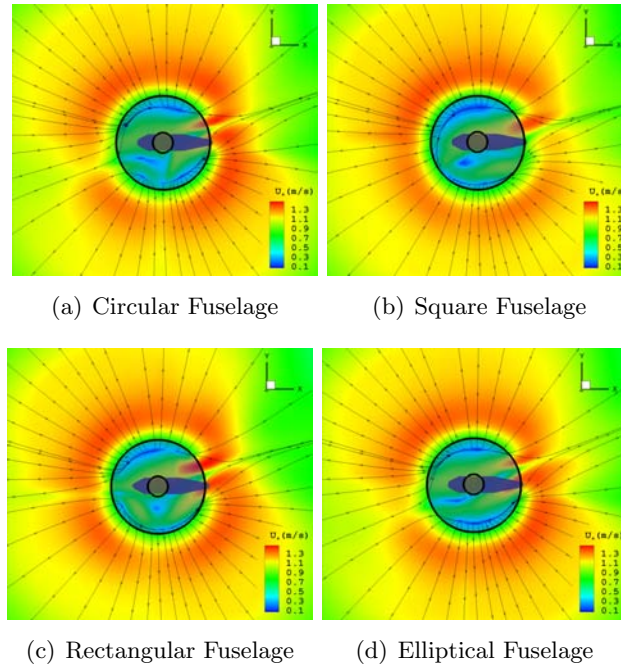


Figure 5.34 Ground friction velocity comparison at $H = 1.0R$

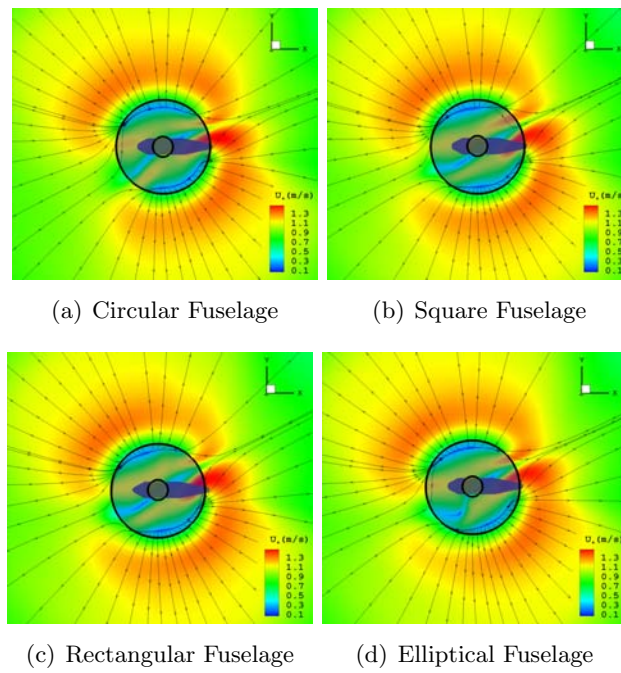


Figure 5.35 Ground friction velocity of different fuselage cross-section at $H = 1.5R$

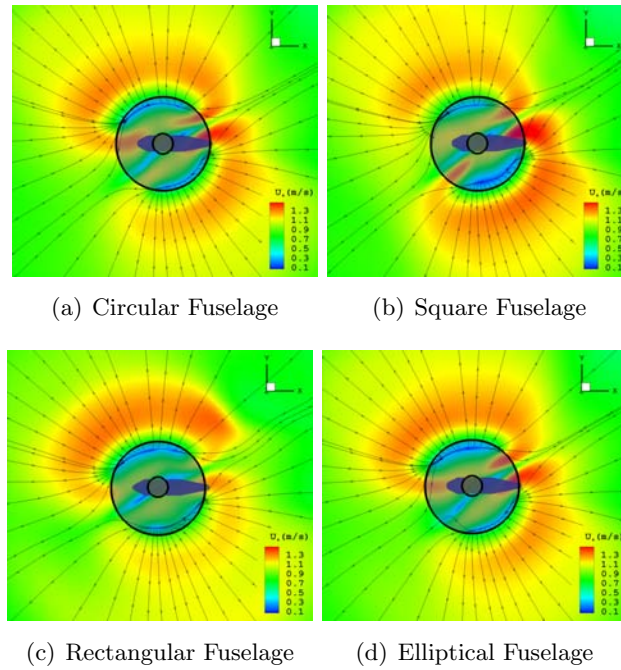


Figure 5.36 Ground friction velocity comparison at $H = 2.0R$

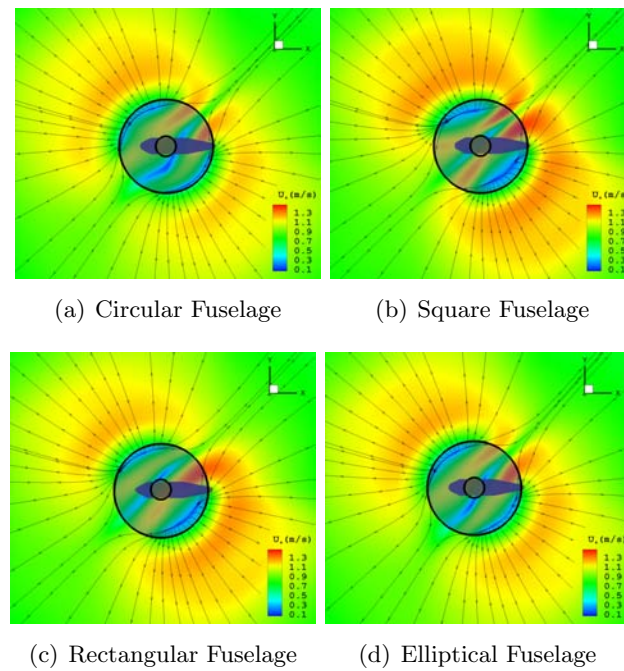


Figure 5.37 Ground friction velocity comparison at $H = 3.0R$

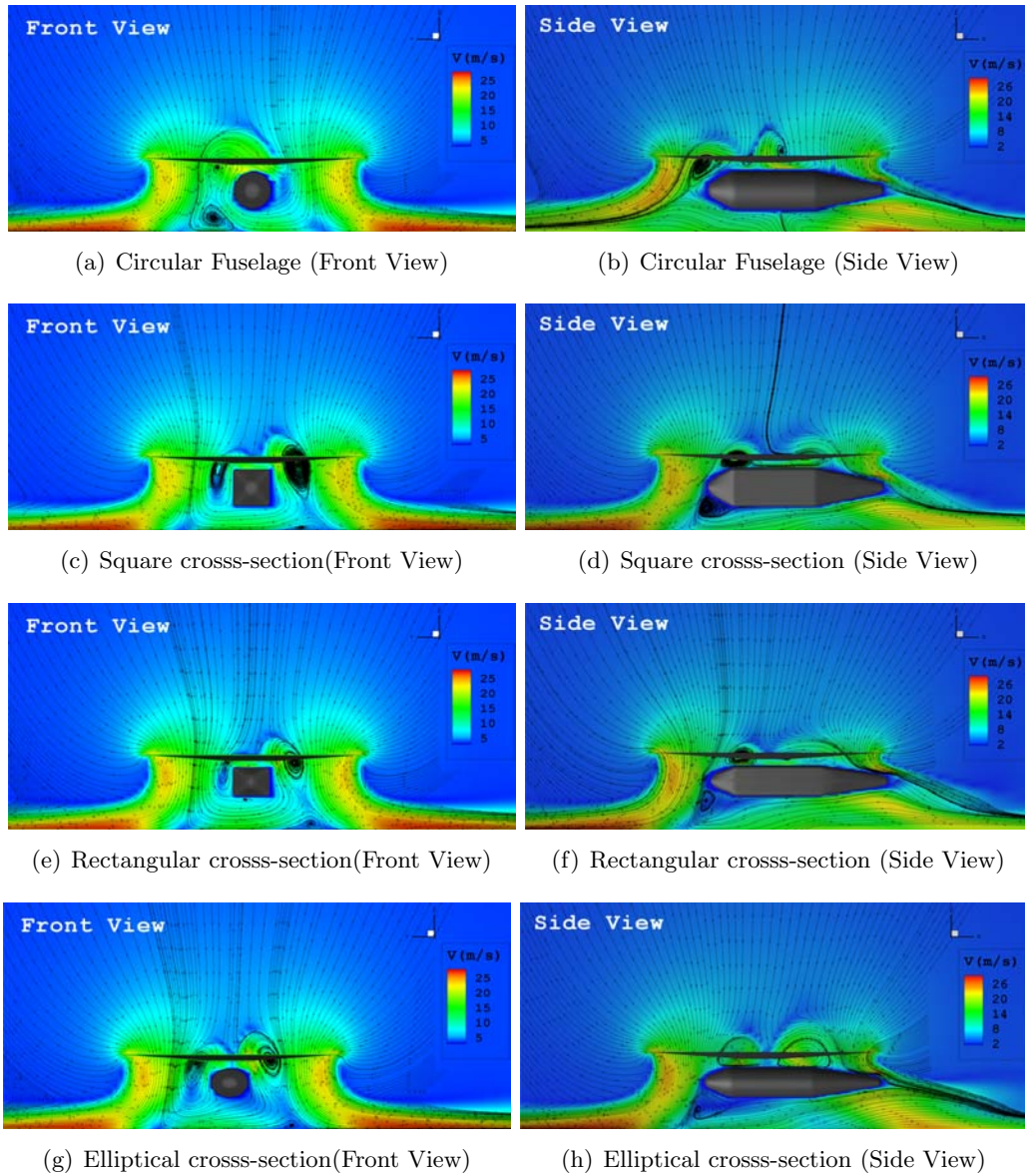


Figure 5.38 Velocity magnitude and streamlines for different fuselage shapes at $H = 0.6R$

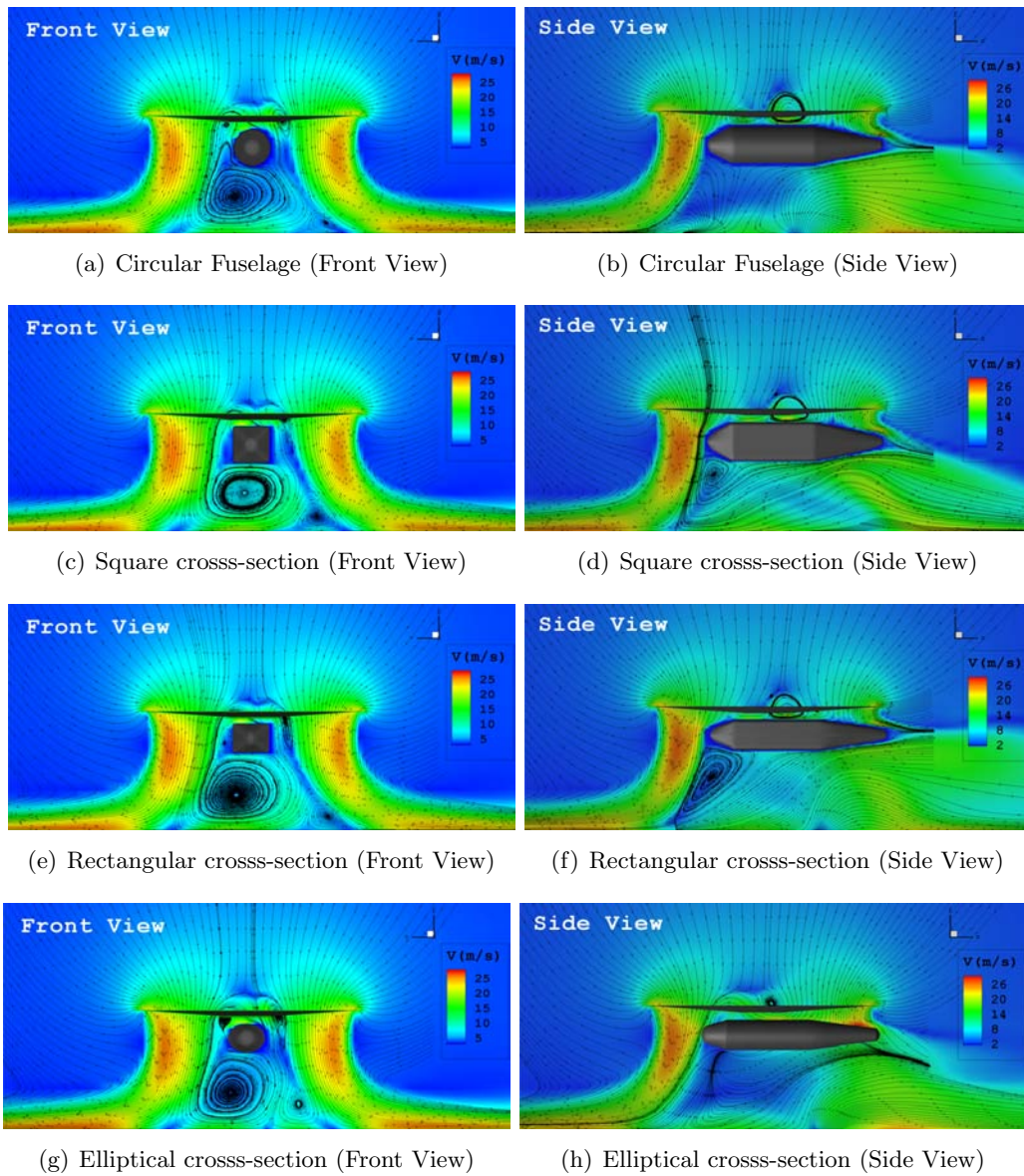


Figure 5.39 Velocity magnitude and streamlines for different fuselage shapes at $H = 1.0R$

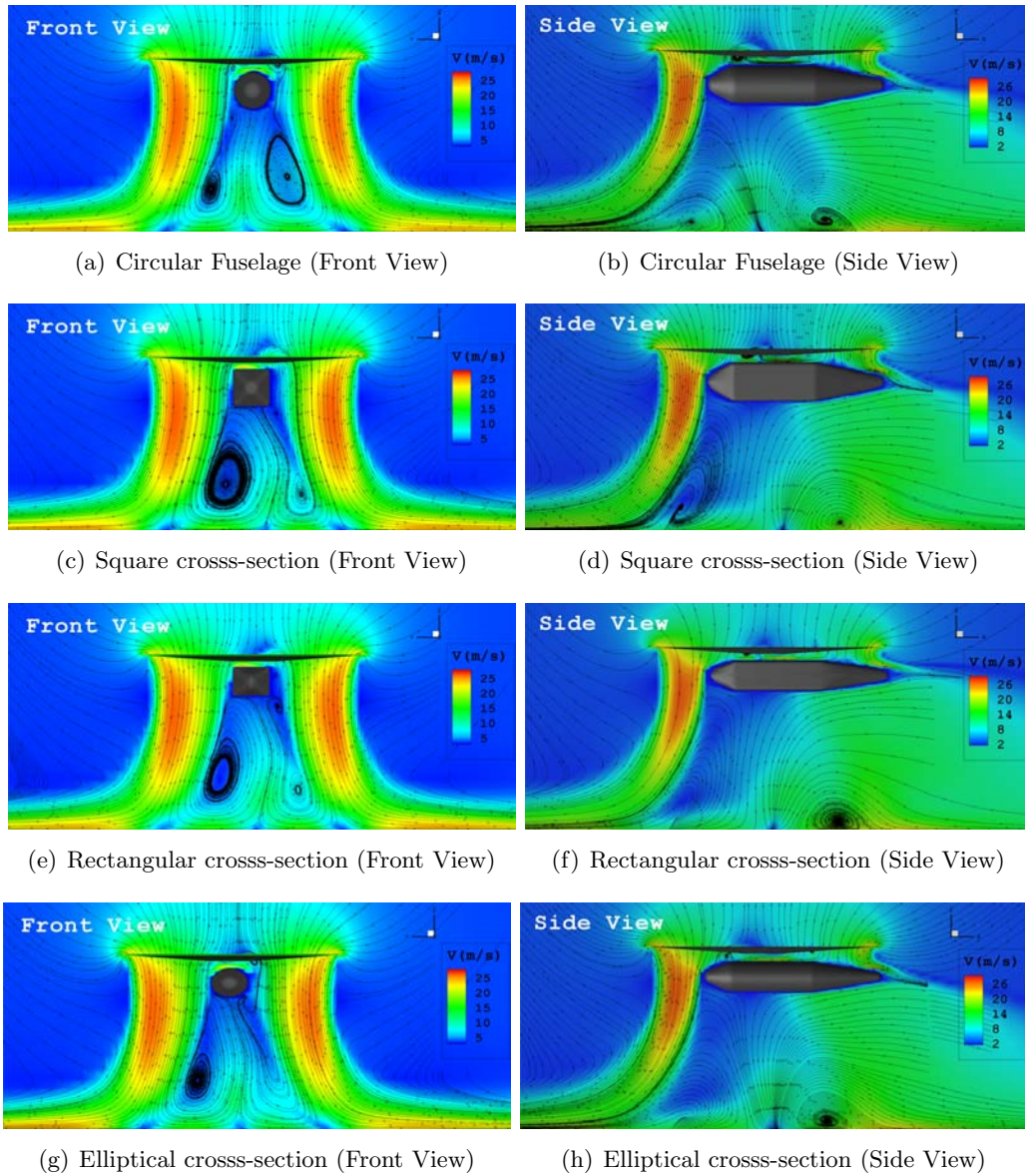


Figure 5.40 Velocity magnitude and streamlines for different fuselage shapes at $H = 1.5R$

5.6 Multi-Rotor Configuration Effect on Brownout

Full rotorcraft configurations with single rotor, tandem rotor, tilt rotor, and quad rotor have been used for this study (Figure 5.41). The rotor properties used are given in Table 5.3. *NACA0012* airfoil has been used for the rotor blades. The collective pitch of each rotor is adjusted so the C_T/σ for all the rotorcrafts are the same, while hovering at OGE (out of ground effect). The mechanism of calculating the collective pitch is the same as discussed in last section. σ is the solidity of the rotor given by $\sigma = N_b c/\pi R$, where N_b is the number of rotor blades and c is the rotor chord.

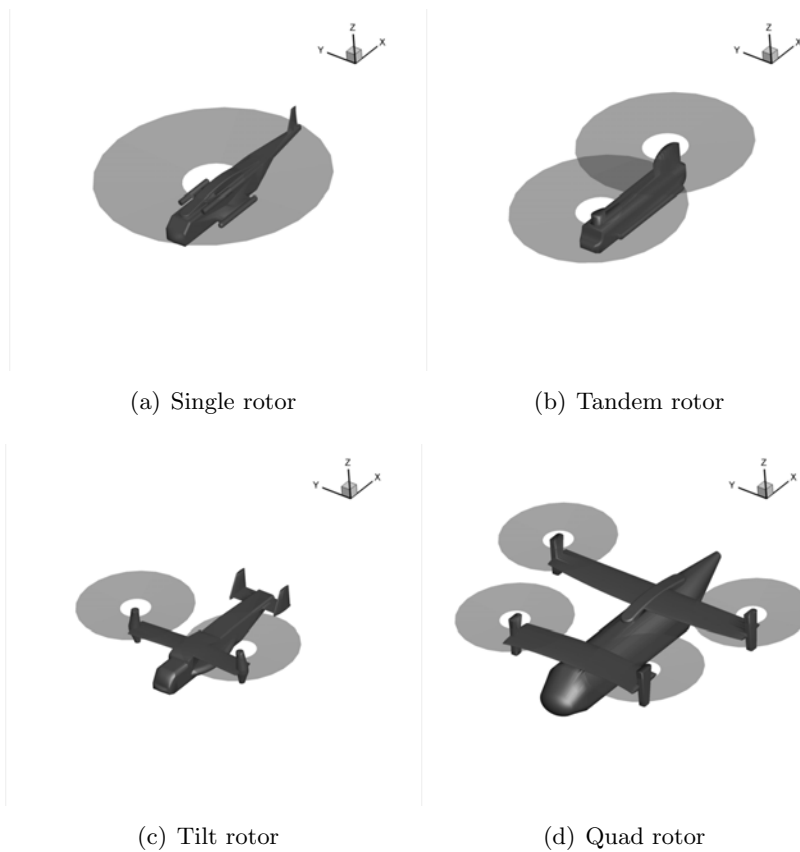


Figure 5.41 Rotor configurations

The simulation was carried out for four rotor heights $1.0, 1.5, 2.0,$ and $2.5R_{ref}$, where R_{ref} is the rotor radius of a single rotor helicopter. Corresponding non-dimensional heights (H/R) for the tandem rotor are $1.33, 2, 2.66,$ and 3.66 . For tilt and quad rotor, the non-dimensional

Table 5.3 Properties of rotor for multi-rotor configurations

	Rotor Radius	Rotor Blades (per rotor)	Twist	σ	C_T
Single rotor	12m	5	12°	0.095	0.0071
Tandem rotor	9m	3	12°	0.083	0.0063
Tilt rotor	6m	3	16°	0.105	0.0076
Quad rotor	6m	3	16°	0.105	0.0077

heights (H/R) are 2, 3, 4, and 5.

Velocity streamlines at three different lateral planes – front rotor mid plane, fuselage mid plane, and rear rotor mid plane – are plotted for tandem and quad rotors at various heights in Figures 5.42 and 5.46. The tilt rotor streamlines are plotted on lateral rotor mid plane in Figure 5.44. Streamlines along longitudinal plane are also plotted in Figures 5.43, 5.45, and 5.47.

In tandem rotor, large recirculating regions are observed underneath the fuselage at rotor heights of $H = 1.0, 1.5,$ and $2.0R_{ref}$. At fuselage mid plane, rotor wake are found to be shifted on the starboard side. This is due to the effect of mixing two counter rotating and swirling rotor downwashes. The rotor outwash and the wall-jet thickness in the longitudinal plane are determined to be similar to the single rotor configuration. The recirculating region near the ground at height $2.5R_{ref}$ has diminished.

Similar to tandem rotor, tilt and quad rotor configurations show a heavy recirculating zone below the fuselage at a height of 1.0, 1.5, and $2.0R_{ref}$. In particular, the region below the fuselage wings is found highly unsteady. One of the major differences between tilt and quad rotor with respect to tandem rotor is the rotor outwash and wall jet thickness along the longitudinal plane. At lower altitudes, the outwash and the wall jet of tilt and quad rotor are found thicker compared to tandem and single rotor. This plays a very important role in dust particle transport in front of the fuselage.

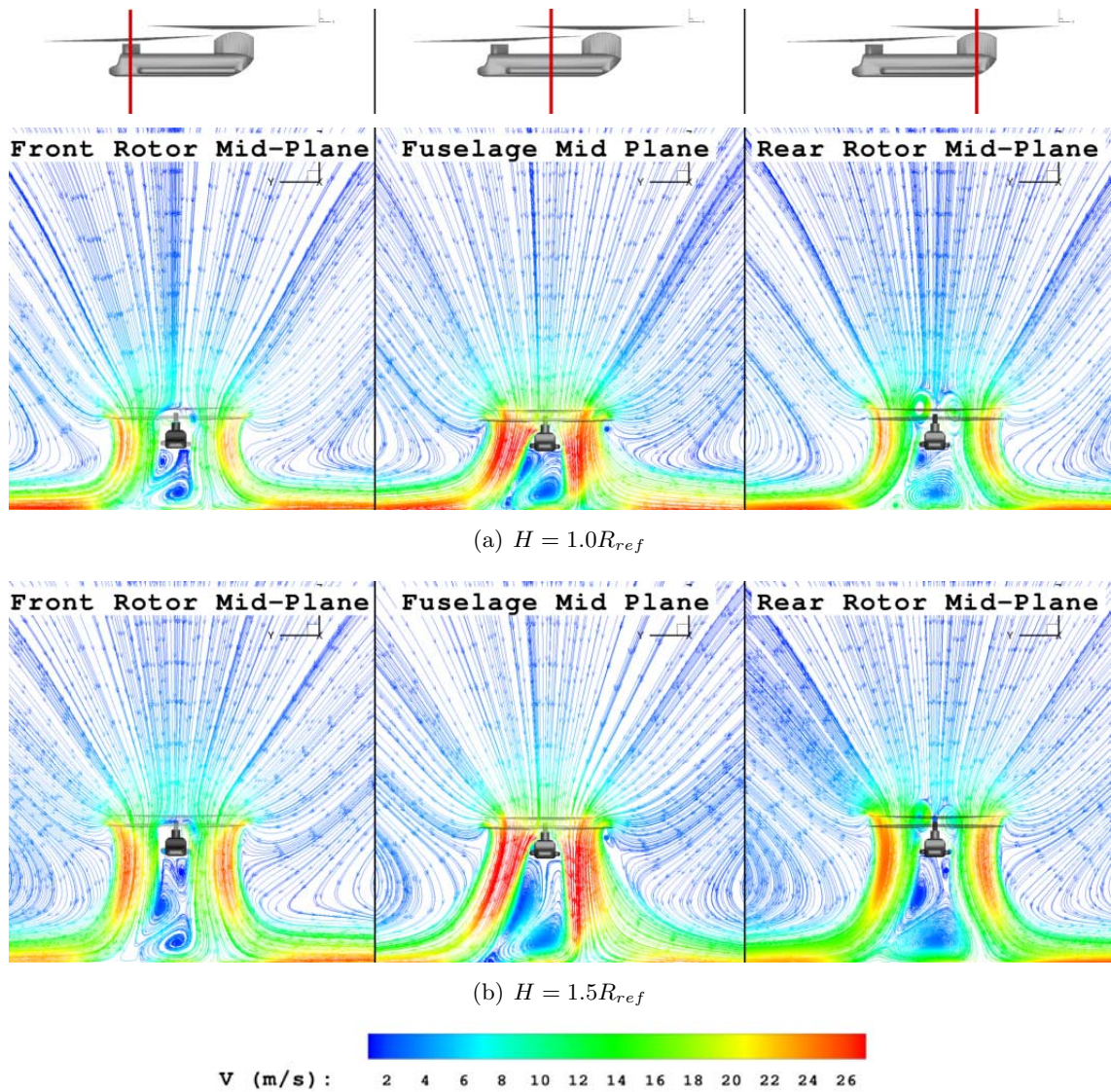


Figure 5.42 Streamlines in lateral plane for tandem rotor hovering at different heights

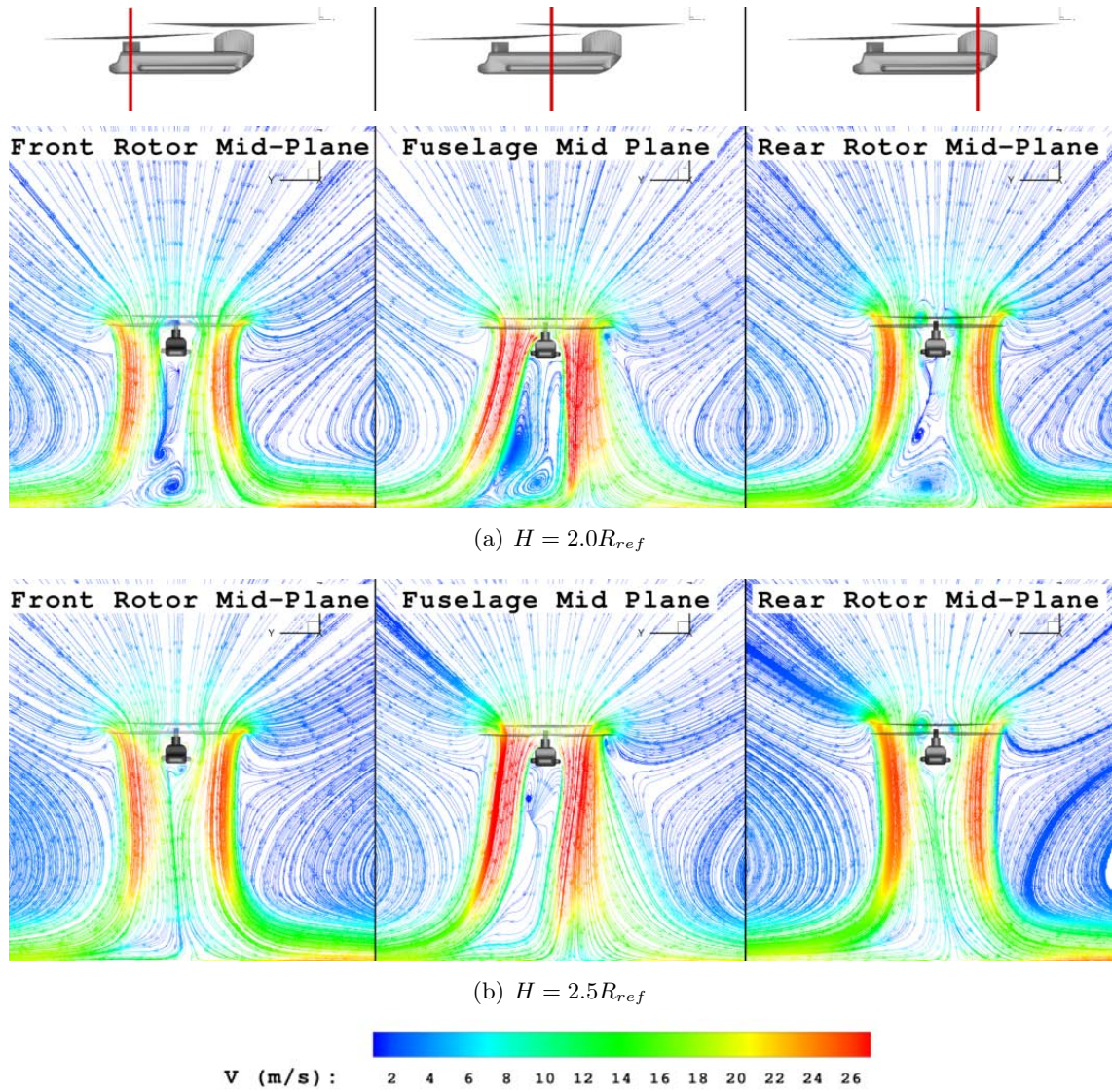


Figure 5.42 (continued) Streamlines in lateral plane for tandem rotor hovering at different heights

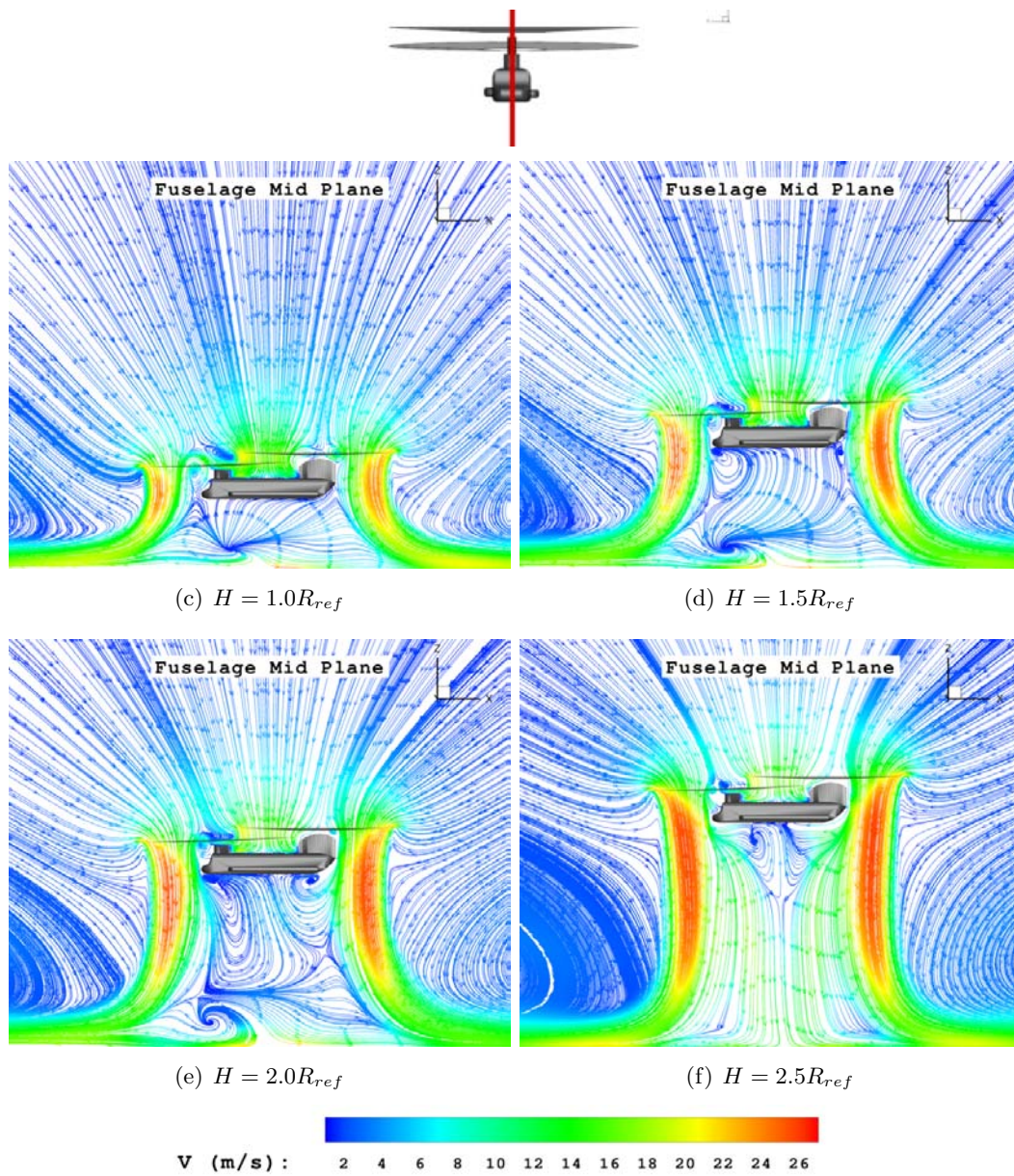


Figure 5.43 Streamlines in longitudinal plane for tandem rotor hovering at different heights

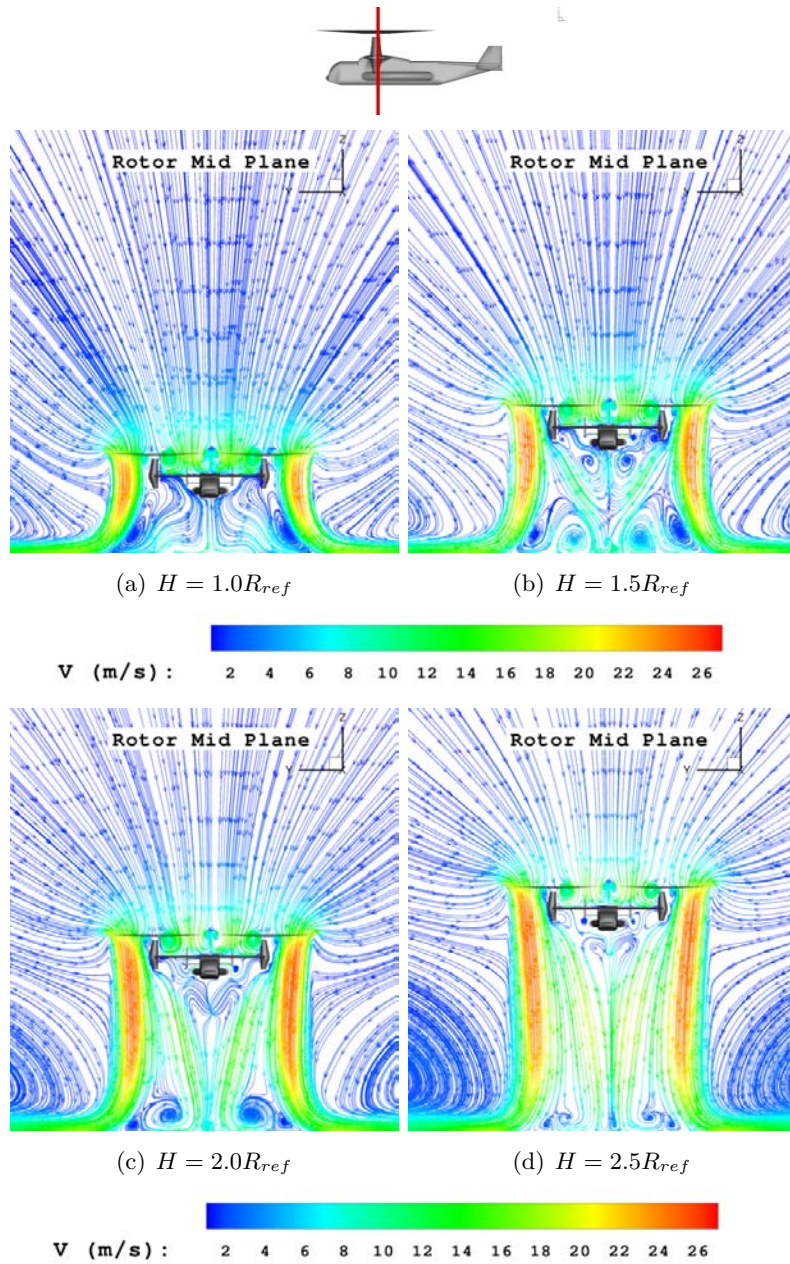


Figure 5.44 Streamlines in lateral plane for tilt rotor hovering at different heights

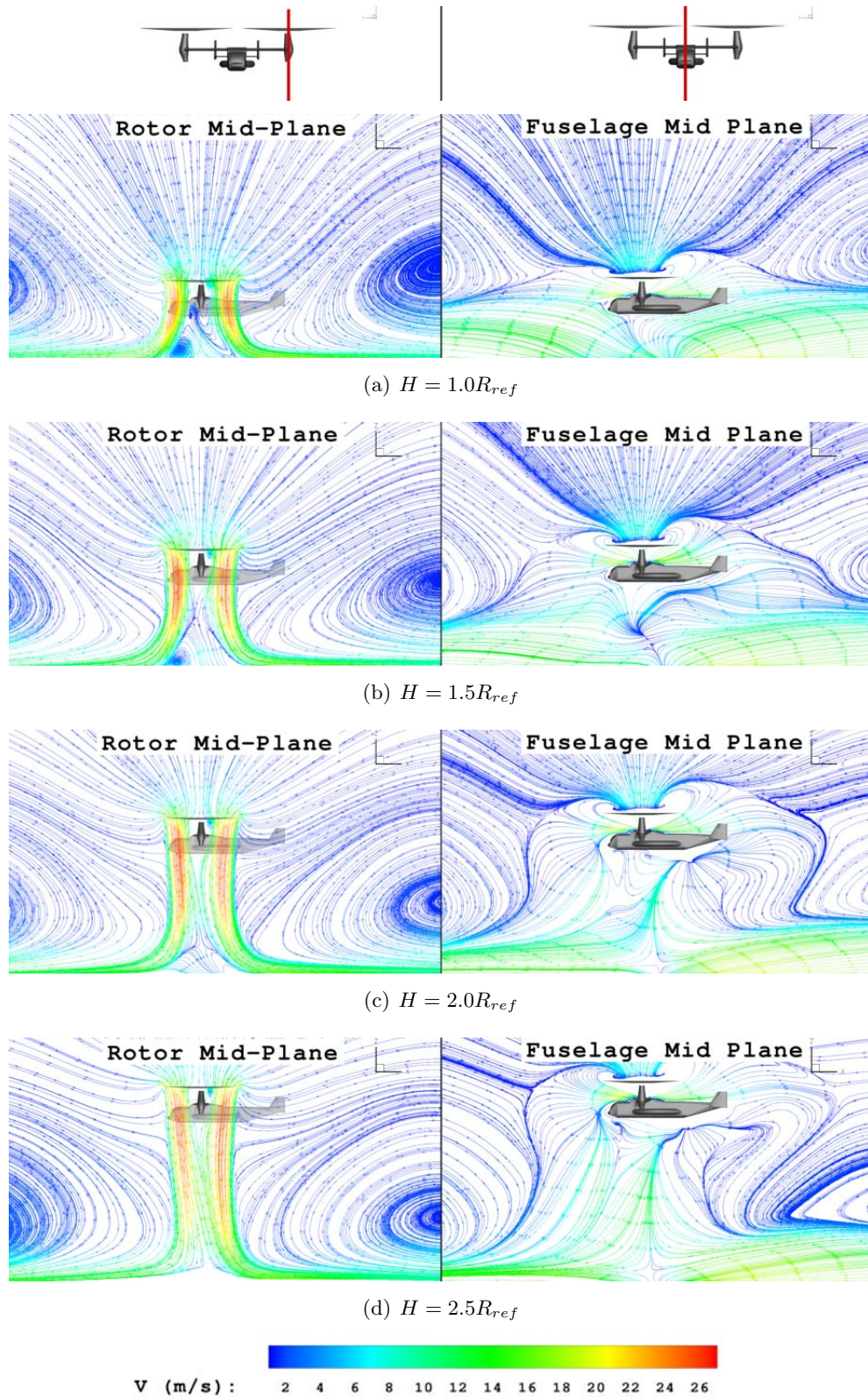


Figure 5.45 Streamlines in longitudinal plane for tilt rotor hovering at different heights

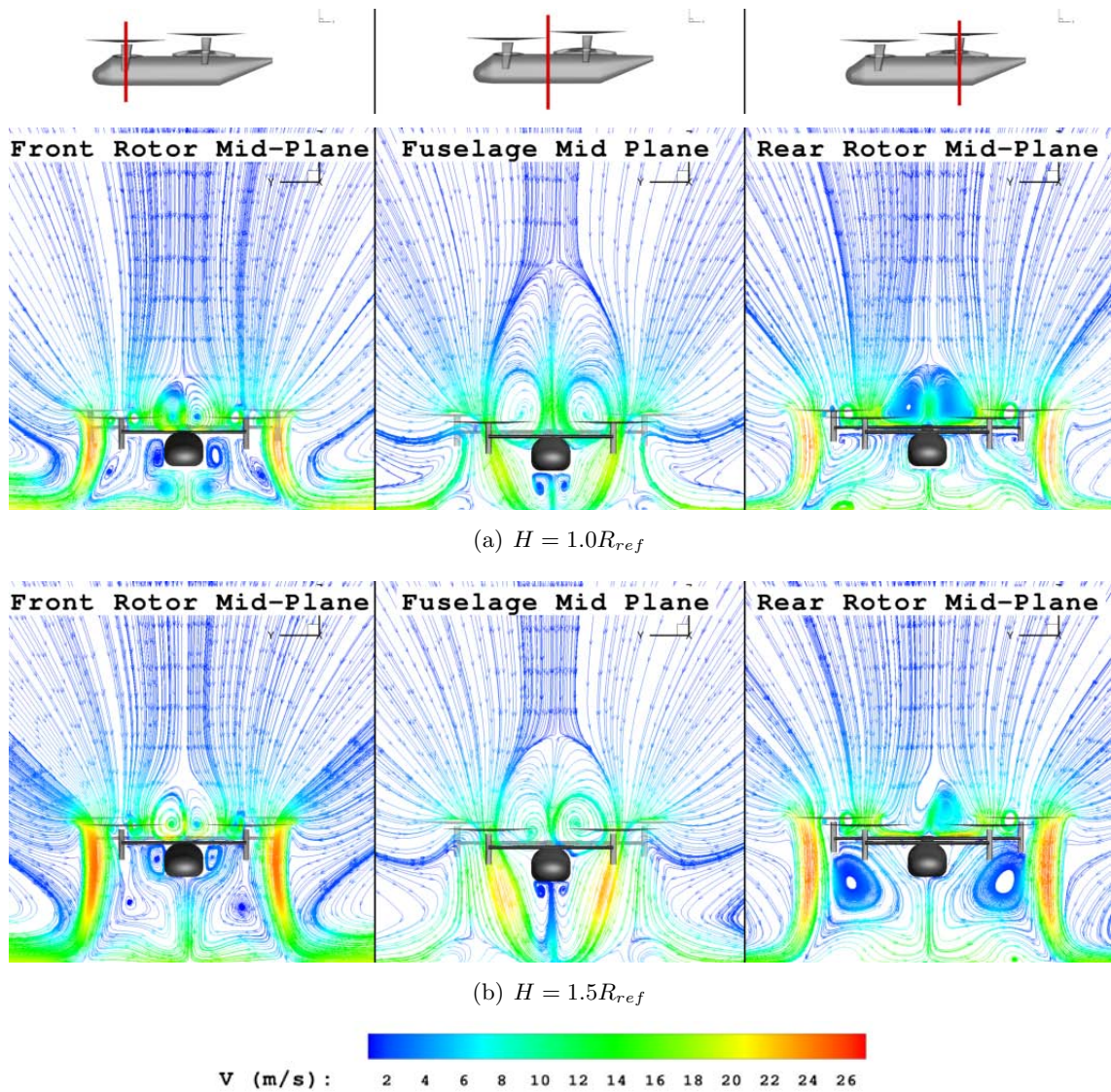


Figure 5.46 Streamlines in lateral planes for quad rotor hovering at different heights

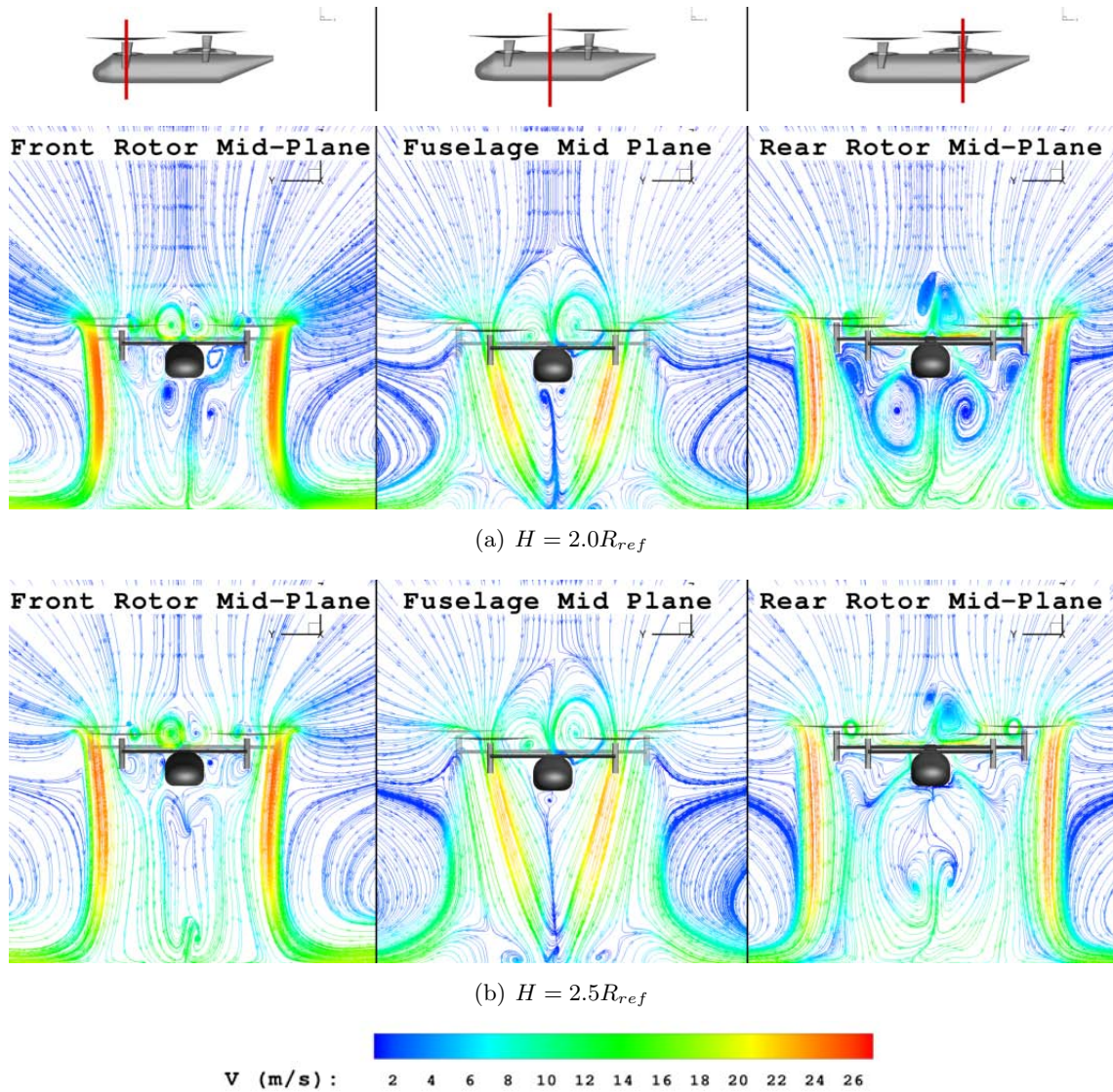


Figure 5.46 (Continued) Streamlines in lateral planes for quad rotor hovering at different heights

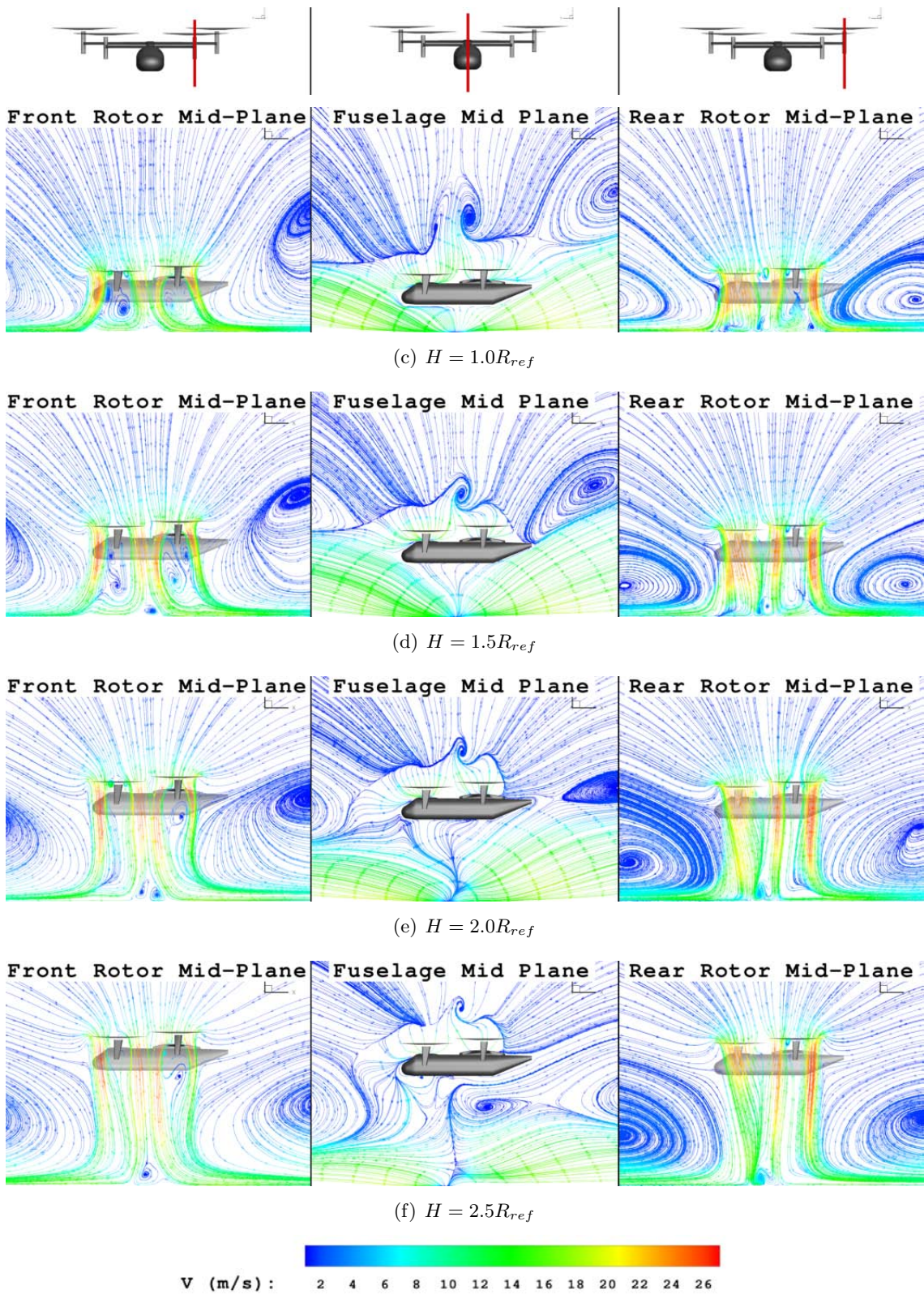
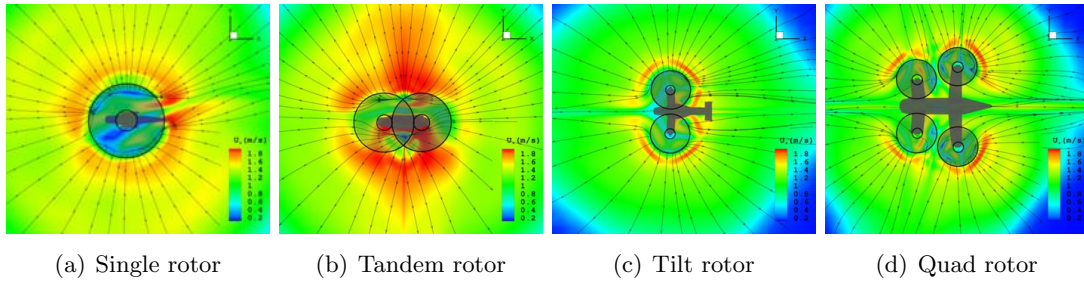
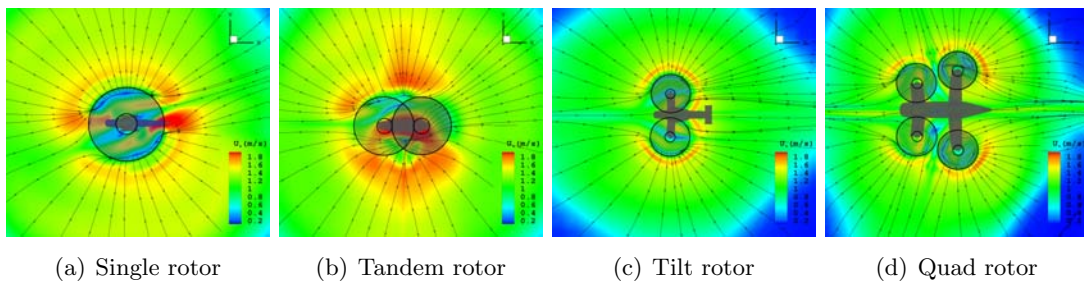
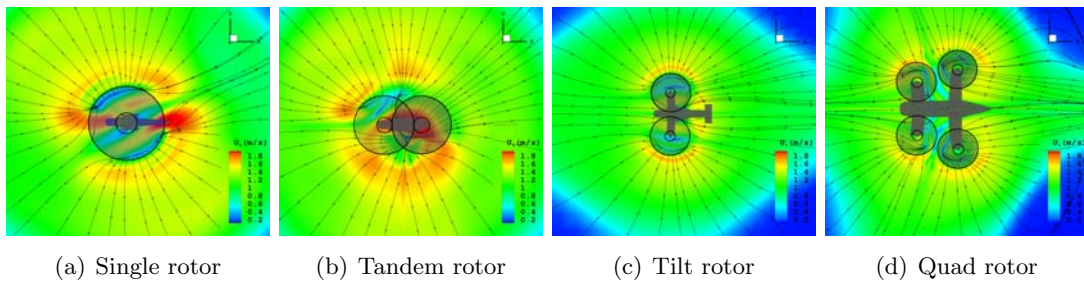
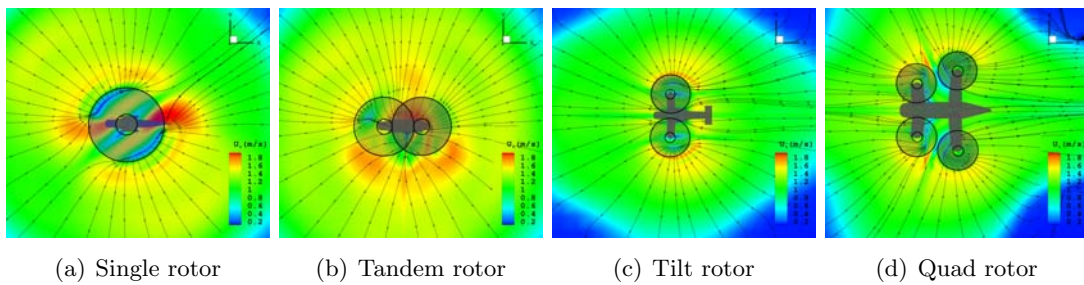


Figure 5.47 Streamlines on longitudinal plane for quad rotor hovering at different heights

To compare the dust erosion capability of different rotor configurations, the ground signature of each configuration at different heights is plotted in Figures 5.48 to 5.51. A significant difference of ground friction velocity has been found between single and tandem rotor with respect to tilt and quad rotors at the same dimensional height. In particular, tandem rotor is determined to give strong ground signature for all heights. Even at the same non-dimensional height (H/R) of 2.0, (comparing Figures 5.50(a), 5.49(b), 5.48(c), and 5.48(d)), the tandem rotor has the most intense ground friction.

Dust clouds (iso-surface of $50mg/m^3$) after simulation time of 5s for different rotor configurations at different heights are shown in Figures 5.52 to 5.55. At all heights the spread of the dust cloud is more for the single and tandem rotors. Dust characteristics along the rotorcraft's lateral plane is visualized by removing the dust cloud on the rear side of the fuselage mid lateral plane. Dust characteristic seen through fuselage's center lateral plane (front view) are shown in Figures 5.56 to 5.59, where the x-axis is normal to the images. Similarly, for dust characteristics along the longitudinal plane (side view), the dust cloud is removed from the port side of the fuselage's longitudinal plane (x-z plane) and seen through this plane in Figures 5.60 to 5.63, where the y-axis is normal to the plane. Although in all scenarios single and tandem rotor form more denser clouds, in terms of front visual reference, these two are determined as better. As seen in the front view at heights 1.0 and $1.5R_{ref}$, huge dust clouds form in front of the tilt and quad rotor, thus restricting the pilot's front visibility. This is mainly caused by transport of dust particles by stronger and thicker rotor outwash in front of the fuselage in tilt and quad rotor configuration. In terms of side view perspective, tilt and quad rotor are determined as better. There is an unusually huge dust cloud on the starboard side of the tandem rotor at greater heights. This is caused by dust carried by the shifted rotor downwash on the starboard side as discussed earlier.

Another interesting phenomenon observed is the dust fountain just below the fuselage tilt and quad rotor is not as intense as compared to single and tandem rotors. This might be due to a smaller rotor in tilt and quad rotors, thus, smaller downwash area hitting the ground as shown in the ground signature.

Figure 5.48 Ground friction velocity comparison at $H = 1.0R_{ref}$ Figure 5.49 Ground friction velocity comparison at $H = 1.5R_{ref}$ Figure 5.50 Ground friction velocity comparison at $H = 2.0R_{ref}$ Figure 5.51 Ground friction velocity comparison at $H = 2.5R_{ref}$

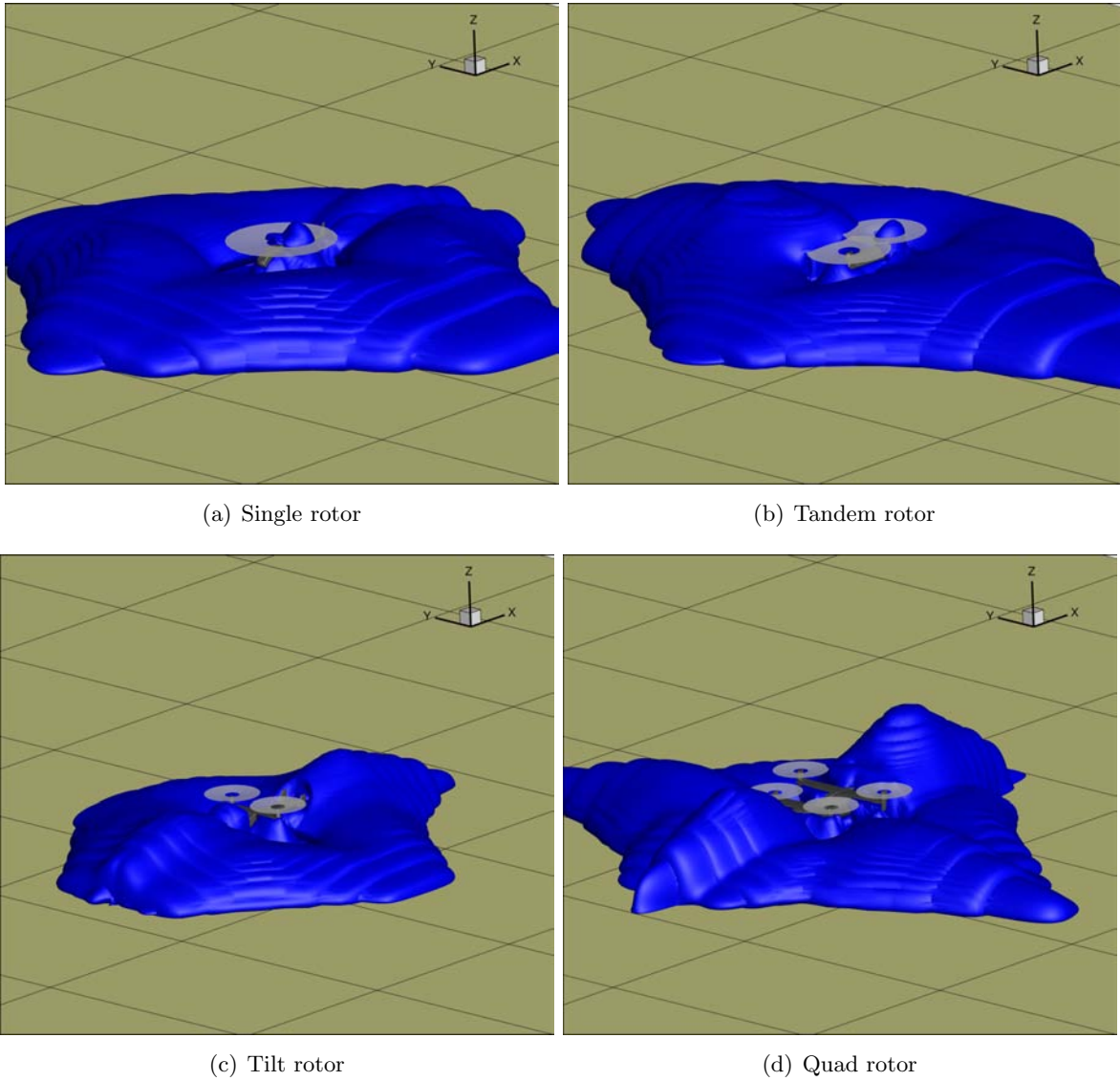


Figure 5.52 Dust cloud comparison for multiple rotor configurations at $H = 1.0R_{ref}$

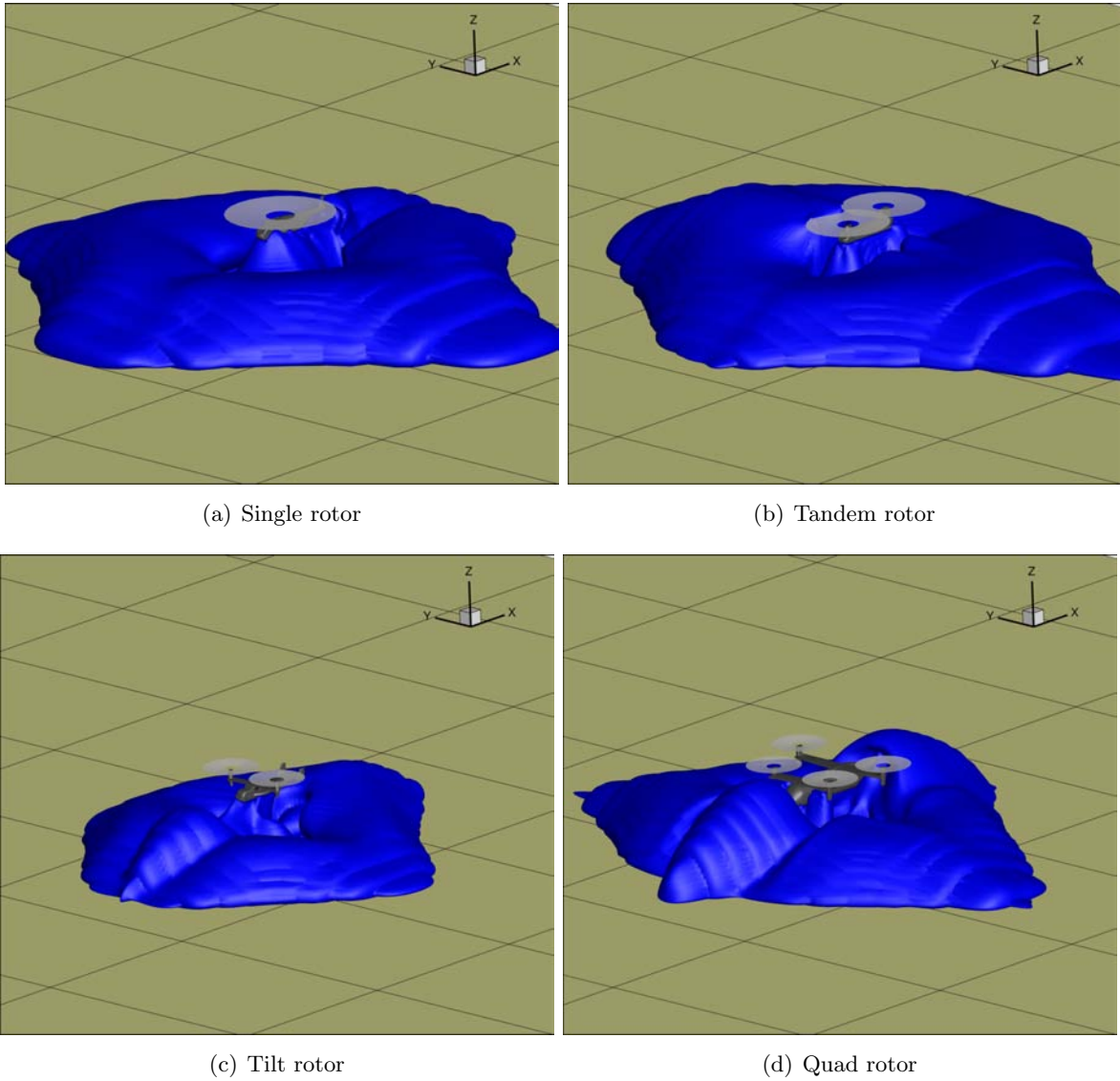


Figure 5.53 Dust cloud comparison for multiple rotor configurations at $H = 1.5R_{ref}$

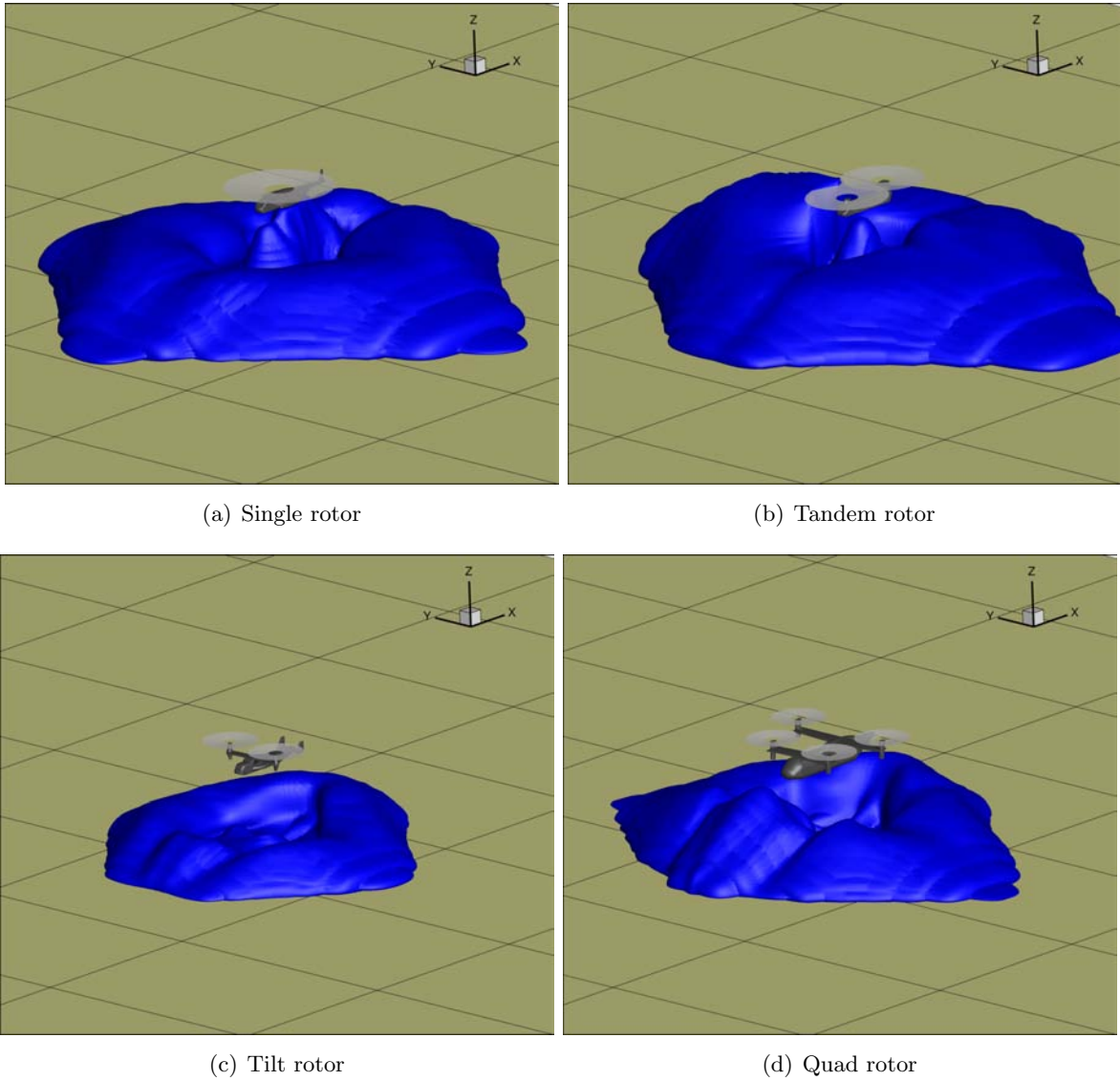


Figure 5.54 Dust cloud comparison for multiple rotor configurations at $H = 2.0R_{ref}$

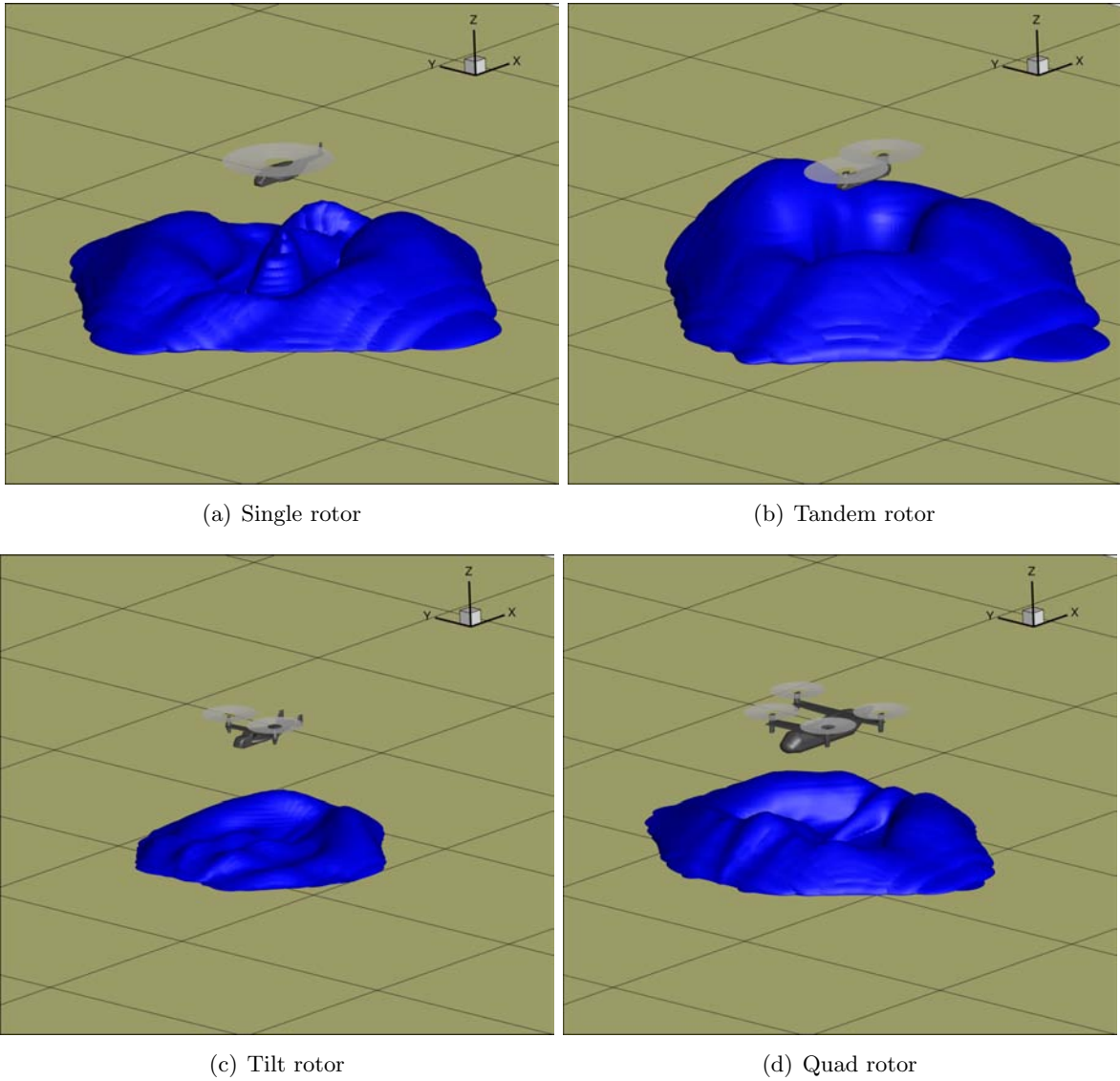


Figure 5.55 Dust cloud comparison for multiple rotor configurations at $H = 2.5R_{ref}$

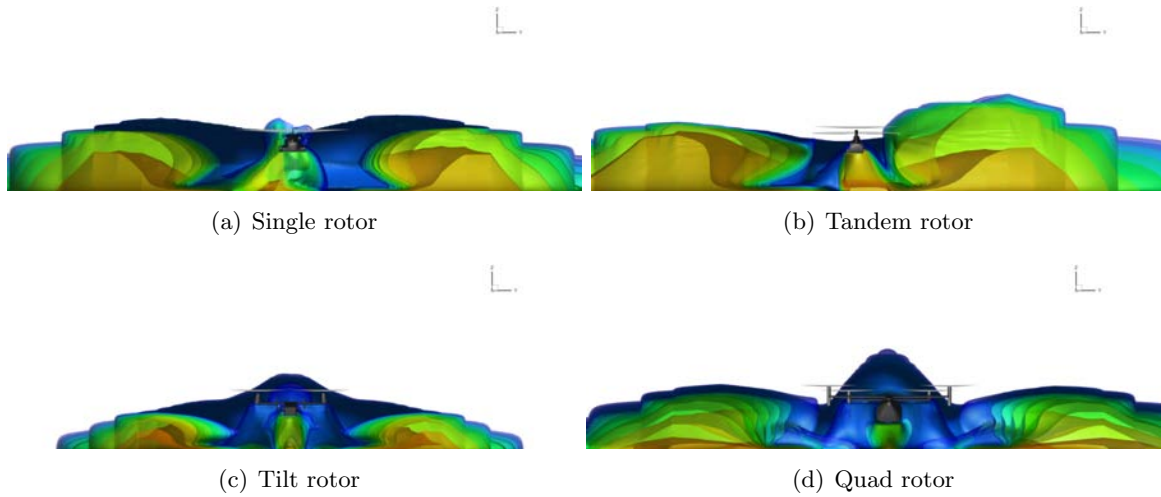


Figure 5.56 Dust cloud characteristics through fuselage lateral mid plane at $H = 1.0R_{ref}$

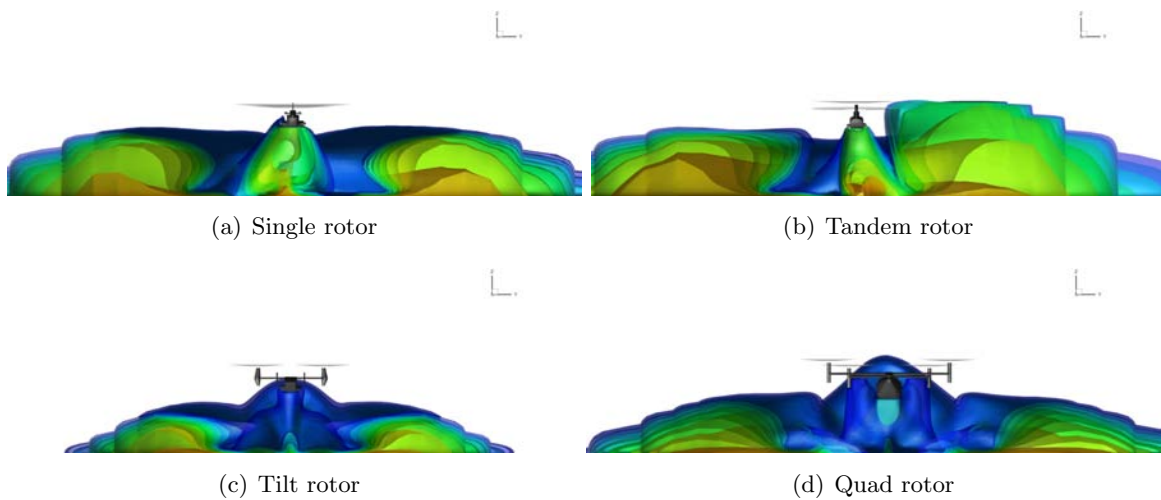


Figure 5.57 Dust cloud characteristics through fuselage lateral mid plane at $H = 1.5R_{ref}$

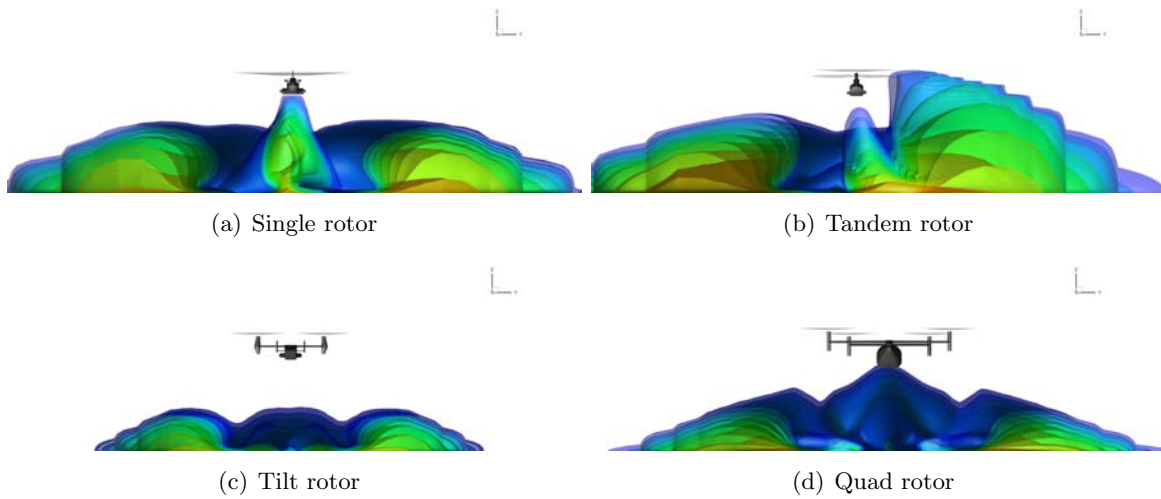


Figure 5.58 Dust cloud characteristics through fuselage lateral mid plane at $H = 2.0R_{ref}$

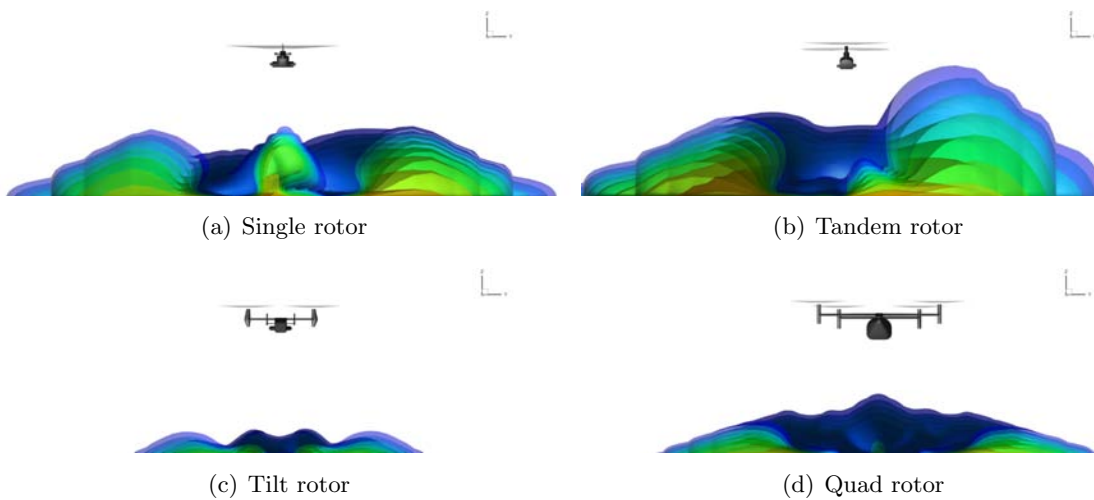


Figure 5.59 Dust cloud characteristics through fuselage lateral mid plane at $H = 2.5R_{ref}$

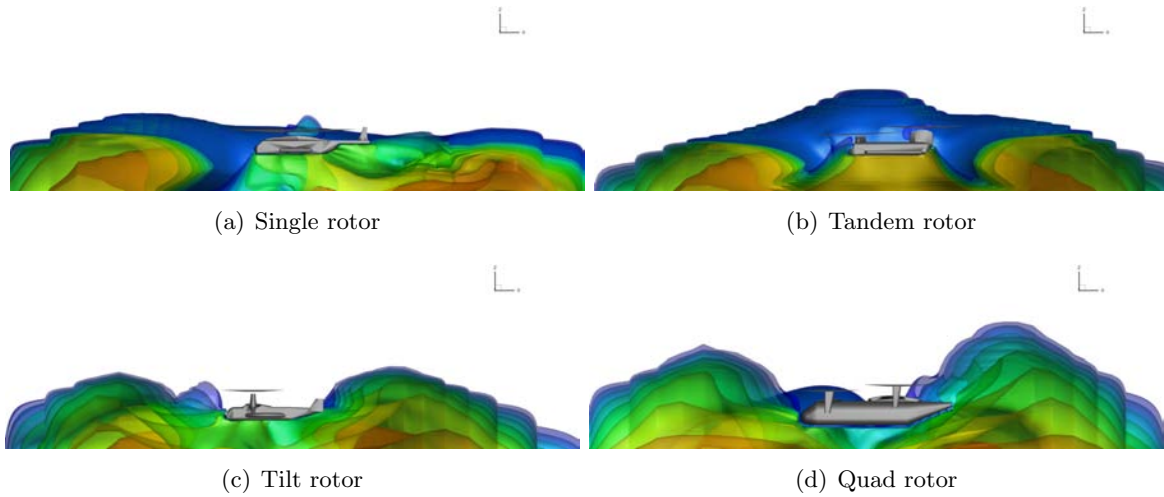


Figure 5.60 Dust cloud characteristics through fuselage longitudinal mid plane at $H = 1.0R_{ref}$

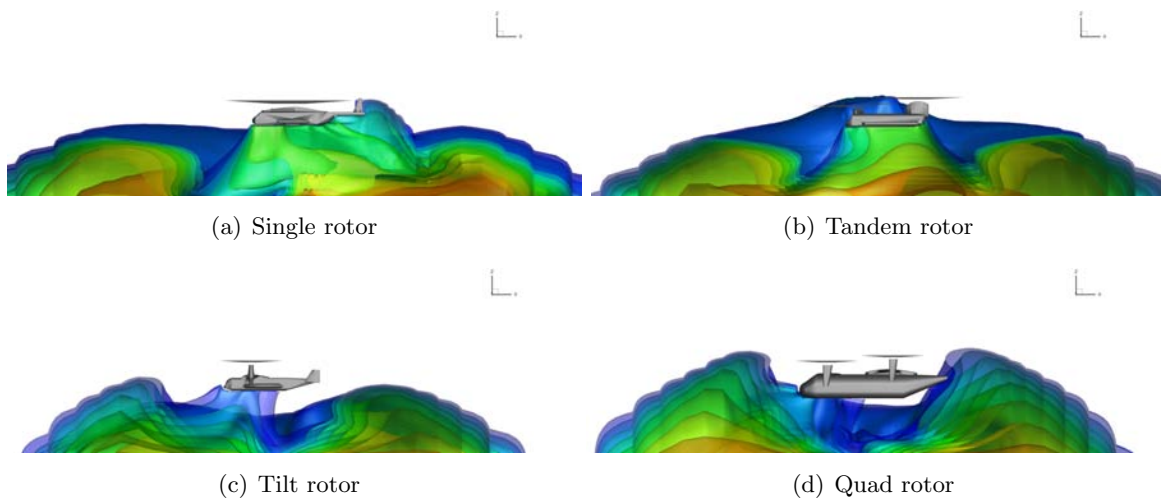


Figure 5.61 Dust cloud characteristics through fuselage longitudinal mid plane at $H = 1.5R_{ref}$

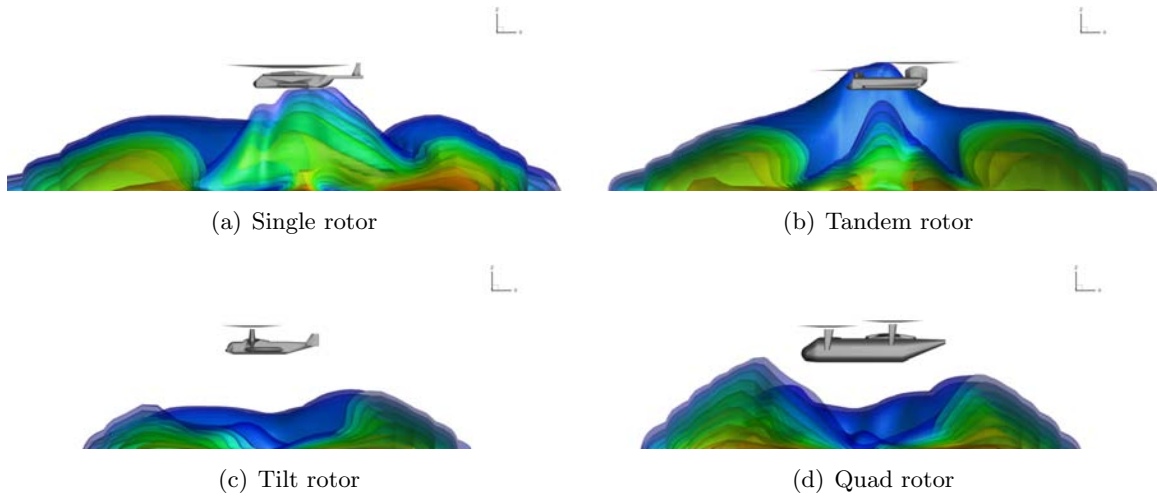


Figure 5.62 Dust cloud characteristics through fuselage longitudinal mid plane at $H = 2.0R_{ref}$

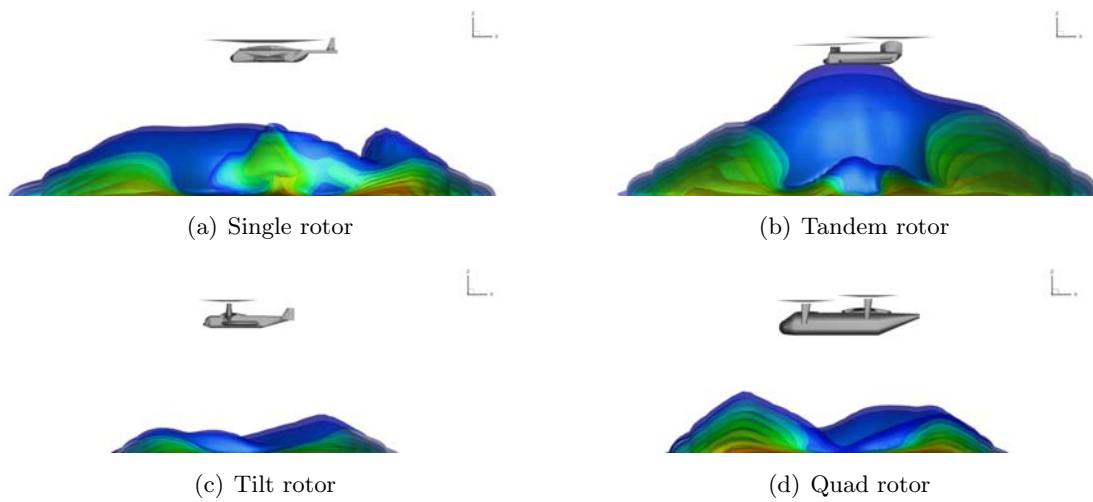


Figure 5.63 Dust cloud characteristics through fuselage longitudinal mid plane at $H = 2.5R_{ref}$

Time evolution of dust for all configurations at height $1.0R_{ref}$ is shown in Figures 5.64 - 5.68. After 2 s, the dust cloud height formed by tandem rotor is significantly higher than for other configurations. It can be clearly seen that the major dust entrainment is from the starboard side of the tandem rotors. After 3 s, all configurations show considerable size of dust cloud formation. Single rotor shows dust formation all along the perimeter of the rotor. Some effects of the fuselage tail are also found in the rear zone. The tandem rotor also shows dust formation from all sides, but dust cloud heights are larger on the lateral sides. Dust cloud size in the tilt rotor are comparatively small with a major evolution of dust coming from front and rear. The quad rotor also shows similar trends with significant dust evolution from the sides as well. After 5 s, all the configurations are almost engulfed in the dust cloud and there is no visual reference for pilots. The single rotor still has some near rotor visual reference. After 10 s, all rotorcraft are engulfed in the cloud, without any visual reference. The dust cloud is almost axisymmetric for a single rotor. In the tandem rotor, a huge dust cloud is seen on the starboard side; whereas, for tilt and quad rotors, it is seen in the front and rear.

Comparison of fuselage effect on multi rotor configurations is shown in Figures 5.69 - 5.71. Plots are shown for ground friction and dust clouds for multi-rotor configurations, with and without fuselage, hovering at $1.0R_{ref}$. Similar to the helicopter, there is a significant effect of fuselage on ground signature. The strength of ground friction velocity is found higher in the case with fuselage for all configurations. Average height of the dust for rotor and rotor-fuselage configurations are found to be almost the same, but the dust cloud density for the fuselage rotor configurations are higher.

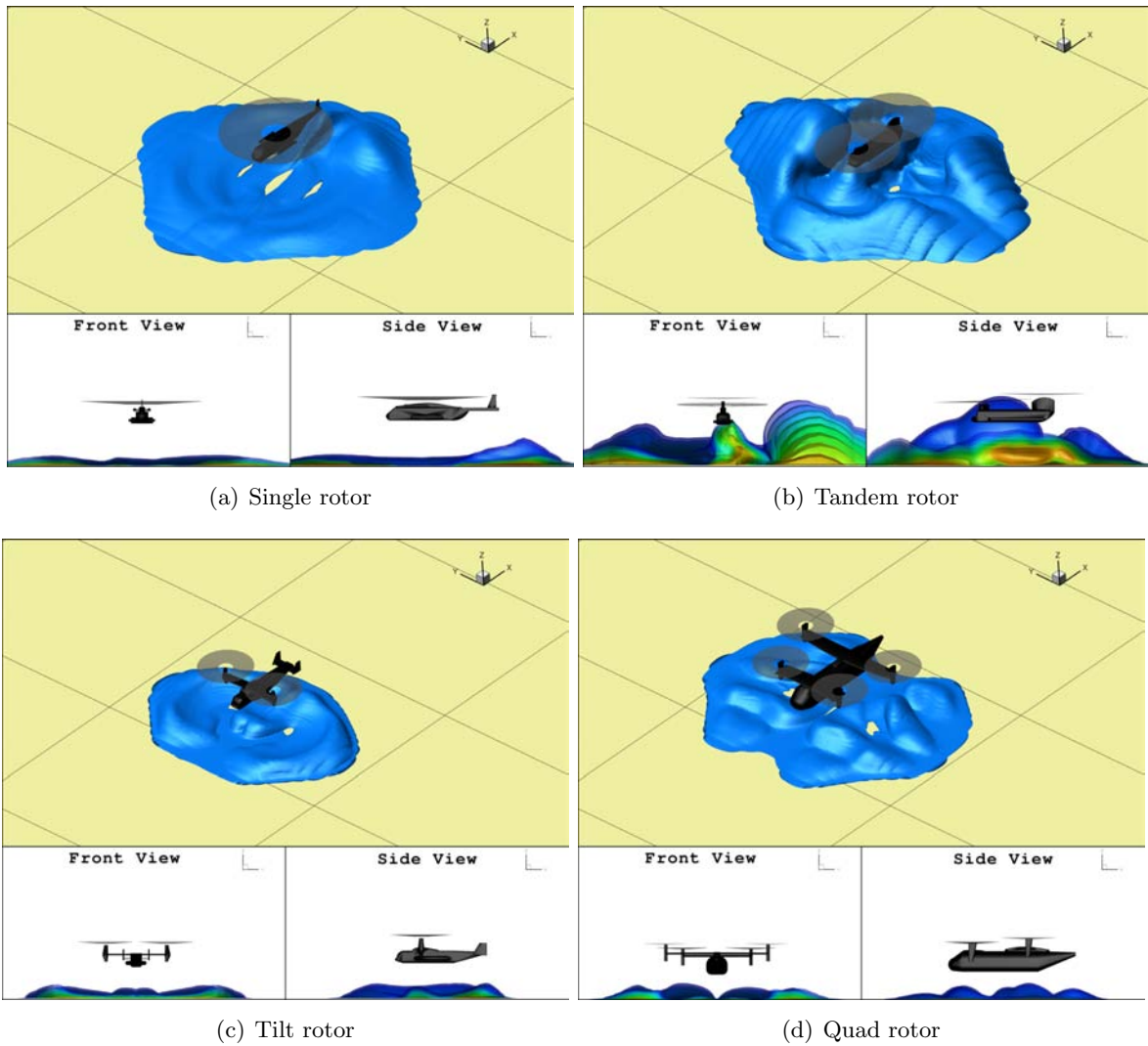


Figure 5.64 Dust cloud evolution after 2s at $H = 1.0R_{ref}$

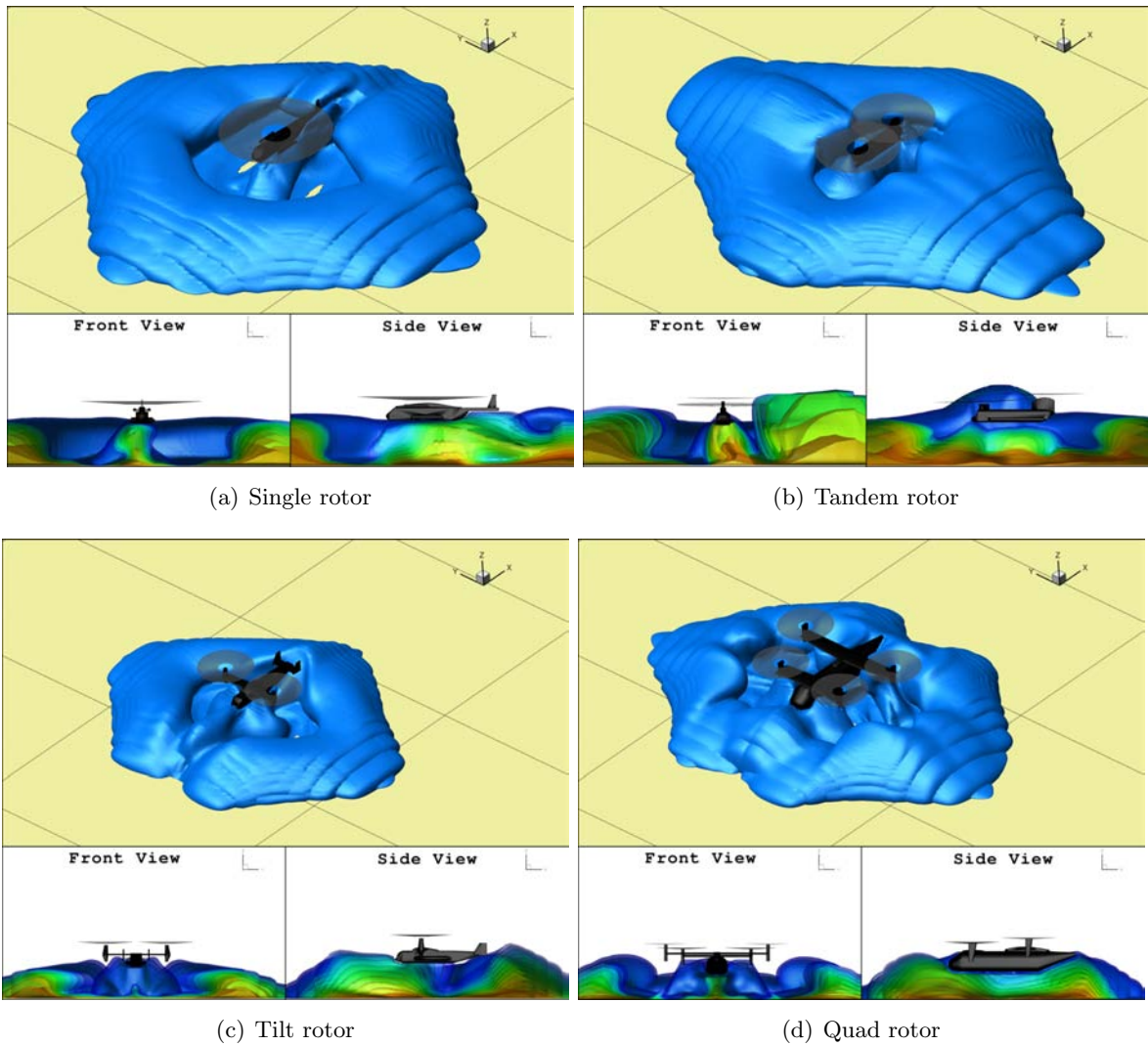


Figure 5.65 Dust cloud evolution after $3s$ at $H = 1.0R_{ref}$

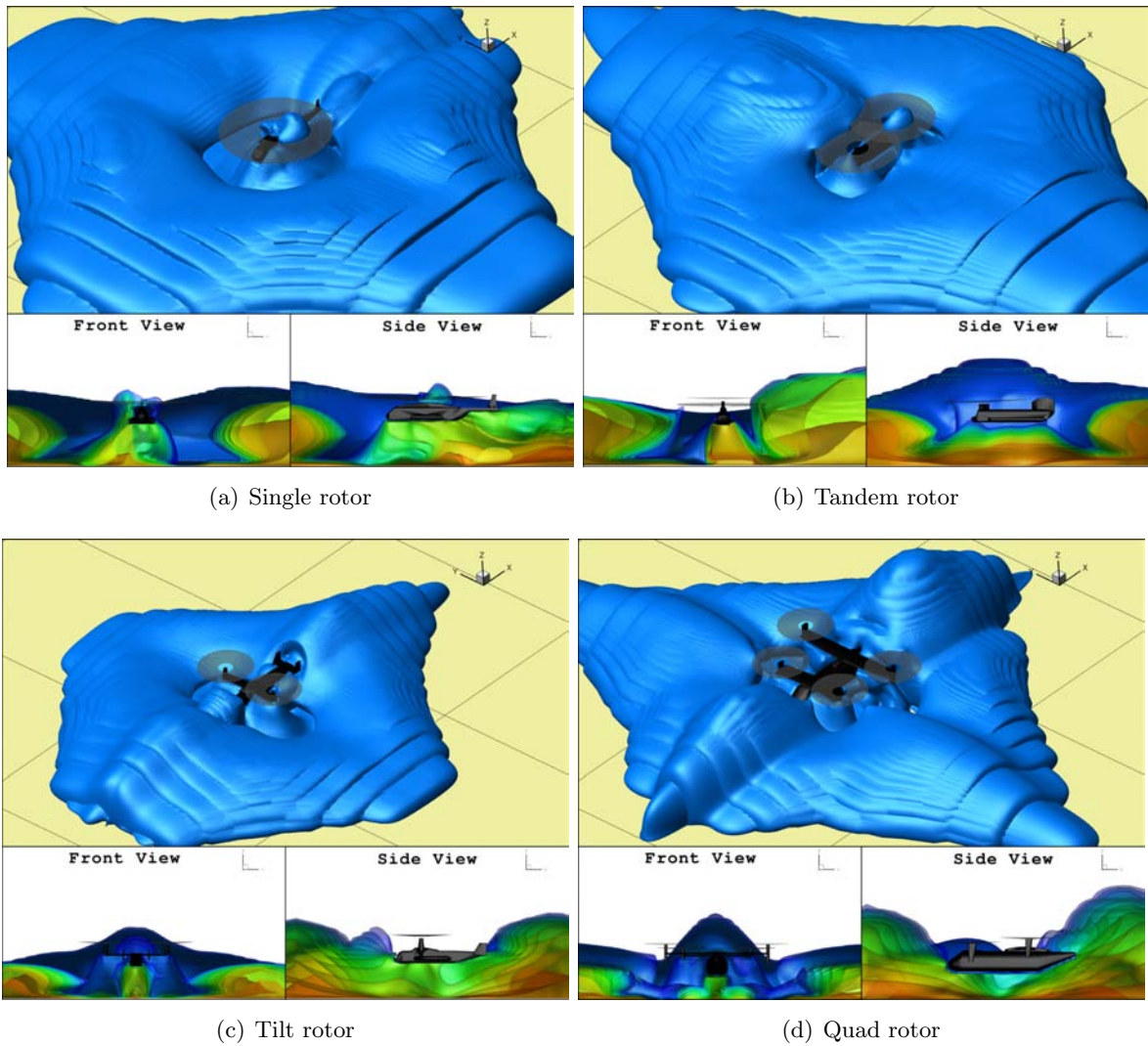


Figure 5.66 Dust cloud evolution after $5s$ at $H = 1.0R_{ref}$

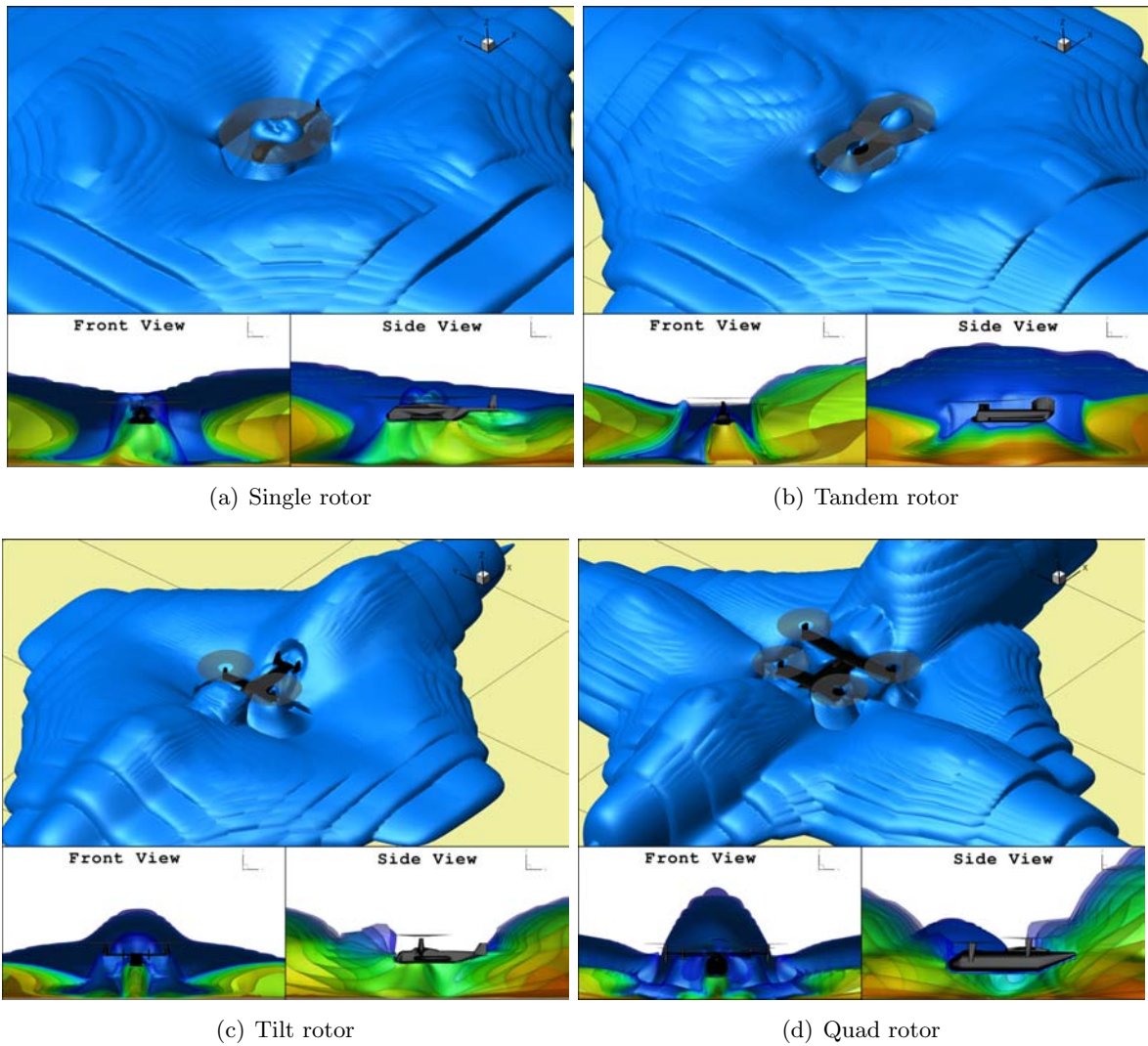


Figure 5.67 Dust cloud evolution after $7s$ at $H = 1.0R_{ref}$

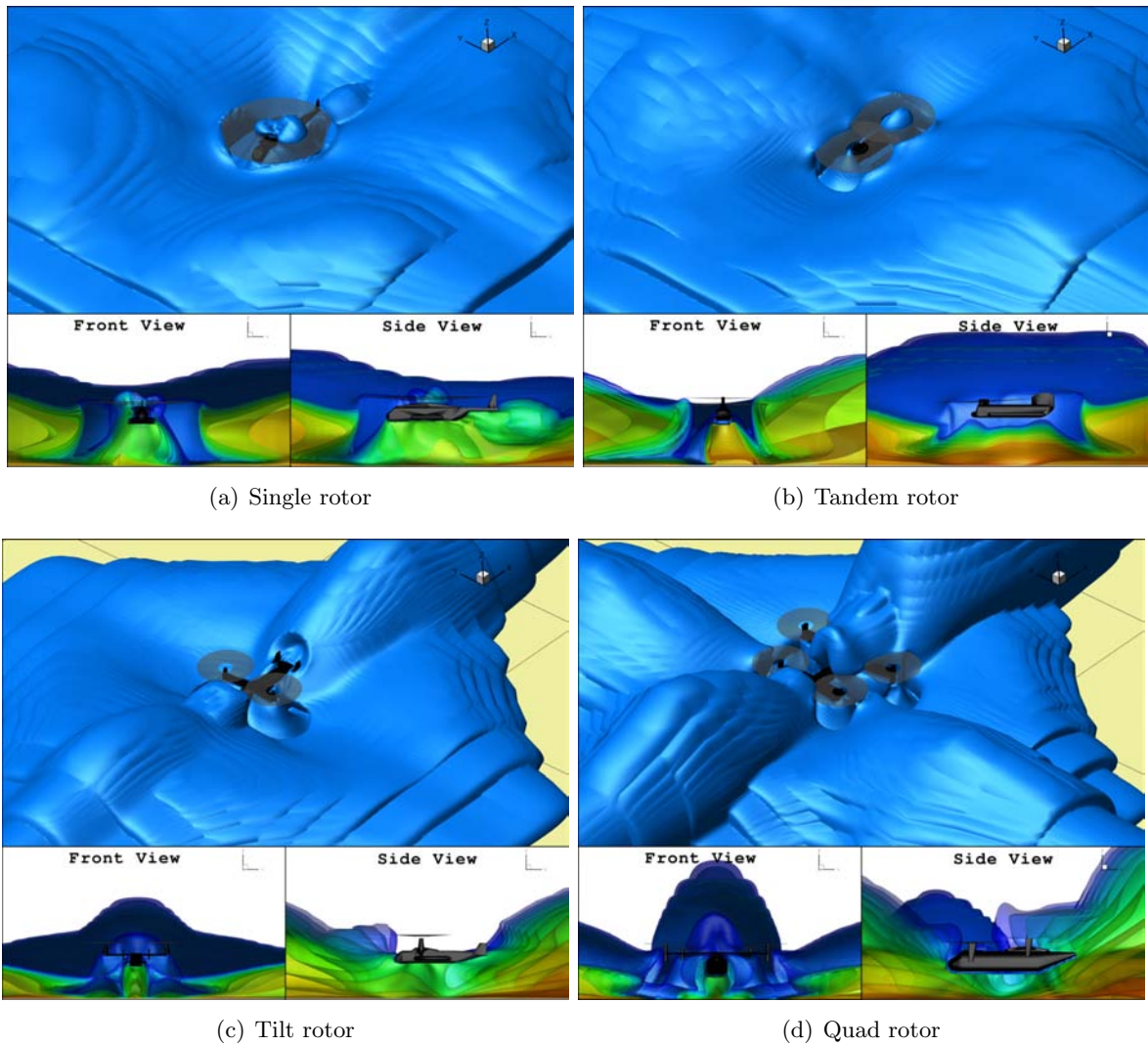
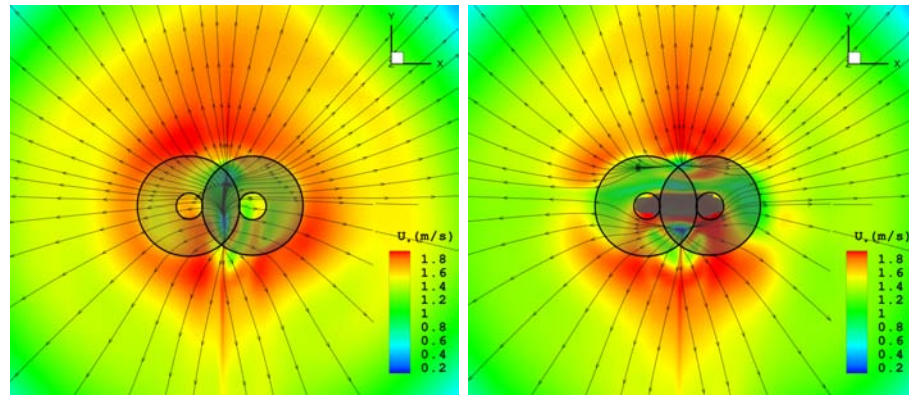
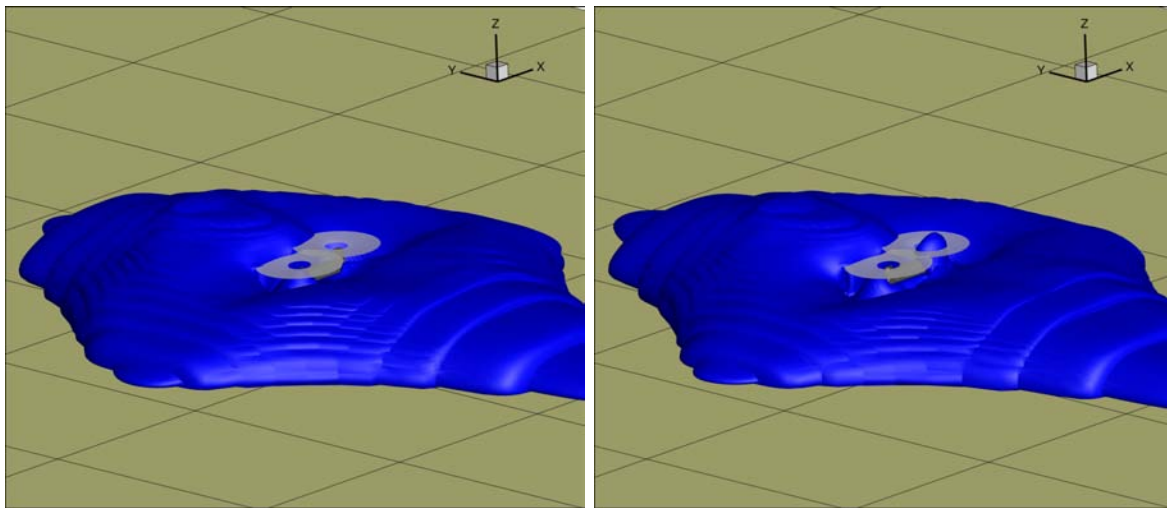


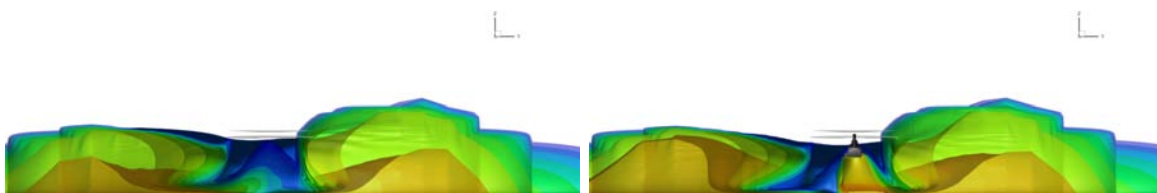
Figure 5.68 Dust cloud evolution after 10s at $H = 1.0R_{ref}$



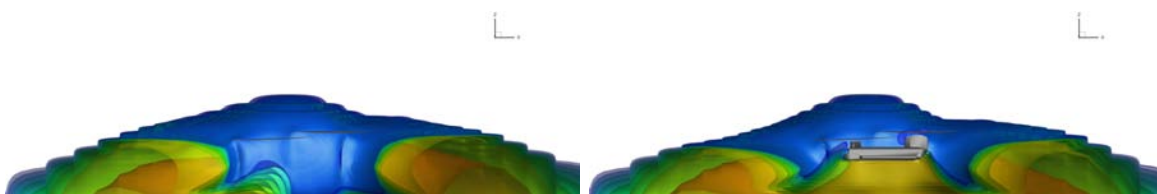
(a) Ground friction velocity for tandem rotors only (b) Ground friction velocity for tandem rotors with fuselage



(c) Tandem rotors only (dust cloud) (d) Tandem rotors with fuselage (dust cloud)

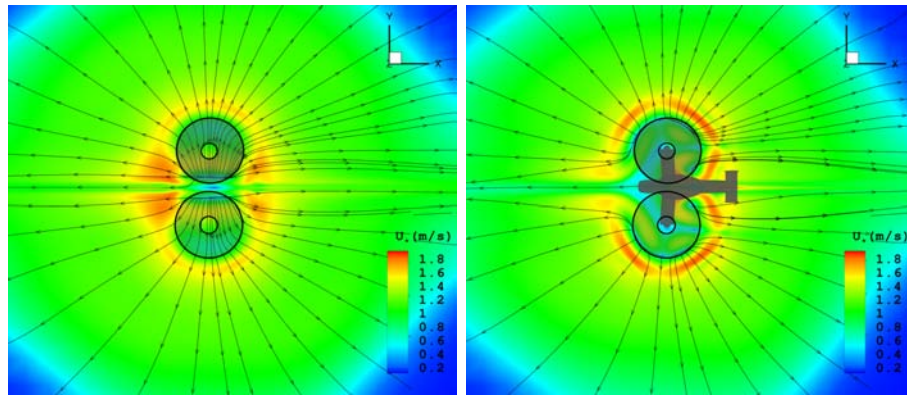


(e) Tandem rotors only (Pilot's front view) (f) Tandem rotors with fuselage (Pilot's front view)

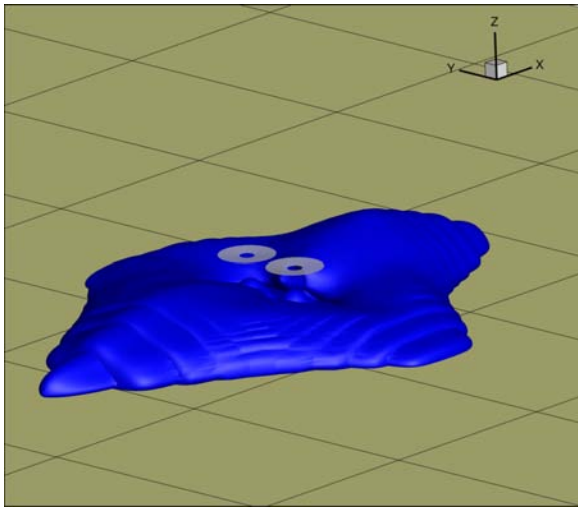


(g) Tandem rotors only (Pilot's side view) (h) Tandem rotors with fuselage (Pilot's side view)

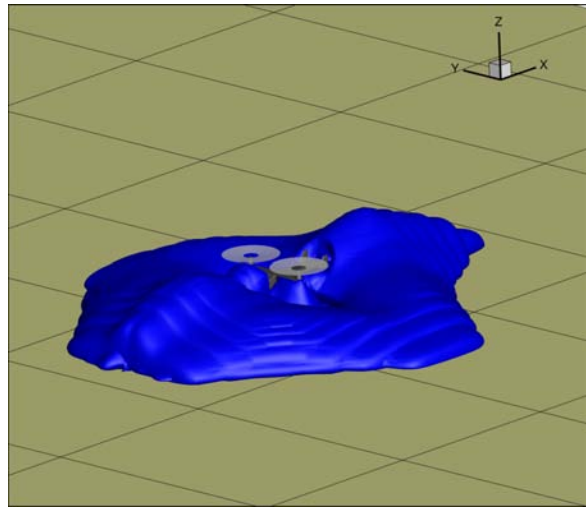
Figure 5.69 Comparison of tandem rotors with and without fuselage at $H = 1.0R_{ref}$



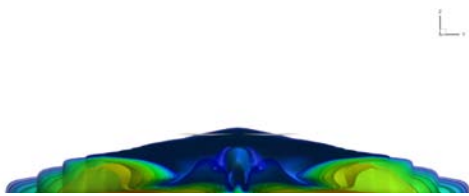
(a) Ground friction velocity for tandem rotors only (b) Ground friction velocity for tandem rotors with fuselage



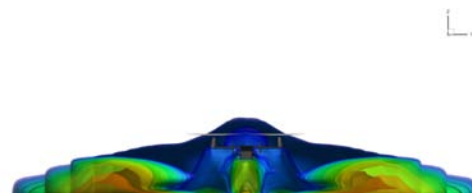
(c) Tilt rotors only (dust cloud)



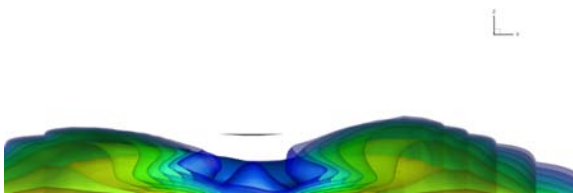
(d) Tilt rotors with fuselage (dust cloud)



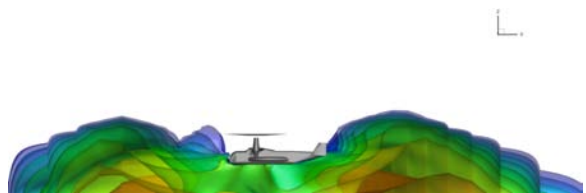
(e) Tilt rotors only (Pilot's front view)



(f) Tilt rotors with fuselage (Pilot's front view)

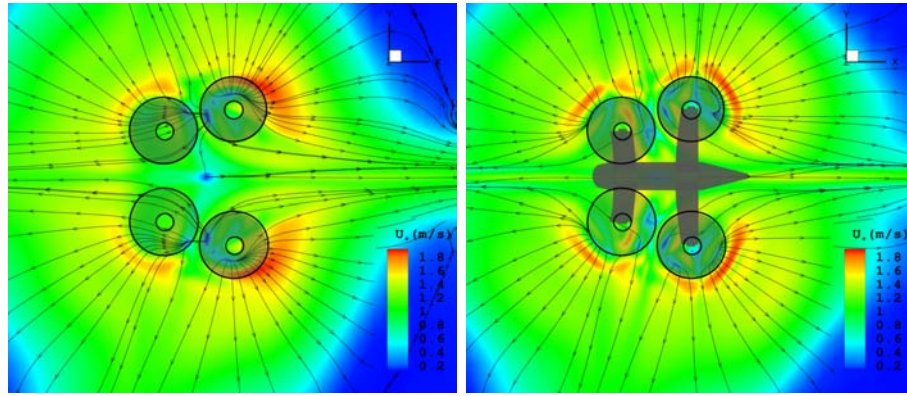


(g) Tilt rotors only (Pilot's side view)

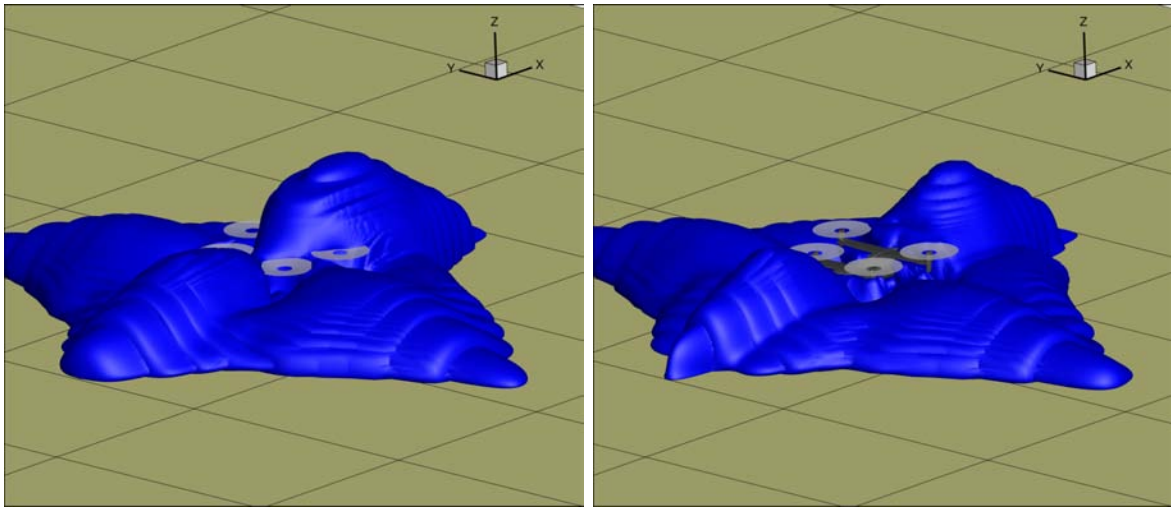


(h) Tilt rotors with fuselage (Pilot's side view)

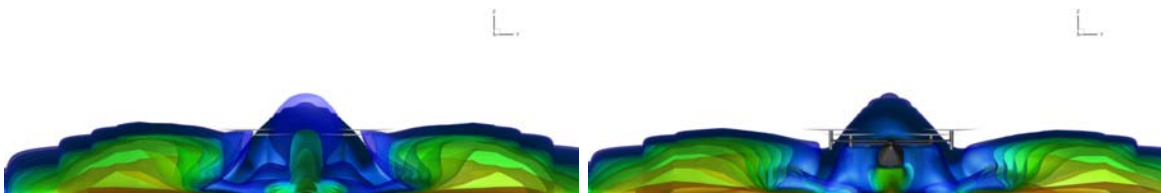
Figure 5.70 Comparison of tilt rotors with and without fuselage at $H = 1.0R_{ref}$



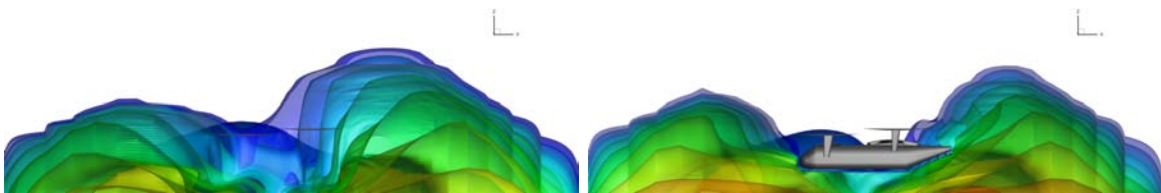
(a) Ground friction velocity for tandem rotors only (b) Ground friction velocity for tandem rotors with fuselage



(c) Quad rotors only (dust cloud) (d) Quad rotors with fuselage (dust cloud)



(e) Quad rotors only (Pilot's front view) (f) Quad rotors with fuselage (Pilot's front view)



(g) Quad rotors only (Pilot's side view) (h) Quad rotors with fuselage (Pilot's side view)

Figure 5.71 Comparison of quad rotors with and without fuselage at $H = 1.0R_{ref}$

CHAPTER 6. CONCLUSION, REMARKS, AND FUTURE WORK

In the current research, a computational test bed has been developed for studying rotorcraft brownout. Various turbulence models have been implemented and tested for impinging type flows, from which the Realizable $k - \epsilon$ model has been selected as more suitable for rotor flows. Momentum source, based time averaged rotor model, has been integrated to solve for rotor flow. The dust transport model based on Eulerian frame of reference has been used for solving the brownout dust transport. The dust entrainment on the ground has been modeled through empirical relations used in geophysical research.

Based on the simulation completed on rotor and fuselage-rotor configurations it has been determined that presence of body has a significant effect in brownout conditions. This effect is particularly pronounced between heights of 1.0 to 3.0 times the rotor radius. The same effect is also observed in multiple rotor configurations.

In the simulations with different fuselage shapes, it has been found that the cross-sectional shape of the fuselage does not have much effect on ground signature if the shadow (the projection on the ground plane) of the body is the same. Although there is not much difference in the wake, separation zones have been observed near the fuselage nose for square and rectangular shaped fuselage because of sharp corners.

In the study of multiple rotor configuration, it has been found the tandem rotor has the most significant ground signature. Although the amount of dust entrainment in tandem is high, from the pilot's front view perspective, has the least visual restriction. Both tilt and quad rotor show lower visual performance because of large dust cloud evolution in front of the fuselage.

Future work Although the ability of the present computational model to predict and calculate the brownout scenario looks promising, further work is needed to model an unsteady rotor, which can capture the effect of an individual rotor.

All the test cases studied in the current research are completed for hovering rotors at different heights; whereas in an actual scenario, the height of the rotorcraft decreases with time. Also, current tactics used by the pilot while landing in an arid desert region is by flying at very low altitudes parallel to the ground and suddenly land like a fixed wing aircraft. By achieving this, the pilot prevents the rotorcraft from engulfing itself in the dust cloud and, thus, extend the visual reference for a longer time. To model this actual scenario, a moving body method must be developed.

BIBLIOGRAPHY

- [1] Rogers, S. J. (1968). Evaluation of The Dust Cloud Generated by Helicopter Rotor Downwash. Technical Report 67-81, U.S. Army Aviation Material Laboratories.
- [2] Chatten, C. (2007). Sandblaster 2 Support of See-Through Technologies for Particulate Brownout. Task 5 Technical Report, U.S. Army Aviation and Missile Command Under Contract No. W31P4Q-07-C-0215 Midwest Research Institute (MRI), Project No. 110565.1.001
- [3] Keller, J. D., Whitehouse, G. R., Wachspress, D. A., Teske, M. E., and Quackenbush, T. R. (2006). A Physics-Based Model of Rotorcraft Brownout for Flight Simulation. *62nd Annual American Helicopter Society Forum*, Phoenix, AZ.
- [4] Ryerson, C. C., Hachnel, R. B., Koenig, G. G., and Moulton, M. A. (2005). Visibility Enhancement in Rotorwash Clouds. *AIAA Aerospace Sciences Meeting and Exhibit*, Reno, Nevada.
- [5] Haehnel, R. B., Moulton, M. A., Wenren, Y., and Steinhoff, J. (2008). A Model to Simulate Rotorcraft-Induced Brownout. *64th Annual Forum of the American Helicopter Society*, Montreal.
- [6] Phillips, C. and Brown, R. E. (2008). Eulerian simulation of the fluid dynamics of helicopter brownout. *American Helicopter Society 64th Annual Forum, Montreal, Canada*, April 29 - May 1, 2008.
- [7] Phillips, C., Kim, H. W. and Brown, R. E. (2009). The Effect of Rotor Design on the Fluid Dynamics of Helicopter Brownout. *35th European Rotorcraft Forum*, Germany.

- [8] Wachspress, D. A., Whitehouse, G. R., Keller, J. D., Yu, K., Gilmore, P., Dorsett, M., and McClure, K. (2009). A high fidelity brownout model for real time flight simulation and trainer. *American Helicopter Society 65th Annual Forum*, Grapevine.
- [9] Keller, J. D., Whitehouse, G. R., Wachspress, D. A., Milton, E. T., Quackenbush, T. R. (2006). A Physics-Based Model of Rotorcraft Brownout for Flight Simulation Applications. *American Helicopter Society 62nd Annual Forum*, Phoenix, AZ.
- [10] Haehnel, R. and Dade, W. B.. (2008). Physics of Particle Entrainment Under the Influence of an Impinging Jet. *Proceedings Army Science Conference*, Orlando, FL.
- [11] Patankar, S. V. (1980). *Numerical heat transfer and fluid flow*. Washington, DC, Hemisphere Publishing Corp..
- [12] Wilcox, D.C., (1998) *Turbulence Modeling for CFD*. 2nd Ed., DCW Industries, Inc..
- [13] Launder, B. E., Reece, G. J. and Rodi, W. (1975). Progress in the Development of a Reynolds-Stress Turbulent Closure. *Journal of Fluid Mechanics*, 68(3), 537–566.
- [14] Craft, T. J., Launder, B. E., and Suga, K. (1997). Prediction of turbulent transitional phenomena with a nonlinear eddy-viscosity model. *International Journal of Heat and Fluid Flow*, 18(1), 15–28.
- [15] Rajagopalan, R. G. and Fanucci, J. B. (1985). Finite difference model for vertical axis wind turbines. *Journal of Propulsion and Power*, 1 432–436.
- [16] Rajagopalan, R. G. and Lim, C. K. (1991). Laminar Flow Analysis of a Rotor in Hover. *Journal of American Helicopter Society*, 36(1) 12–23.
- [17] Rajagopalan, R. G. and Mathur, S, R. (1993). Three Dimensional Analysis of a Rotor in Forward Flight. *Journal of American Helicopter Society*, 38 14–25.

- [18] Baldwin, B. S. and Lomax, H. (1978). Thin Layer Approximation and Algebraic Model for Separated Turbulent Flows. *American Institute of Aeronautics and Astronautics, Aerospace Sciences Meeting*, 78–257.
- [19] Spalart, P. R. and Allmaras, S. R. (1992). A One-Equation Turbulence Model for Aerodynamic Flows. *American Institute of Aeronautics and Astronautics*, 92–0439.
- [20] Launder, B. E. and Spalding, D. B. (1974). The numerical computation of turbulent flows. *Computer Methods in Applied Mechanics and Engineering*, 3(2), 269–289.
- [21] Shih, T. H., Liou, W. W., Shabbir, A., Yang, Z. and Zhu, J. (1995). A new eddy-viscosity model for high Reynolds number turbulent flows—Model development and validation. *Computers Fluids*, 24(3), 227–238
- [22] Kato, M. and Launder, B. E. (1993). The Modeling of Turbulent Flow Around Stationary and Vibrating Square Cylinders. *Proc. 9th Symposium on Turbulent Shear Flows, Kyoto*, 10.4.1–10.4.6.
- [23] Fluent 6.3 (2006). Fluent User's Guide. ANSYS, Inc.
- [24] Shao, Y. (2000). *Physics and modelling of wind erosion*. Boston : Kluwer Academic, Dordrecht.
- [25] Crowe, C., Sommerfeld, M. and Tsuji, Y. (1998). *Multiphase flows with droplets and particles*. CRC Press (Boca Raton, Fla) .
- [26] Iversen, J. D., Greeley, R. and Pollack, J. B., (1976). Wind blown dust on Earth, Mars and Venus. *Journal of Atmospheric Science*, 33, 2425-2429.
- [27] Bagnold, R. A. (1941). *The physics of blown sand and desert dunes*. *Journal of Atmospheric Science*, London: Methuen, 265 pp.
- [28] Greeley, R. and Iversen, J. D. (1985). Wind as a Geological Process. *Cambridge University Press*, 99-100.

- [29] Lu, H. and Shao, Y. (2001). Towards quantitative prediction of dust storms: An integrated wind erosion modelling system and its application. *Environmental Modelling and Software*, 16(3), 233–249.
- [30] Owen, P. R. (1964). Saltation of uniform grains in air. *Journal of Fluid Mechanics*, 20(2), 225-242.
- [31] Nalpanis, P., Hunt, J. C. R. and Barrett, C. F. (1993). Saltating particles over flat beds. *Journal of Fluid Mechanics*, 251, 661–685.
- [32] Gillette, D. A. (1977). Fine particulate emissions due to wind erosion. *Transactions of the American Society of Agricultural Engineers*, 20, 890–897.
- [33] Marticorena, B. and Bergametti, G. (1995). Modeling the atmospheric dust cycle: 1. Design of a soil-derived dust emission scheme. *Journal of Geophysical Research*, 100(D8), 415–430.
- [34] Ishii, M. (1975). *Thermo-fluid dynamic theory of two-phase flow*. Paris: Evrolles
- [35] Durst, F., Miloevic, D. and Schnung, B. (1984). Eulerian and Lagrangian predictions of particulate two-phase flows: a numerical study. *Journal of Instructional Computing Research*, 8(2), 101–115.
- [36] Shirolkara, J. S., Coimbrab, C. F. M. and Queiroz McQuay, M. (1984). Fundamental aspects of modeling turbulent particle dispersion in dilute flows. *Progress in Energy and Combustion Science*, 22(4), 363–399.
- [37] Crowe, C. T., Troutt, T. R. and Chung, J. N. (1984). Numerical models for two-phase turbulent flows. *Annual Review of Fluid Mechanics*, 28, 11–43.
- [38] Manninen, M., Taivassalo, V., and Kallio, S. (1996). On the mixture model for multiphase flow. VTT Publications 288, Technical Research Centre of Finland, 1996.

- [39] Wirogo, S. (1997). Flux corrected method: An accurate approach to fluid flow modeling. Ph.D Thesis, Iowa State University. AAT 9737770
- [40] Schlichting, H., Gersten, K. and Gersten, K. (1979). *Boundary-Layer Theory*. McGraw Hill, New York. ISBN: 978-3-540-66270-9.
- [41] Cooper, D., Launder, D. C. and Liao, G. X. (1993)]. Impinging jet studies for turbulence model assessment. Part I: Flow-field experiments. *International Journal of Heat Mass Transfer*, 36, 2675–2684.
- [42] Craft, T. J., Graham, L. J. W., and Launder, B. E., (1993). Impinging jet studies for turbulence model assessment. Part 2: An examination of the performance of four turbulence models. *International Journal of Heat and Mass Transfer*, 36, 2685–2697.
- [43] Rabbott, J. P. (1956). Static-Thrust Measurements of the Aerodynamic Loading on a Helicopter Rotor Blade. Technical Report, National Aeronautics and Space Administration, Washington DC.
- [44] Nathan, N. D. and Green, R. B. (2008). Measurements of a rotor flow in ground effect and visualization of the brown-out phenomenon. *Helicopter Society Annual Forum*, Montreal, Canada.
- [45] Preston, J. R. (1994). VTOL Downwash/Outwash Operational Effects Model. *Annual Forum Proceedings, American Helicopter Society*, 50(V2),1101.
- [46] Phillips, C. and Brown, R. E. (2008). The effect of helicopter configuration on the fluid dynamics of brownout. *34th European Rotorcraft Forum*, 16th - 19th Sept 2008, Liverpool, England.
- [47] Tennekes, H. and Lumley, J. L. (1972). *A First Course in Turbulence*. MIT Press, Cambridge, MA.

- [48] Jones, W. P. and Launder, B. E (1972). The Prediction of Laminarization with a Two-Equation Model of Turbulence. *International Journal of Heat and Mass Transfer*, 15, 301–314

APPENDIX A. WALL FUNCTIONS

At high Reynolds number, a very steep gradient of velocity exists for the flow near the wall. Based on non-dimensional distance $y^+ = \frac{u_* y}{\nu}$, the region near the wall can be divided into three different layers [47].

1. viscous sub-layer ($0 < y^+ < 5$)
2. buffer layer ($5 < y^+ < 30$)
3. inertial sub-layer ($30 < y^+ < 200$)

To accurately capture the velocity gradient, a very refined mesh is required near the wall, which can capture the viscous sub-layer. This increases computational requirements tremendously for the high Reynolds number flow, where the viscous sub-layer is very thin. Also the $k - \epsilon$ Model (and other high Reynolds number turbulence models) do not consider the effect of near-wall in their modelling. So, these models cannot be integrated into the wall since they give inaccurate predictions. To overcome this, the first node of the mesh is kept in an inertial sub-layer and the other required variables are calculated using law of the wall or wall function.

A.1 Standard Wall Function

In the attached turbulent boundary layer, velocity profile in inertial sub-layer is given by logarithmic profile [12] known as wall of law.

$$\frac{U}{u_*} = \frac{1}{\kappa} \ln(Ey^+) \quad (\text{A.1})$$

where κ is van Karman constant equal to 0.41 and E is empirical constant equal to 9.793. If U_p is the velocity at the first node point in the inertial sub-layer, then wall friction can be calculated as

$$\tau_w = \frac{\rho u_* U_p}{\ln(Ey^+)} \quad (\text{A.2})$$

The wall friction calculated through the wall function approach is implemented in the existing discretized equation by modifying the wall viscosity, μ_e , which can be calculated as

$$\tau_w = \mu \frac{\partial U}{\partial y} = \mu_e \frac{U_p}{y_p} \Rightarrow \mu_e \frac{U_p}{y_p} = \frac{\rho u_* U_p}{\ln(Ey^+)} \Rightarrow \mu_e = \frac{\rho u_* y_p \kappa}{\ln(Ey_p^+)} \quad (\text{A.3})$$

A.2 Launder Spalding Wall Function

One of problems with the standard wall function is the u_* goes to zero at separating and re-attachment point, thus causing singularity. Launder and Spalding [20] proposed to use identity $u_* = C_\mu^{1/4} \sqrt{k}$ in calculating effective wall viscosity.

$$\mu_e = \frac{\rho C_\mu^{1/4} \sqrt{k_p} y_p \kappa}{\ln(Ey_p^*)} \quad (\text{A.4})$$

where

$$y_p^* = \frac{y_p C_\mu^{1/4} \sqrt{k_p}}{\nu} \quad (\text{A.5})$$

In the current research, the wall function is applied for the wall adjacent node with $y_p^* > 11.225$ as used in commercial software, Fluent [23].

A.3 Turbulence

Based on the local equilibrium hypothesis in the wall adjacent cell, production of turbulent kinetic energy and dissipation are assumed equal. Accordingly, turbulent production in the wall adjacent cell is calculated as [23]

$$P_k \approx \tau_w \frac{\partial U}{\partial y} = \tau_w \frac{\tau_w}{\kappa \rho C_\mu^{1/4} \sqrt{k_p} y_p} \quad (\text{A.6})$$

and the turbulent dissipation in wall adjacent node is calculated as

$$\epsilon_p = \frac{C_\mu^{3/4} k_p^{3/2}}{\kappa y_p} \quad (\text{A.7})$$

A.4 Wall Function for Rough Wall

Effective viscosity for the rough wall is given by

$$\mu_e = \frac{\rho C_\mu^{1/4} \sqrt{k_p} y_p \kappa}{\ln(E y_p^*) - \Delta B} \quad (\text{A.8})$$

where ΔB is the roughness function which depends upon non-dimensional roughness height K_s^+ . K_s^+ is given by

$$K_s^+ = \frac{\rho K_s u_*}{\mu} \quad (\text{A.9})$$

where K_s is the physical roughness height.

The wall is considered smooth when $K_s^+ < 2.25$. In this case, $\Delta B = 0$. For a fully rough regime, when $K_s^+ > 90$,

$$\Delta B = \frac{1}{\kappa} \ln(1 + C_{ks} K_s^+) \quad (\text{A.10})$$

where C_{ks} is roughness constant which varies from 0.5 to 1.0.